

POLITECNICO DI TORINO

in collaboration with

ÉCOLE POLYTECHNIQUE FÉDÉRALE DE LAUSANNE

Master's Degree in Civil Engineering



EPFL

Master's Degree Thesis

**Fracture mechanism study applied to limit
equilibrium analysis of an unstable rock mass**

Supervisors:

Prof. Claudio Scavia, Politecnico di Torino

Prof. Marie Violay, EPFL

Dr. Federica Sandrone, EPFL

Dr. Lucas Pimienta, EPFL

Dr. François Passèlegue, EPFL

Candidate

Salvatore D'Urso

July 2019

“Hey! Non permettere mai a nessuno di dirti che non sai fare qualcosa. Neanche a me. Ok? Se hai un sogno tu lo devi proteggere. Quando le persone non sanno fare qualcosa lo dicono a te che non la sai fare. Se vuoi qualcosa, vai e inseguila. Punto.”

*Chris Gardner (Will Smith)
dal film “La ricerca della felicità”*

Abstract

In geotechnical field, the Limit Equilibrium Method (LEM) is one of the most used analysis to solve the stability problem of an unstable rock cliff. A limit of the LEM is the impossibility of considering the evolution over the time of the rock's mechanical parameters and also the effect of the crack tip stress concentrations, which may trigger a crack propagation. The aim of this thesis is to overcome these limitations of the LEM model, proposing the application of a fracture mechanism approach on the real unstable cliff of "Madonna del Sasso". In this study, the effects of degradation of rock joint are evaluated through a time-dependent reduction of rock bridge along the discontinuity. After a preliminary characterization of the granite samples, many laboratory experiments were carried out on the CCNBD specimens to investigate the mode I and mode II fracture toughness of the rock under different types of load. The intact granite specimens have been thermally treated in order to have a better representation of the possible in situ degradation of the rock and, in the end, the subcritical crack growth parameters have been computed to apply the fracture mechanism approach to the LEM analysis. The final result shows the decrease of the safety factor F_s over the time which becomes critical after 193 years. Nevertheless, some critical issues have arisen during the development of this fracture mechanism approach. Therefore, it appears that this approach still needs to be improved before being considered reliable for big scale application on rock slope stability

Keywords: Limit Equilibrium Method, stability, rock cliff, crack propagation, unstable rock mass, fracture mechanics, , LEFM, reduction of rock bridge, granite, laboratory experiments, CCNBD specimen, mode I fracture toughness, mode II fracture toughness, thermal treatment, acoustic emission, subcritical crack growth, reduction of safety factory over the time.

Sommario

Il Metodo dell'Equilibrio Limite (LEM) rappresenta uno degli strumenti più utilizzati in ambito geotecnico per risolvere i problemi di stabilità legati ad un ammasso roccioso. Un limite di tale metodo consiste, tuttavia, nell'impossibilità di valutare l'evoluzione nel tempo dei parametri meccanici della roccia e, inoltre, di non considerare gli effetti di tensioni concentrate che possono innescare la propagazione di una frattura. L'obiettivo della seguente tesi è di cercare di superare queste limitazioni del Metodo dell'Equilibrio Limite applicando un modello che consideri il meccanismo di propagazione della frattura sul versante roccioso della "Madonna del Sasso". In questo modello, gli effetti dovuti al degrado della roccia in corrispondenza delle discontinuità sono valutati attraverso la progressiva riduzione nel tempo dei ponti di roccia. Dopo aver effettuato una caratterizzazione preliminare del granito, sono stati testati in laboratorio numerosi campioni CCNBD al fine di investigare la resistenza alla frattura di modo I e modo II, facendo variare le condizioni di carico. I campioni di granito intatto sono stati termicamente trattati per emulare il possibile degrado della roccia in situ. Infine, sono stati calcolati i parametri di crescita subcritica della frattura per l'implementazione del modello della meccanica della frattura nell'analisi condotta con il Metodo dell'Equilibrio Limite. Il risultato finale del nuovo studio mostra una progressiva riduzione del fattore di sicurezza F_s nel tempo, che risulta critico dopo circa 193 anni. Tuttavia, si sono manifestate alcune criticità nello sviluppo di tale approccio basato sulla meccanica della frattura. Perciò, sono ancora necessari dei miglioramenti per rendere questo modello adatto ad una analisi di stabilità a grande scala.

Résumé

La Méthode de l'Équilibre Limite (LEM) représente un des outils les plus utilisés en géotechnique pour résoudre les problèmes de stabilité liés à une masse rocheuse. Cependant, une limitation de cette méthode réside dans l'impossibilité d'évaluer l'évolution dans le temps des paramètres mécaniques de la roche et, parallèlement, de ne pas prendre en compte les effets de tensions concentrées, qui peuvent déclencher la propagation d'une fracture. L'objectif de la thèse suivante est d'essayer de surmonter ces limitations de la méthode de l'équilibre limite en appliquant un modèle prenant en compte le mécanisme de fracture de la masse rocheuse instable de "Madonna del Sasso". Dans ce modèle, les effets dus à la dégradation de la roche en correspondance avec les discontinuités sont évalués par la réduction progressive des ponts rocheux au fil du temps. Après avoir procédé à une caractérisation préliminaire du granite, plusieurs tests en laboratoire ont été effectués sur des CCNBD échantillons afin d'étudier la résistance à la rupture des modes I et II en faisant varier les conditions de chargement. Les échantillons de granite intact ont été soumis à un traitement thermique afin de simuler la possible dégradation de la roche in situ. Enfin, les paramètres de croissance sous-critiques de la fracture ont été calculés pour la mise en œuvre du modèle de mécanique de la fracture dans l'analyse effectuée avec la méthode de l'équilibre limite. Le résultat final de la nouvelle étude montre une réduction progressive du facteur de sécurité F_s au fil du temps, en devenant critique au bout d'environ 193 ans. Cependant, certains problèmes critiques sont apparus dans le développement de cette approche basée sur la mécanique de la fracture. Par conséquent, des améliorations sont encore nécessaires pour rendre ce modèle adapté à l'analyse de stabilité à grande échelle.

Contents

Abstract	III
Sommario 	IV
Résume 	V
Contents	VI
List of Figures	IX
List of Tables	XVI
List of Equations.....	XIX
Introduction.....	1
Chapter 1: Stability analysis of the cliff of Madonna del Sasso.....	4
1.1 Geological framework	5
1.2 Introduction to LEM theory	6
1.3 Static analysis.....	8
1.3.1 Planar sliding	9
1.3.2 Wedge sliding	10
1.3.3 Toppling	11
1.3.4 Stereographic investigation	12
1.4 Geometrical and geomechanical data assumptions	13
1.5 Analysis of forces	14
1.5.1 Gravitation case.....	14
1.5.2 Joint's saturation case	15
1.5.3 Seismic action case	16
1.5.4 Extreme case	18

1.6	LEM analysis results	18
1.6.1	Sector A	18
1.6.2	Sector B.....	20
1.6.3	Toppling analysis	21
1.7	Concluding remarks.....	22
Chapter 2: Fracture Mechanics.....		25
2.1	Concepts of linear elastic fracture mechanics (LEFM).....	25
2.2	Fracture mechanism approach	29
2.3	Fracture toughness testing method	30
2.3.1	Semi-Circular Bend (SCB) specimen.....	31
2.3.2	Cracked Chevron Notched Brazilian Disc (CCNBD) specimen.....	32
2.3.3	Discussion about the most suitable test.....	33
Chapter 3: Preliminary characterization of granite of Alzo.....		35
3.1	Porosity analysis	36
3.1.1	Pycnometer test	36
3.1.2	Indirect method.....	37
3.1.3	Conclusions.....	39
3.2	Electrical conductivity analysis	40
3.3	Ultrasonic propagation test.....	49
3.3.1	Seismic data comparison with literature and considerations	53
3.4	Triaxial test	56
3.5	Concluding remarks.....	58
Chapter 4: Fracture toughness investigation		60
4.1	Sample preparation.....	61
4.1.1	Cutting phase.....	61
4.1.2	Thermal treatment	61
4.1.3	Sensors positioning.....	63
4.1.4	Acoustic emission's sensors.....	63
4.1.5	CCNBD geometry	64

4.2	Mode I fracture toughness investigation	67
4.2.1	Mode I fracture toughness with increasing load until failure.....	67
4.2.2	Mode I fracture toughness with constant load (creep).....	79
4.2.3	Mode I fracture toughness with cyclic load (fatigue).....	84
4.3	Mode II fracture toughness investigation	89
Chapter 5: Subcritical crack growth		91
5.1	Investigation for 200° C thermally treated granite	92
5.2	Investigation for different thermally treated granites.....	94
5.2.1	100° C thermally treated sample (G32).....	100
5.2.2	300° C thermally treated sample (G31).....	102
5.2.2	400° C thermally treated sample (G30).....	104
5.3	Concluding remarks.....	106
Chapter 6: Fracture mechanism application to the LEM analysis.....		108
6.1	Problem's assumptions	108
6.2	Analysis result	109
6.3	Limits of the analysis	110
Chapter 7: Conclusions and perspectives.....		112
7.1	Perspectives.....	112
References.....		116
Acknowledgements.....		120

List of Figures

Chapter 1: Stability analysis of the cliff of Madonna del Sasso

Figure 1.1: Geographical localitation (a) and aerial view (b) of the cliff of Madonna del Sasso cliff	4
Figure 1.2: Aerial view (a) and schematic representation (b) of the major fracture traces a discontinuity planes [3].....	5
Figure 1.3: A typical cross-section of a slope used in two-dimensional analyses	8
Figure 1.4: Schematic representation (a) and a real example (b) of a planar sliding [6].....	9
Figure 1.5: Schematic representation (a) and a real example (b) of a wedge sliding [6].....	10
Figure 1.6: Schematic representation (a) and a real example (b) of a toppling failure [6]	11
Figure 1.7: Stereographic view of the four joint's families detected by Lancellotta in 1991	12
Figure 1.8: Qualitative analysis of the height of the unstable rock mass with Google Earth Pro	13
Figure 1.9: Representation of cohesion and weight force vectors on the unstable slope model.....	14
Figure 1.10: Representation of water pressure vectors on the unstable slope model	16
Figure 1.11: Representation of seismic force vectors on the unstable slope model	17

Figure 1.12: LEM analysis of Sector A under four different loading cases ...	19
Figure 1.13: LEM analysis of Sector B under four different loading cases	20
Figure 1.14: Qualitative analysis of the width of the unstable slope with Google Earth Pro	21
Figure 1.15: Toppling analysis of the unstable cliff.....	22
Figure 1.16: Factor of safety comparison between sector A and sector B in the gravitation case.....	23

Chapter 2: Fracture Mechanics

Figure 2.1: Three primary failure modes	26
Figure 2.2: Cracks in mode I and mode II conditions in rock structures: (a) tunnel; (b) slope [9]	26
Figure 2.3: Reference axes and variables [9].....	27
Figure 2.4: Fracture mechanics models, a) single rock bridge under far field normal and shear stresses, b) multiple rock bridges under far field normal and shear stresses [10]	29
Figure 2.5: SCB specimen geometry and schematic loading arrangement [12]	32
Figure 2.6: CSTBD and CCNBD specimen geometries [14].....	33

Chapter 3: Preliminary characterization of granite of Alzo

Figure 3.1: Porosity analysis rock A	39
Figure 3.2: Porosity analysis rock B.....	40
Figure 3.3: Example of fluid's and rock's conductivity relationship (Courtesy of Prof. Violay).....	47
Figure 3.4: Formation factor F and pycnometer porosity ϕ	48
Figure 3.5: Pulse transmission sketch	50
Figure 3.6: P wave of the dry GB1 sample (test 1).....	50

Figure 3.7: P wave of the dry GB1 sample (test 2).....	50
Figure 3.8: V_p -porosity plane comparison between saturated samples (1 week), saturated samples (2 weeks) and dry samples.....	52
Figure 3.9: V_s -porosity plane comparison between saturated samples (1 week), saturated samples (2 weeks) and dry samples.....	53
Figure 3.10: V_p - V_s plane comparison between saturated samples (1 week), saturated samples (2 weeks) and dry samples	53
Figure 3.11: Triaxial test result	57
Figure 3.12: $t - s$ deviatoric plane	58
Figure 3.13: Photo of the specimen after the triaxial test	59

Chapter 4: Fracture toughness investigation

Figure 4.1: Special jig recommended by the ISRM with the circular diamond saw	61
Figure 4.2: CCNBD sample into the oven ready for the thermal treatment..	62
Figure 4.3: CCNBD specimen with all the sensors placed on it (AE sensors, strain gauges and extensometer) and ready for the test	63
Figure 4.4: CCNBD specimen's geometry [15]	64
Figure 4.5: ISRM suggested valid geometry for CCNBD specimen's valid geometry.....	66
Figure 4.6: Stress intensity factor in function of the axial displacement for each samples during the mode I fracture toughness tests (increasing load) .	68
Figure 4.7: Stress intensity factor in function of the CMOD for each samples during the mode I fracture toughness tests (increasing load).....	68
Figure 4.8: K_I/K_{IC} in function of the axial displacement (increasing load tests).....	69
Figure 4.9: K_I/K_{IC} in function of the CMOD (increasing load tests).....	69
Figure 4.10: $K_I/K_{IC,25}$ in function of $V_p/V_{p,25}$	70

Figure 4.11: $K_I/K_{IC,25}$ in function of the temperature of the thermal treatment 70

Figure 4.12: Stress intensity factor evolution coupled with AE of test G8 (no treated)..... 72

Figure 4.13: CMOD evolution coupled with AE of test G8 (no treated)..... 72

Figure 4.14: Acoustic emission cumulative evolution of test G8 (no treated) ... 72

Figure 4.15: Stress intensity factor evolution coupled with AE of test G7 (100° C) 73

Figure 4.16: CMOD evolution coupled with AE of test G7 (100° C) 73

Figure 4.17: Acoustic emission cumulative evolution of test G7 (100° C) 73

Figure 4.18: Stress intensity factor evolution coupled with AE of test G6 (200° C) 74

Figure 4.19: CMOD evolution coupled with AE of test G6 (200° C) 74

Figure 4.20: Acoustic emission cumulative evolution of test G6 (200° C) 74

Figure 4.21: Stress intensity factor evolution coupled with AE of test G9 (300° C) 75

Figure 4.22: CMOD evolution coupled with AE of test G9 (300° C) 75

Figure 4.23: Acoustic emission cumulative evolution of test G9 (300° C) 75

Figure 4.24: Stress intensity factor evolution coupled with AE of test G4 (400° C) 76

Figure 4.25: CMOD evolution coupled with AE of test G4 (400° C) 76

Figure 4.26: Acoustic emission cumulative evolution of test G4 (400° C) 76

Figure 4.27: Picture of G8 sample (no thermally treated) before and after the test 77

Figure 4.28: Picture of G7 sample (100° C) before and after the test 77

Figure 4.29: Picture of G6 sample (200° C) before and after the test 77

Figure 4.30: Picture of G9 sample (300° C) before and after the test 78

Figure 4.31: Picture of G4 sample (400° C) before and after the test 78

Figure 4.32: G8 sample during the test and just after the crack propagation	78
Figure 4.33: Stress intensity factor evolution coupled with AE of test G10 (creep)	79
Figure 4.34: Comparison of CMOD between the mode I fracture behaviour in the creep tests	80
Figure 4.35: CMOD evolution coupled with AE of test G10 (creep)	81
Figure 4.36: Acoustic emission cumulative evolution of test G10 (creep).....	81
Figure 4.37: CMOD evolution coupled with AE of test G16 (creep)	82
Figure 4.38: Acoustic emission cumulative evolution of test G16 (creep).....	82
Figure 4.39: CMOD evolution coupled with AE of test G12 (creep)	83
Figure 4.40: Acoustic emission cumulative evolution of test G12 (creep).....	83
Figure 4.41: K_I/K_{IC} evolution of test G36 (cyclic)	84
Figure 4.42: CMOD evolution of test G36 (cyclic).....	85
Figure 4.43: K_I/K_{IC} in function of the CMOD of test G36 (cyclic).....	85
Figure 4.44: CMOD evolution of test G17 (cyclic).....	86
Figure 4.45: K_I/K_{IC} in function of the CMOD of test G17 (cyclic)	86
Figure 4.46: CMOD evolution of test G24 (cyclic).....	87
Figure 4.47: Detail of the first crack propagation in the CMOD evolution of test G24 (cyclic).....	87
Figure 4.48: K_I/K_{IC} in function of the CMOD of test G24 (cyclic)	87
Figure 4.49: G1 sample during the mode II fracture toughness test.....	90
Figure 4.50: Picture of the G1 sample after the failure with a tilted crack propagation.....	90

Chapter 5: Subcritical crack growth

Figure 5.1: Subcritical fracture growth patterns [29]	93
Figure 5.2: Subcritical crack growth parameters determination for creep tests	93
Figure 5.3: K_I/K_{IC} evolution of test G3	96
Figure 5.4: CMOD evolution of test G3	96
Figure 5.5: K_I/K_{IC} evolution of test G23	97
Figure 5.6: CMOD evolution of test G23	97
Figure 5.7: Subcritical crack growth parameters determination for sample G3	98
Figure 5.8: Subcritical crack growth parameters determination for sample G23	99
Figure 5.9: Comparison between subcritical crack growth parameters.....	100
Figure 5.10: K_I/K_{IC} evolution of test G32	101
Figure 5.11: CMOD evolution of test G32	101
Figure 5.12: Subcritical crack growth parameters determination for sample G32	102
Figure 5.13: K_I/K_{IC} evolution of test G31	103
Figure 5.14: CMOD evolution of test G31	103
Figure 5.15: Subcritical crack growth parameters determination for sample G31	104
Figure 5.16: K_I/K_{IC} evolution of test G30	105
Figure 5.17: CMOD evolution of test G30	105
Figure 5.18: Subcritical crack growth parameters determination for sample G30	106
Figure 5.19: Summary of all the thermally treated sample about the subcritical crack growth	107

Chapter 6: Fracture mechanism application to the LEM analysis

Figure 6.1: Fracture mechanics models, a) single rock bridge under far field normal and shear stresses, b) multiple rock bridges under far field normal and shear stresses [10] 109

Figure 6.2: Reduction of the Safety factor over the years with $n=13$ 110

Figure 6.3: Reduction of the Safety factor over the years with $n=15$ 111

List of Tables

Chapter 1: Stability analysis of the cliff of Madonna del Sasso

Table 1.1: Joint sets parameters from the geomechanical characterization carried out by Lancellotta et al. [1991]	6
Table 1.2: Input parameters for sector A analysis	19
Table 1.3: Input parameters for sector B analysis.....	20

Chapter 3: Preliminary characterization of granite of Alzo

Table 3.1: Final result of the Pycnometer test	37
Table 3.2: Final results of the indirect method to find the porosity.....	38
Table 3.3: Electrical resistivity computation	43
Table 3.4: First electrical test on samples saturated with tap water	43
Table 3.5: Second electrical test on samples saturated in a 0.15 % salty solution.....	44
Table 3.6: Third electrical test on samples saturated in a 1.5 % salty solution.....	45
Table 3.7: Fourth electrical test on samples saturated in a 3 % salty solution...	46
Table 3.8: Formation factor, tortuosity and cementation index of the samples	48
Table 3.9: Final results of the seismic test on the rock A.....	51
Table 3.10: Final results of the seismic test on the rock B.....	51
Table 3.11: Results of the microcracks aspect ratio and density investigation ..	56

Table 3.12: Residual phase stress condition	57
Table 3.13: Residual friction angle φ_r and the cohesion c of the rock.....	58
 Chapter 4: Fracture toughness investigation	
Table 4.1: Summary of geometrical data	66
Table 4.2: Summary of the mode I fracture toughness investigation.....	71
Table 4.3: Summary of the mode I fracture toughness investigation under creep behaviour	80
Table 4.4: Summary of the mode I fracture toughness investigation under cyclic load	85
Table 4.5: Comparison between creep and cyclic tests based on KI, max	88
Table 4.6: Comparison between creep and cyclic tests based on KI, avg	88
Table 4.7: Values of ϕ and N_{II} for different crack length ratios a/R in the CCNBD specimen	89
Table 4.8: Geometrical and mechanical parameters of mode II fracture toughness test	90
 Chapter 5: Subcritical crack growth	
Table 5.1: Subcritical crack growth velocity computed from the creep tests	91
Table 5.2: Loading path for the test on G3.....	94
Table 5.3: Loading path for the test on G23.....	95
Table 5.4: Subcritical crack growth velocity computation for G3 sample	98
Table 5.5: Subcritical crack growth velocity computation for G23 sample ...	98
Table 5.6: Comparison of subcritical crack growth parameters for 200° C treated samples.....	99
Table 5.7: Loading path for the test on G32.....	100
Table 5.8: Subcritical crack growth velocity computation for G32 sample .	101

Table 5.9: Loading path for the test on G31..... 102

Table 5.10: Subcritical crack growth velocity computation for G31 sample 103

Table 5.11: Loading path for the test on G30..... 104

Table 5.12: Subcritical crack growth velocity computation for G30 sample 105

Table 5.13: Comparison between subcritical crack growth parameters 106

List of Equations

Chapter 1: Stability analysis of the cliff of Madonna del Sasso

Equation 1.1: Shear strength with Mohr-Coulomb criterion.....	7
Equation 1.2: Theoretical formula of the factor of safety in the limit equilibrium method.....	7
Equation 1.3: Generic formula of the factor of safety for planar sliding.....	14
Equation 1.4: Safety factor formulation for planar sliding in gravitation case	15
Equation 1.5: Formula for the water force computation of fully saturated joint.....	15
Equation 1.6: Safety factor formulation for planar sliding in joint's saturation case	16
Equation 1.7: Vertical and horizontal seismic forces	16
Equation 1.8: Horizontal seismic coefficient formula.....	17
Equation 1.9: Maximum seismic acceleration on the study field.....	17
Equation 1.10: Safety factor formulation for planar sliding in presence of a seismic action.....	18
Equation 1.11: Safety factor formulation for planar sliding in presence of all acting forces	18
Equation 1.12: Generic safety factor formulation for toppling mechanism ...	21
Equation 1.13: Safety factor formulation for toppling in presence of only weight force	21

Chapter 2: Fracture Mechanics

Equation 2.1: Planar stress state in a polar system of reference.....27

Equation 2.2: Stress state in plane conditions for $\theta = 0$27

Equation 2.3: Vertical stress around the crack tip28

Equation 2.4: Stress intensity factor formula28

Equation 2.5: Power-law of the variation of rock bridge size over time.....30

Equation 2.6: Time-dependent reduction of the rock bridge.....30

Chapter 3: Preliminary characterization of granite of Alzo

Equation 3.1: Bulk volume for cylindrical sample37

Equation 3.2: Matrix volume formula.....37

Equation 3.3: Porosity formula37

Equation 3.4: Pores volume formula used in the indirect method38

Equation 3.5: Electrical resistivity formula41

Equation 3.6: Electrical conductivity of rock formation.....41

Equation 3.7: Formation factor law for high porosity rocks.....41

Equation 3.8: Formation factor law for low porosity rocks42

Equation 3.9: Electrical conductivity proportional formula42

Equation 3.10: Reduced Archie’s law.....46

Equation 3.11: Velocity formula.....49

Equation 3.12: P- and S-wave velocities in function of the rock’s mechanical properties54

Equation 3.13: Relationship between the shear and bulk moduli with the microcrack density55

Equation 3.14: Relationship between bulk modulus and the microcrack aspect ratio55

Equation 3.15: Fluid compressibility55

Equation 3.16: Deviatoric and average stress formula57

Equation 3.17: Residual friction angle ϕ_r and the cohesion c formula58

Chapter 4: Fracture toughness investigation

Equation 4.1: Dimensionless geometrical parameters.....64

Equation 4.2: Geometrical validity range for CCNBD sample.....65

Equation 4.3: Mode I fracture toughness.....67

Equation 4.4: Mode I critical non-dimensional stress intensity factor67

Equation 4.5: Mode II fracture toughness89

Chapter 5: Subcritical crack growth

Equation 5.1: Subcritical crack growth velocity power-law92

Equation 5.2: Reduced subcritical crack growth velocity law92

Equation 5.3: Logarithmic reduced subcritical crack growth velocity law92

Chapter 6: Fracture mechanism application to the LEM analysis

Equation 6.1: Time-dependent reduction of the rock bridge.....108

Introduction

The study of stability and prediction of the behaviour of an unstable rock mass represents one of the most difficult problems in the engineering field. Its complexity is linked to the difficult identification of the mechanical parameters to be used in the numerical analysis, and to the high variability of external factors such as air temperature variation, presence and evaluation of water pressure, seismic events, rock degradation, etc. In geotechnical field, it is usual to use the Limit Equilibrium Method (LEM) to solve the stability problem of the unstable rock cliff. The behaviour of rock slopes is strongly affected by their geometric configuration and by the discontinuities in the rock mass. For this reason, in the LEM analysis the rock mass is considered as rigid body and the presence of discontinuities is taken into account by choosing strength parameters lower than the those characteristic of the rock material. One of the limits of the LEM analysis is the impossibility of considering an evolution over time of the rock's mechanical parameters. The area where the rock formation mostly degrade is concentrated at the joints, in fact, if discontinuities are filled with a material that is weaker than the surrounding intact rock, this material might exhibit ductile creep behaviour under shear loading. Furthermore, the asperities along rough joints will likely be concentrators of shear stress, promoting the crack propagation. Therefore, the probability of failure over the life of an unstable rock mass can be much higher compared with the time-independent analysis. The aim of this thesis is to overcome these limits of the LEM model, proposing the application of a fracture mechanism approach. According to the Linear Elastic Fracture Mechanism (LEFM), the crack will propagate when its stress intensity factor reaches a critical value K_{IC} (fracture toughness), but natural fractures can grow at lower stress intensities. In these cases, we talk about subcritical crack

propagation. In 2003, J. Kemeny developed a fracture mechanics model, based on the subcritical crack growth, in order to illustrate the importance of time-dependence for brittle fractured rock. According to his study, the effects of degradation of rock joint can be evaluated through a time-dependent reduction of rock bridge along the discontinuity. Therefore, after a preliminary characterization of the granite samples, many laboratory experiments were carried out for the investigation of mode I and mode II fracture toughness of the rock under different methods of loads. The intact granite specimens have been also thermally treated in order to have a better representation of the possible in situ degradation of the rock. Finally, the subcritical crack growth parameters have been computed in order to apply the fracture mechanism approach to the LEM analysis.

The structure of this master's thesis is as follows:

- Chapter 1, entitled "Stability analysis of the cliff of Madonna del Sasso", presents the description of the unstable rock mass and an attempt of resolution of the stability analysis, performed with the Limit Equilibrium Method ;
- Chapter 2, entitled "Fracture mechanics", summaries the concepts of the Linear Elastic Fracture Mechanics (LEFM), and promotes a new fracture mechanism approach based on the study J. Kemeny about the the effects of degradation of rock joint, which are evaluable through a time-dependent reduction of rock bridge along the discontinuity. Finally, several specimens are suggested for the mode I and mode II fracture toughness investigation, with a focus on the CCNBD specimen;
- Chapter 3, entitled "Preliminary characterization of granite of Alzo", encloses several tests carried out on the granite samples in order to ensure that two granite's rock blocks have the same physical and mechanical properties. Porosity, electrical conductivity and ultrasonic propagation have been investigated;

- Chapter 4, entitled “Fracture toughness investigation”, describes the three types of mode I fracture toughness experiments (Increasing load, constant load and cyclic load) and the mode II fracture toughness test. The sample preparation and the experimental set-up are particularly deepened, and there is a special focus on the comparison between the creep and fatigue behaviour of the rock ;
- Chapter 5, entitled “Subcritical crack growth”, presents the investigation of the subcritical crack growth parameters for the 200° C thermally treated sample. Furthermore, it is described a new kind of test carried out in order to determine the same parameters for different thermally treated samples;
- Chapter 6, entitled “Fracture mechanism application to the LEM analysis”, shows the stability analysis of the Madonna del Sasso rock cliff, based on the fracture mechanism approach. There is a particular focus on the problem’s assumptions and on the fracture mechanism’s limits;
- Chapter 7, entitled “Conclusions and perspectives”, summaries the contribution provided by this thesis to the prediction of the unstable rock mass behaviour and the possible improvements both for the experimental data analysis and for the unstable rock mass stability analysis;

Along with the abovementioned activities, other research activities were performed during the master’s thesis path. These activities investigated the ultrasonic propagation in the sample in different moments (before cutting, after cutting, after thermal treatment and after the rupture) in order to investigate any structural difference.

Chapter 1

Stability analysis of the cliff of Madonna del Sasso

The site that has been chosen for the stability analysis is the cliff of Madonna del Sasso ($45^{\circ}79'N$, $8^{\circ}37'E$) that is located in NW Italy, on the western shore of the Orta Lake (Figure 1.1a). It consists in a granitic slope bounded on three sides (N, E and S) by pseudo vertical walls, with a height of about 200 m (Figure 1.1b). A XVIII-century sanctuary, from which the site takes his name, stands on the top of the cliff (650 m. s. l.). At the bottom of the slope, between the cliff and the lake, there are several buildings, and a road (SP 46) connecting the towns on the western shore of the lake. An intense mining activity on the bottom of the cliff, lasting until few decades ago, gave it the current steep morphology.



Figure 1.1: Geographical localitation (a) and aerial view (b) of the cliff of Madonna del Sasso cliff

1.1 Geological framework

The area is totally characterized by a granitic rock mass, known as granite of Alzo. This unit belongs to the non-metamorphosed, and generally low deformed, granitic masses, related to a larger NE-SW elongated Permian batholith [1].

From a geomechanical point of view [2] [3], the rock mass is intact but affected by widely spaced joint sets with good surface quality. Four main discontinuity's family were identified (dip direction/dip): K1 (110/75), K2 (0/80), K3 (150/15) and K4 (50/75). These fractures (Figure 1.2) tend to isolate two frontal portions of the slope (sectors A and B), with an estimated total volume of about 12000 m³. Sector A is delimited by fractures K2 and K1 on the sides and truncated at the base by K3 system, with a volume of about 4500 m³. Sector B, on the other hand, is bounded by the joints K2 and K4 on the side and truncated at the bottom by K3 system, with a volume of about 7500 m³. The K4 discontinuity shows clear evidence of displacement, but on the contrary, K2 fracture reveals the widest opening (around 40 cm) with a significant persistence within the rock mass and apparently no filling material in the first superficial meters of observation (Table 1.1).

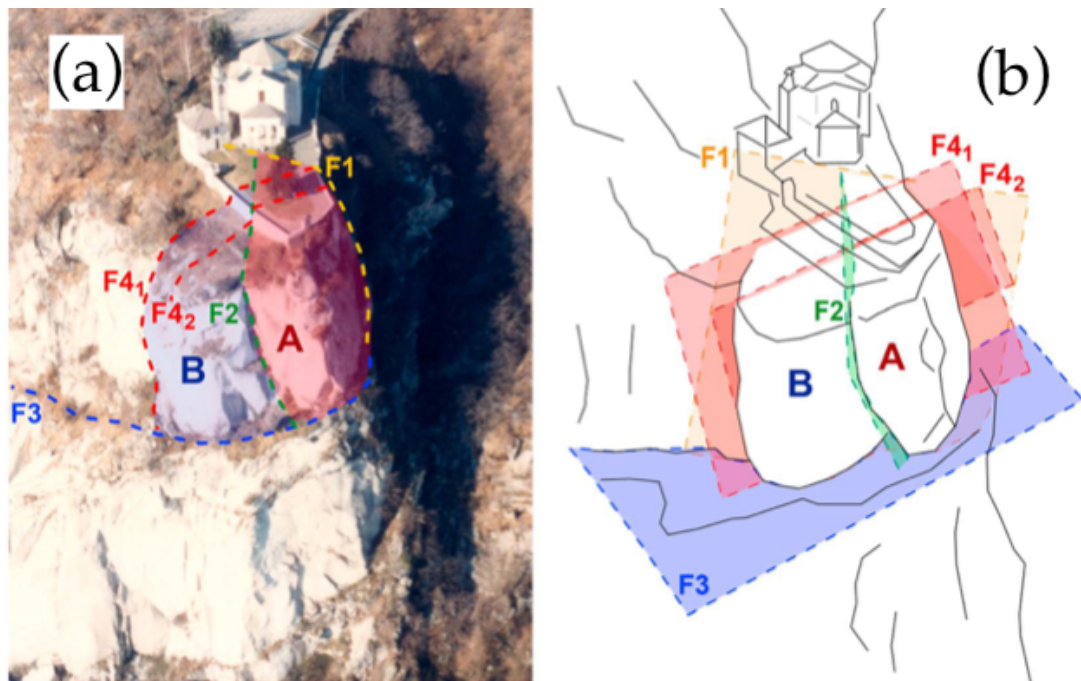


Figure 1.2: Aerial view (a) and schematic representation (b) of the major fracture traces and discontinuity planes [3]

Table 1.1: Joint sets parameters from the geomechanical characterization carried out by Lancellotta et al. [1991]

Joint set	Dip direction	Dip	Opening [cm]	Persistence	Depth [m]
K1	110°	75°	-	-	-
K2	0°	80°	50	significant	45
K3	150°	15°	-	-	-
K4	50°	75°	-	significant	16±2

In occasion of isolated phenomena (winter 2013, spring 2015) when, after long-lasting intense rainfalls, several damages and confined collapses occurred in the grassy yard at the top of the cliff, bringing to light the deep and open chasms related to fractures of the K4 and K2 systems. For this reason, a micro-seismic monitoring network was placed in situ [4][5], and then a network of 10 automatic crackmeters coupled with temperature probes was installed for the displacement monitoring of sector A. Five of them were deployed on the northern side following the K4 fracture, and the others were placed on the southern cliff following K2 fracture at different heights. The monitoring results suggested that the joint opening is directly connected to the mean air temperature and displacements are interpreted as the outcome of rock-mass thermal contraction, with a maximum displacement over the winter, and a minimum over the summer, related to the thermal expansion. At the end of an annual cycle of observation, three probes went back to the initial zero-value while seven sensors preserved a residual opening of an average of 2 mm/year. The maximum opening value was 5-6.1 mm/year. Even if, up to now, relevant irreversible changes have not been detected by the various adopted monitoring systems, there is an increasing awareness in population of the risk related to the site.

1.2 Introduction to LEM theory

The limit equilibrium method (LEM) is one of the most used approach in the geotechnical field for the evaluation of rock slope stability. It investigate the equilibrium of a soil or rock mass tending to slide down under the influence

of gravity. Translational or rotational movement is considered on an assumed or known potential slip surface below the soil or rock mass. The LEM also allows to perform the back-analysis of a failed slope, so that we can study the causes of the collapse and compute the operative shear strength parameters during the failure.

The simplicity of the LEM is based on three main assumptions. First of all, the real case is reduced in a two-dimensional problem, with the critical slip surface represented by a line (Figure 1.3) and sections analysed assuming plane strain condition. Furthermore, the shear strengths of the materials along the potential failure surface are governed by a failure criterion and, in our case, we assume the Mohr-Coulomb's one. This means that, at each point of the slip surface, the shear strength is given by

$$\tau'_f = c' + \sigma'_n \tan\phi' \quad (1.1)$$

where c' is the intercept cohesion and ϕ' is the friction angle.

The unstable body is in limit equilibrium condition when the shear stress is equal to the shear strength at any point of the slip surface. In fact, the output of the analysis is a factor of safety F_s

$$F_s = \frac{\tau_f}{\tau} \quad (1.2)$$

defined as the ratio of the shear strength τ_f (or, alternatively, an equivalent measure of shear resistance or capacity) to the shear stress τ (or other equivalent measure) required for equilibrium. If the safety factor value is less than 1.0, the slope is unstable in that analysed condition. The last hypothesis is to have a constant factor of safety along the slip surface, namely that all the points of the slip surface are using the same quantity of shear strength. This assumption is fundamental for the LEM application, but it is clearly false.

The LEM does not consider soil displacements prior, during or after slope failure and does not involve any constitutive law for the behaviour of the soil. Although these limitations often make the LEM inaccurate for a soil mechanics analysis, it appears that it is particularly precise in rock slope engineering for a simple block failure along distinct discontinuities. The validity of this method was confirmed over the years through back-analysis and comparison with finite element methods. Furthermore, the simplicity of the LEM makes it suitable for the proposing and the assessment of remedial works.

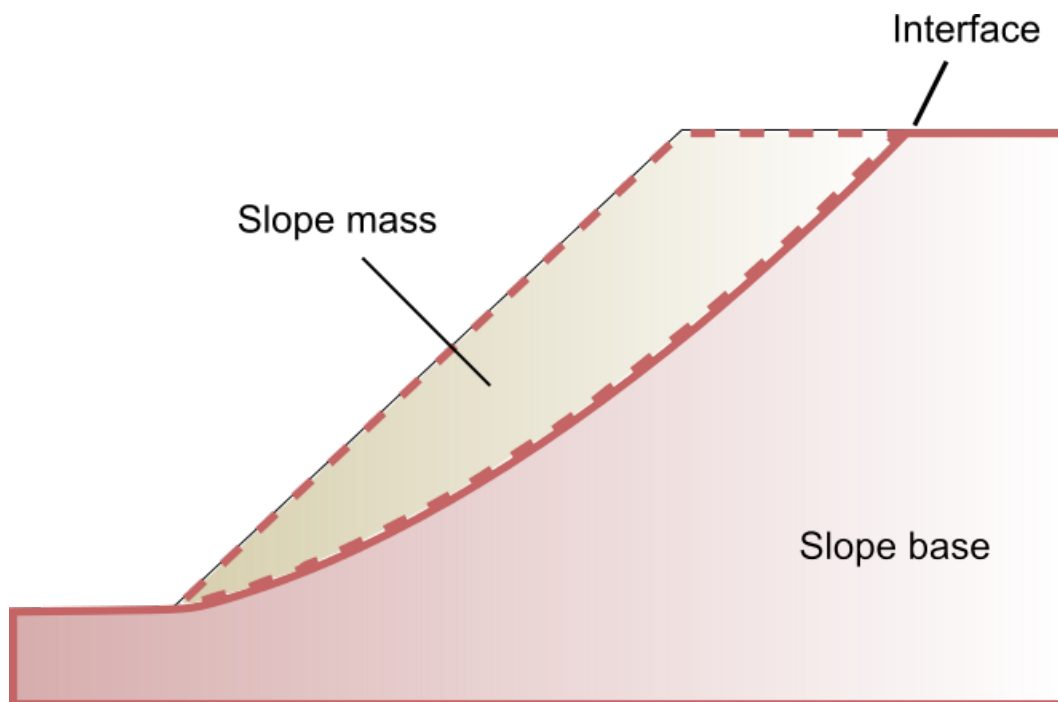


Figure 1.3: A typical cross-section of a slope used in two-dimensional analyses

1.3 Static analysis

The purpose of the static analysis is to establish the most dangerous breaking mechanism of the analysed cliff. Indeed, in rock mechanics, there are three main failure modes: planar sliding, wedge sliding and toppling.

1.3.1 Planar sliding

Planar sliding: the failure surface in planar failures are resulted by structural discontinuities like bedding planes, faults or the interface between weathered rock and the underlying bedrock. This kind of failure leads to sliding action along the failure surface. Hence, planar failure occurs in response to a single discontinuity (Figure 1.4). The following conditions are necessary for a planar failure:

- The strikes of both the sliding plane and the slope face lie parallel ($\pm 20^\circ$) to each other;
- The dip angle of the failure plane should be less than the dip angle of the slope face;
- The dip of the sliding plane is greater than the friction angle;

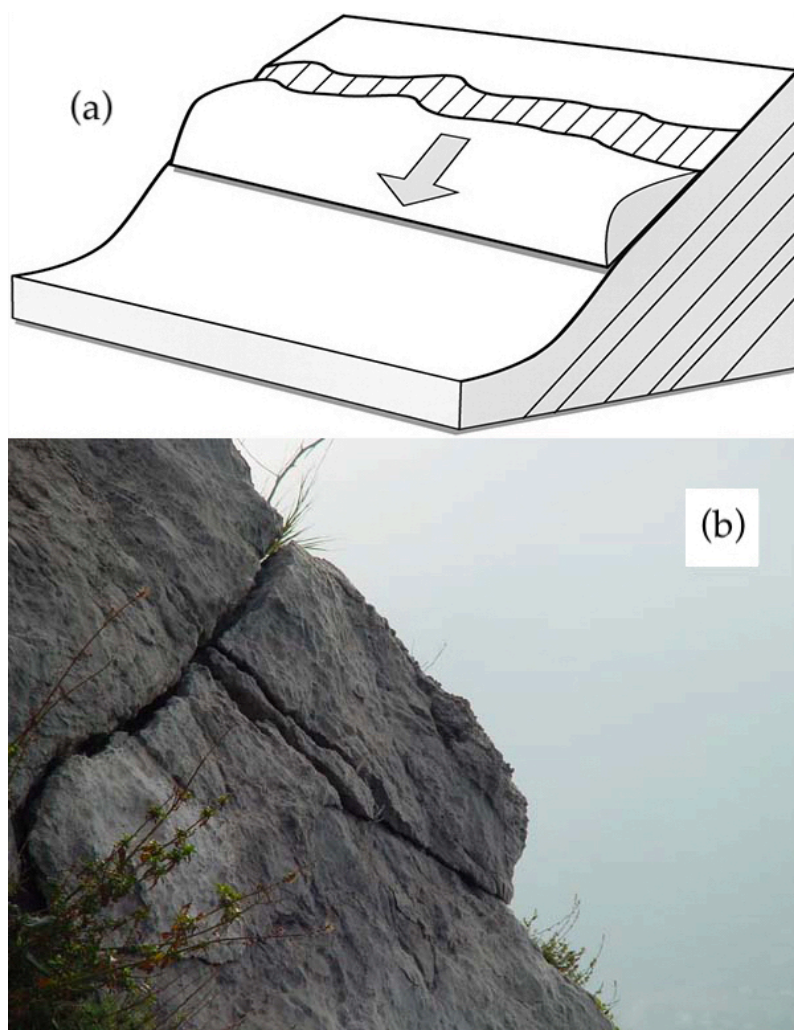


Figure 1.4: Schematic representation (a) and a real example (b) of a planar sliding [6]

1.3.2 Wedge sliding

This kind of failure causes a rock mass to slide along two intersecting discontinuities (Figure 1.5). This mode of failure needs the dip angle of at least one joint intersection to be greater than the angle of friction of the joint surface. Favourable lithology for the development of wedge failure includes inclined bedding, foliation and well defined cleavages. Rocks such as shale, limestone and slate are more prone to this kind of failure due to its internal form. Structural conditions are also necessary for the propagation of wedge failure:

- The plunge line of the intersection should be greater than the friction angle of the slope;
- The dip angle of the intersection should be less than the dip angle of the slope;

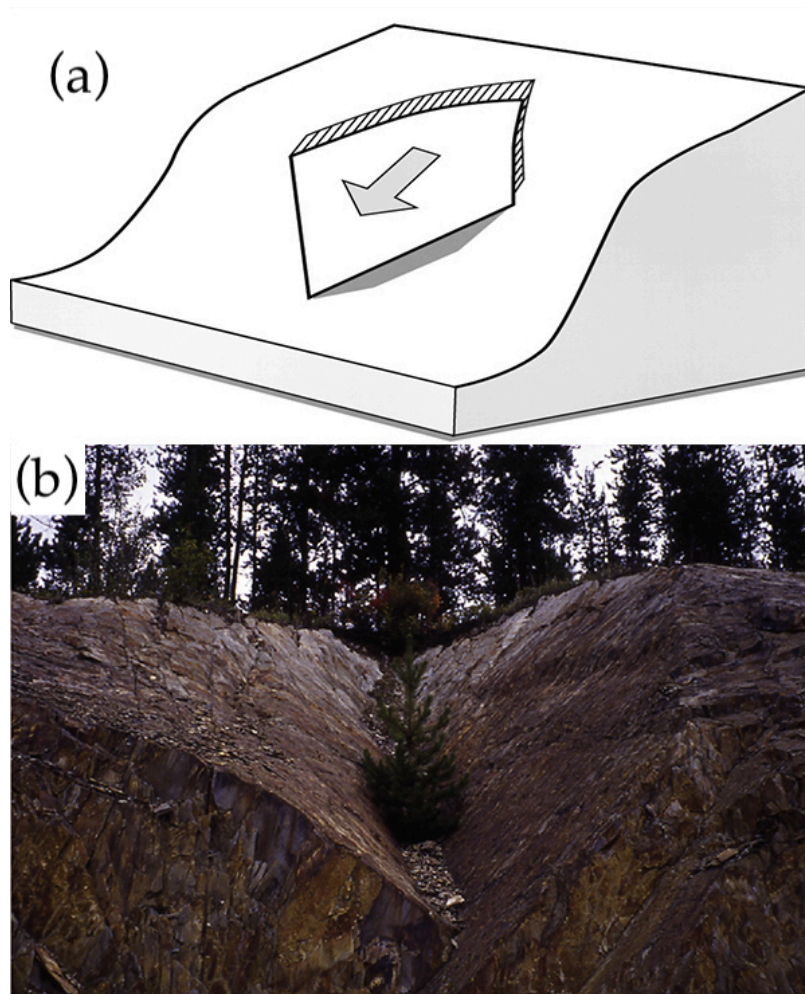


Figure 1.5: Schematic representation (a) and a real example (b) of a wedge sliding [6]

1.3.3 Toppling

Toppling failure occurs due to steep discontinuities in the rock which eventually leads to slippage of the layers and the outward and downward movement of a column of rock (Figure 1.6). Prerequisites for toppling failure include closely spaced jointed rock mass with steep discontinuities dipping away from the slope face. Sometimes the removal of an overburden load, that was previously imparting constraining stresses in the rock structure, could instigate toppling.

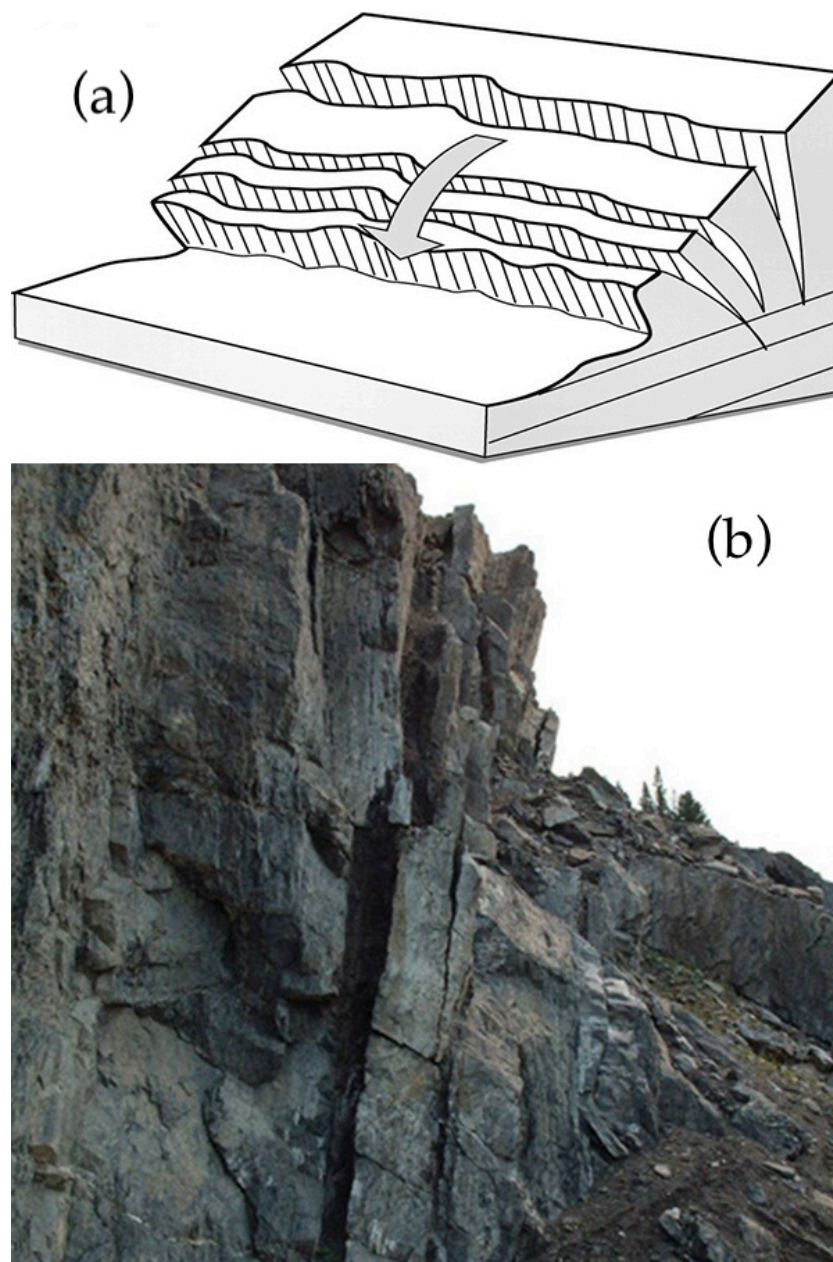


Figure 1.6: Schematic representation (a) and a real example (b) of a toppling failure [6]

1.3.4 Stereographic investigation

The static study begins in situ, where the geologist performs surveys (small or large scale) in order to identify the main discontinuity's family and fractures. They are defined with the dip, the steepest angle of descent of a tilted bed or feature relative to a horizontal plane, and the dip direction, the azimuth of the direction the dip as projected to the horizontal. In our case report, as better discussed in the section 1.1, the cliff of Madonna del Sasso is characterized by four main discontinuity's family. The next step is to represent the joint's plane and the slope's walls on a stereogram with the aim of detect all the possible failure's mechanism. The following stereographic analysis was carried out using the software "Dips 6.0" of the RocScience suite (Figure 1.7).

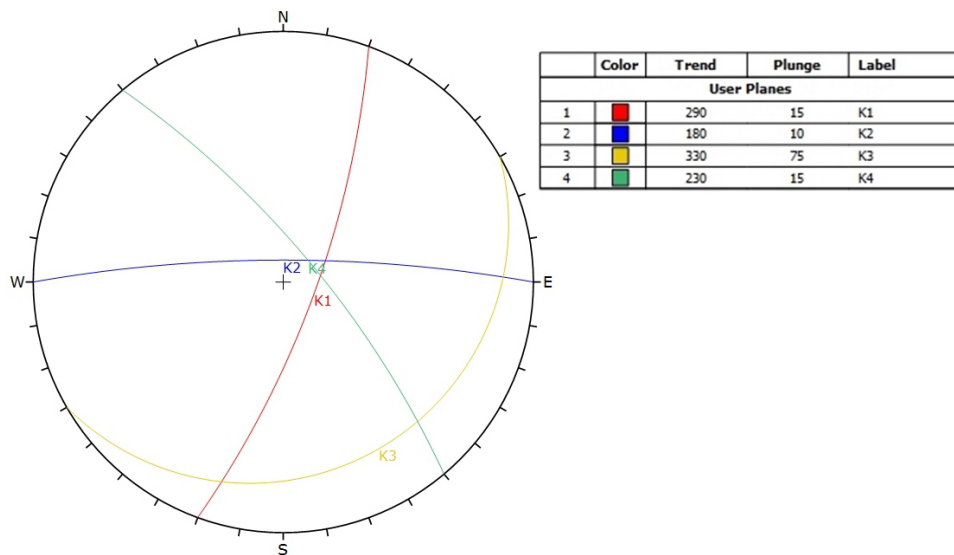


Figure 1.7: Stereographic view of the four joint's families detected by Lancellotta in 1991

The stereographic analysis revealed that the sector A is subject to a mechanism of planar sliding along the discontinuity K2. There are also two potential wedge sliding mechanisms between the joints K2, K4 and K1, but for the stability analysis it will be enough to study the planar sliding's failure, since the three-dimensionality of the wedge sliding provides greater stability to the rock mass. The sector B, on the contrary, is subject to a planar sliding's mechanism along the discontinuities K1 and K4, because of the presence of slopes both in North and in East direction. Since the height of the two sides is almost identical, it will therefore be necessary to consider the discontinuity

with the steepest inclination. In our case, these two joint's families have the same dip angle, so it is reasonable to evaluate the stability along any discontinuity. There are wedge sliding mechanisms even for the sector B, but it is possible do not consider them for the reason mentioned before.

1.4 Geometrical and geomechanical data assumptions

The next step of the stability analysis is to identify the forces acting on the unstable rock mass, so it is fundamental to identify the geometrical and geomechanical cliff's parameters in this regard. As discussed in the section 1.1, the total volume of the sector A is about 4500 m³, while it is equal to 7500 m³ for the sector B, while the height of the unstable rock masses is about 40 m (Figure 1.8). As far as rock density is concerned, the average value was about 2600 kg/m³ in the geophysical characterization carried out by Colombo in 2016 [7]. Finally, since the absence of a detailed investigation of the in situ rock's mechanical characteristics, it is appropriate to choose low mechanical parameters of granite from the literature. In our case, I assumed a cohesion of 35000 kPa and a friction angle of 35°, because the in situ granite looks intact.



Figure 1.8: Qualitative analysis of the height of the unstable rock mass with Google Earth Pro

1.5 Analysis of forces

A proper assessment of the forces acting on the rock mass is a fundamental step for an accurate stability assessment. In this phase, the civil engineer is responsible for considering all the possible scenarios which may lead to the slope failure. For this reason, negative events such as earthquakes and joint's saturation usually are analysed for the computation of the factor of safety. Indeed, in the planar sliding case, it can be defined as the ratio of the sum of resisting forces N_r to the sum of sliding forces N_s

$$F_s = \frac{N_r}{N_s} \quad (1.3)$$

For the present study, I decided to focus the attention on four scenarios: gravitation case, joint's saturation case, seismic action case and finally an extreme case, that is the combination of a seismic and joint's saturation events.

1.5.1 Gravitation case

In the gravitation case, the weight force and the cohesion are the only actions that affect the body mass. In particular, the weight force act along the vertical direction while the cohesion is distributed along the discontinuity (Figure 1.9). This is the easiest case and a starter point for all the more detailed analysis.

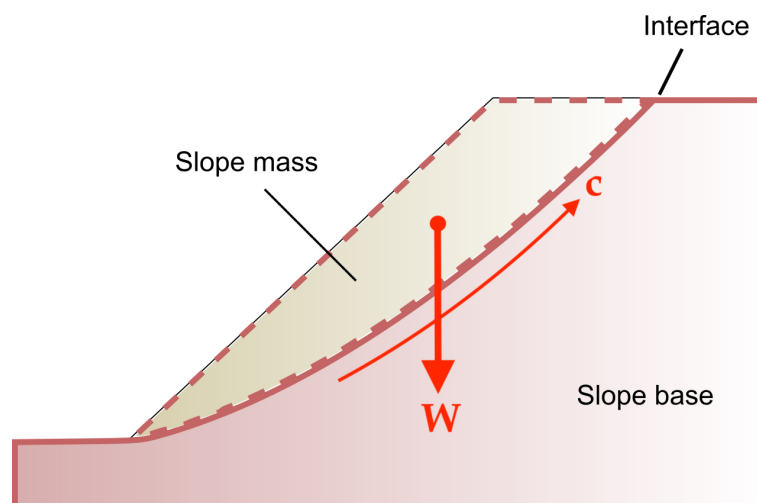


Figure 1.9: Representation of cohesion and weight force vectors on the unstable slope model

The orthogonal to the joint component of the weight force and the cohesion define the resisting force, instead the parallel one characterises the sliding force. Hence, the generic equation 1.3 can be written as

$$F_s = \frac{W \cos(\psi_d) \cdot \tan(\varphi_p) + c \cdot \sum l_i}{W \sin(\psi_d)} \quad (1.4)$$

where W is the total weight force, c represents the cohesion located at the discontinuity level, while φ_p and ψ_d are respectively the friction angle and the joint dip.

Finally, $\sum l_i$ is the sum of the lengths of all the rock bridges along the discontinuity. However, since the persistence value is not known, I choose to vary its value between 99% and 100% in order to study the worst possible scenario. And in so doing, the stability analysis is done in safety conditions.

1.5.2 Joint's saturation case

In the joint's saturation case, the water pressure along the discontinuity must be added to the actions that affect the body mass. As indicated in the previous section, we want to analyse the worst possible conditions and, therefore, I supposed the discontinuity in a fully saturation state with the absence of water leakage. This leads to a triangular water pressure pattern (Figure 1.10), with the depth H_w equal to the cliff height H . In this saturation case, the water force U can be computed as

$$U = \frac{\gamma_w}{2} \cdot \frac{H_w^2}{\sin(\psi_d)} \quad (1.5)$$

where γ_w is the specific weight of water.

Hence, the generic Equation 1.3 becomes

$$F_s = \frac{(W \cos(\psi_d) - U) \cdot \tan(\varphi_p) + c \cdot \sum l_i}{W \sin(\psi_d)} \quad (1.6)$$

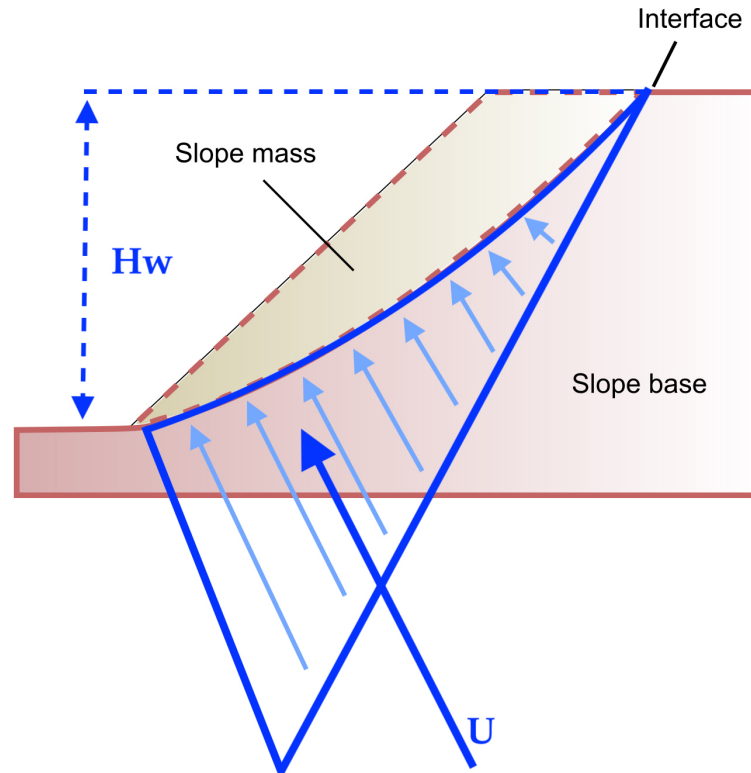


Figure 1.10: Representation of water pressure vectors on the unstable slope model

1.5.3 Seismic action case

In the seismic action case, the evaluation of the earthquake effects is crucial for a consistent analysis. One of the most used approach for the seismic assessment is the Newmark method. It allows to consider the earthquake in the rock slope stability study adding two new forces to the limit equilibrium analysis: a vertical force F_v and an horizontal force F_h (Figure 1.11). The aim of this method is to simulate the hole dynamic action of an earthquake through the application of a constant force for the entire time duration of the event. These two forces are defined as

$$F_v = W \cdot K_v \quad F_h = W \cdot K_h \quad (1.7)$$

where K_v and K_h are respectively the vertical and horizontal seismic coefficient. The norm suggests to evaluate the horizontal action the double of the vertical one $K_h = 2K_v$. The horizontal coefficient is computed as

$$K_h = \frac{a_{max}}{g} \beta \quad (1.8)$$

where g is the gravitational acceleration, and β is a reduction coefficient usually equal to 0.3. Since the vertical and seismic forces are constantly applied for all the duration of the earthquake, the purpose of this factor is to not overestimate the seismic action given that it varies dynamically. Instead, a_{max} is the maximum seismic acceleration that we could observe on the study site and it is defined as

$$a_{max} = a_g \cdot S_s \cdot S_t \quad (1.9)$$

where a_g is the highest peak acceleration read on the seismograph (design acceleration) closer to the site, S_s is a factor that considers the rock nature and the propagation of the elastic seismic waves, and finally S_t is a parameter related to the inclination of the slope.

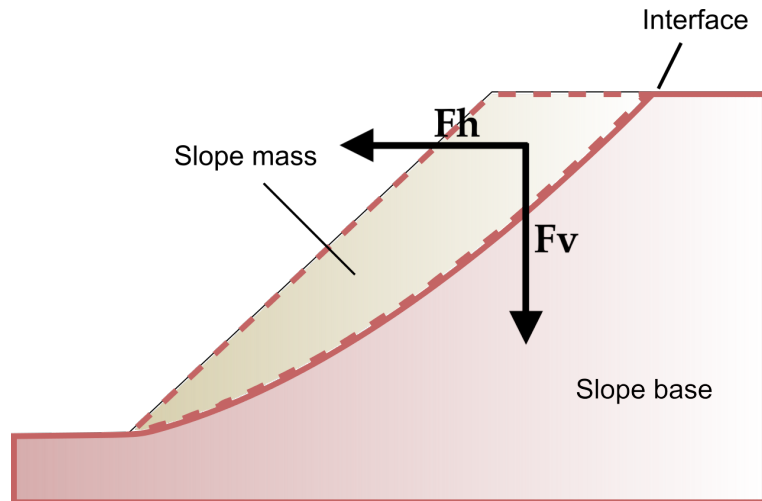


Figure 1.11: Representation of seismic force vectors on the unstable slope model

The site is located in a low seismic risk zone (class 4 according to the INGV institution), hence I assumed a design acceleration of $0.15g$. Then I choose the

ground parameter equal to 1 (typical value recommended for rock mass), and the inclination factor equal to 1.4 (value for very steep slope).

$$a_g = 0.15g \quad S_s = 1 \quad S_t = 1.4$$

Using these parameters, we can compute horizontal and vertical seismic coefficients

$$K_h = 0.063 \quad K_v = 0.0315$$

Finally, the safety factor can be evaluated as

$$F_s = \frac{(W \cos(\psi_d) + F_v \cos(\psi_d) - F_h \sin(\psi_d)) \cdot \tan(\varphi_p) + c \cdot \sum l_i}{W \sin(\psi_d) + F_v \sin(\psi_d) + F_h \cos(\psi_d)} \quad (1.10)$$

1.5.4 Extreme case

In the extreme case, I considered the worst possible scenario with all the forces acting on the unstable slope. The safety factor equation can be obtained by combining the previous formulations:

$$F_s = \frac{(W \cos(\psi_d) + F_v \cos(\psi_d) - F_h \sin(\psi_d) - U) \cdot \tan(\varphi_p) + c \cdot \sum l_i}{W \sin(\psi_d) + F_v \sin(\psi_d) + F_h \cos(\psi_d)} \quad (1.11)$$

1.6 LEM analysis results

The planar sliding mechanism and also a possible toppling mechanism of the entire slope have been analysed. Each stability analysis was performed with the equations and data assumptions described in the previous sections.

1.6.1 Sector A

The sector A is subject to a planar sliding along the discontinuity K2, as described in the stereographic analysis. In the Table 1.2, all the input parameters are enclosed to carry out the LEM analysis, while in the plot

(Figure 1.12) the safety factor is represented in function of the case study and of the persistence.

Table 1.2: Input parameters for sector A analysis

Height [m]	40
Length of discontinuity [m]	40.6
Volume [m ³ /m]	141
Depth [m]	32
Weight [kN/m]	3668
Dip [°]	80°
Cohesion [kPa]	35000
Friction angle [°]	35°
Rock specific weight [kN/m ³]	26
Water specific weight [kN/m ³]	10
Water pressure force [kN/m]	8123
Vertical seismic force [kN/m]	116
Horizontal seismic force [kN/m]	231

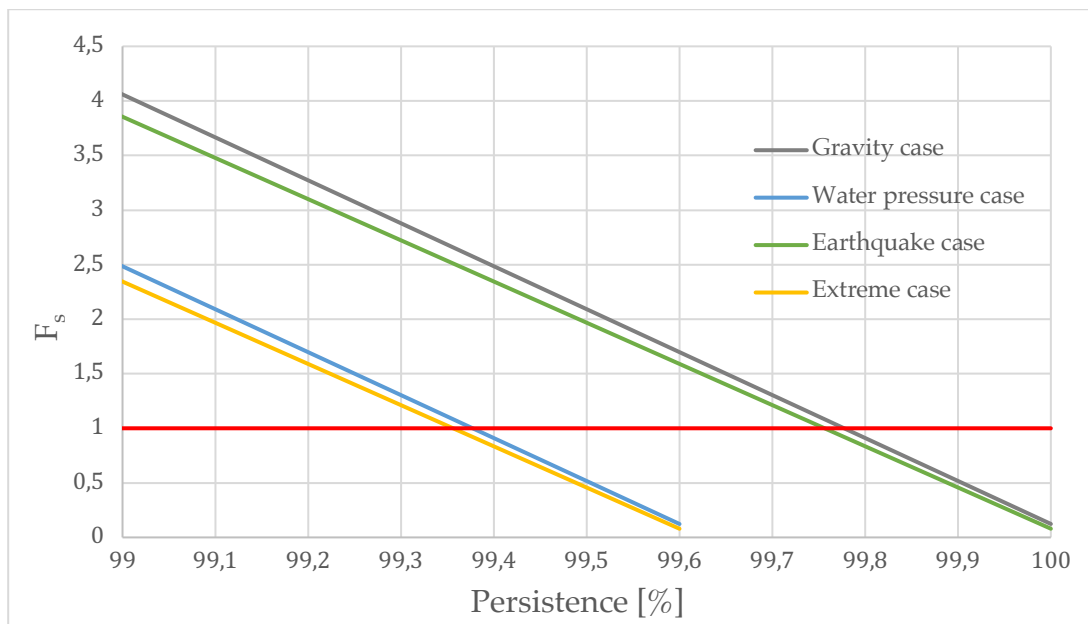


Figure 1.12: LEM analysis of Sector A under four different loading cases

1.6.2 Sector B

The sector B is subject to a planar sliding along the discontinuity K4, as described in the stereographic analysis. In the Table 1.3 are enclosed all the input parameters for the LEM analysis, while in the plot (Figure 1.13) the safety factor is represented in function of the case study and of the persistence.

Table 1.3: Input parameters for sector B analysis

Height [m]	40
Length of discontinuity [m]	41.4
Volume [m^3/m]	214
Depth [m]	29
Weight [kN/m]	5573
Dip [°]	75°
Cohesion [kPa]	35000
Friction angle [°]	35°
Rock specific weight [kN/m^3]	26
Water specific weight [kN/m^3]	10
Water pressure force [kN/m]	8282
Vertical seismic force [kN/m]	176
Horizontal seismic force [kN/m]	351

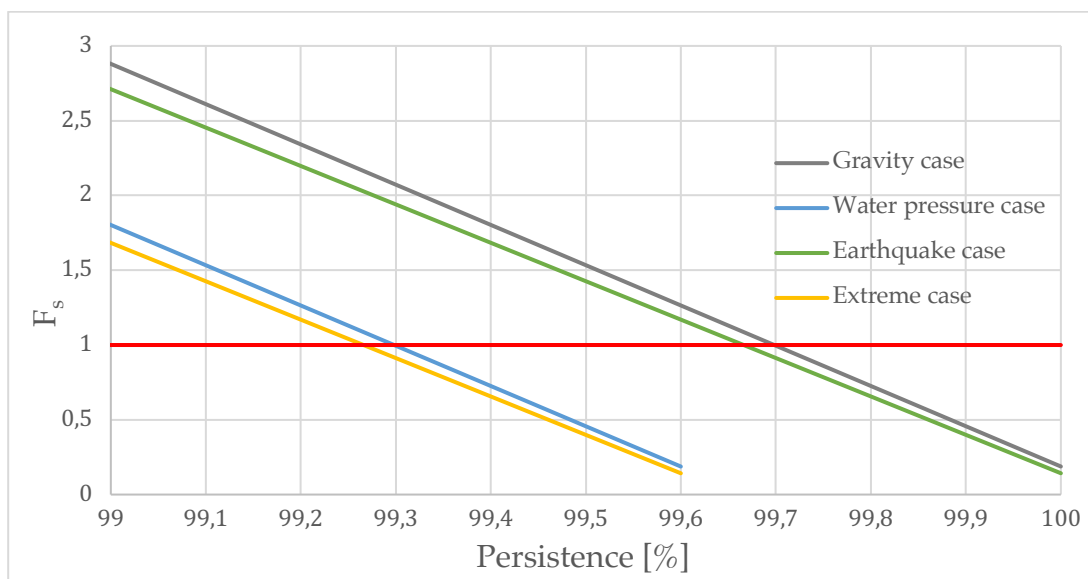


Figure 1.13: LEM analysis of Sector B under four different loading cases

1.6.3 Toppling analysis

The presence of a toppling mechanism can be noticed by observing the whole unstable “Madonna del Sasso” cliff. In particular, the discontinuity K3 represents the sliding plane at the base, while K2 could be considered as a traction joint (Figure 1.2 b). The analysis of the toppling failure must be made by evaluating the safety factor as the ratio between the stabilizing moment M_s and the overturning moment M_o

$$F_s = \frac{M_s}{M_o} \quad (1.12)$$

In presence of the only weight force, this formula becomes

$$F_s = \frac{b}{h} \cdot \frac{1}{\tan(\psi_d)} \quad (1.13)$$

In this way, the safety factor is function only of geometrical parameters such as the width of the unstable slope base b and its height h .

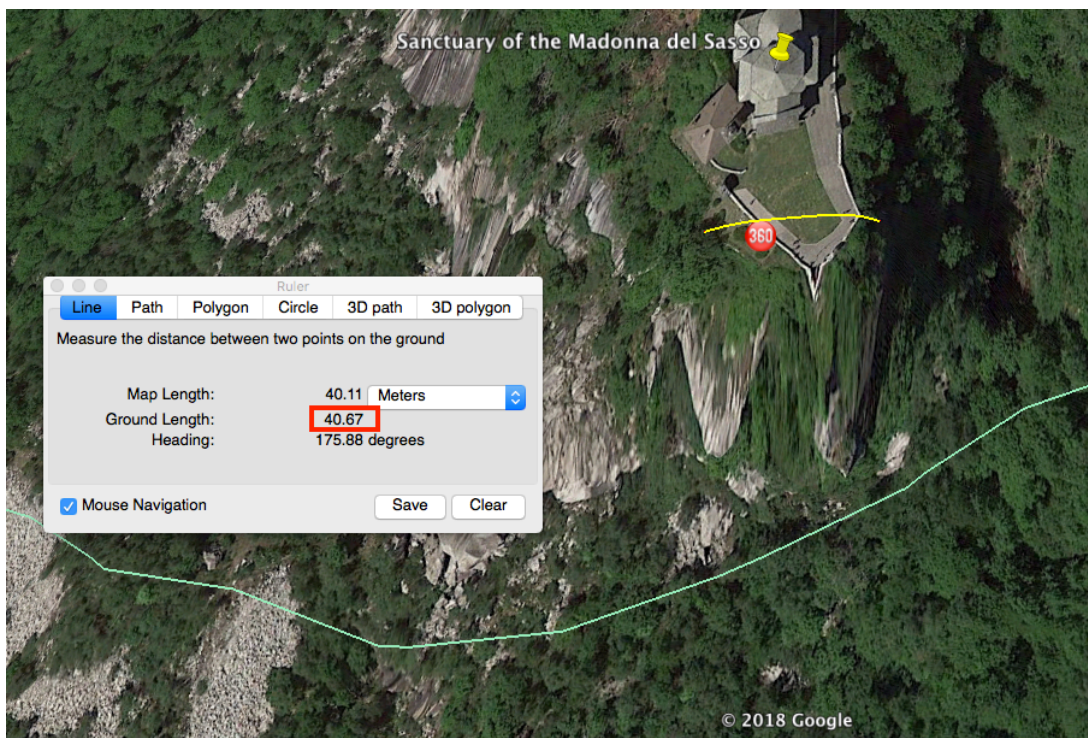


Figure 1.14: Qualitative analysis of the width of the unstable slope with Google Earth Pro

Since the width of the slope is unknown, the following assumption must be done: the width of the blocks A and B is about 40 meters and, then, I assumed a variability of b between 20 and 10 meters, in order to complete the stability study (Figure 1.15). Obviously, this analysis needs additional information such as block geometry and field observations in order to see if a block toppling mechanism is in progress and, for this reason, only the two sliding analyses were chosen for a final comparison.

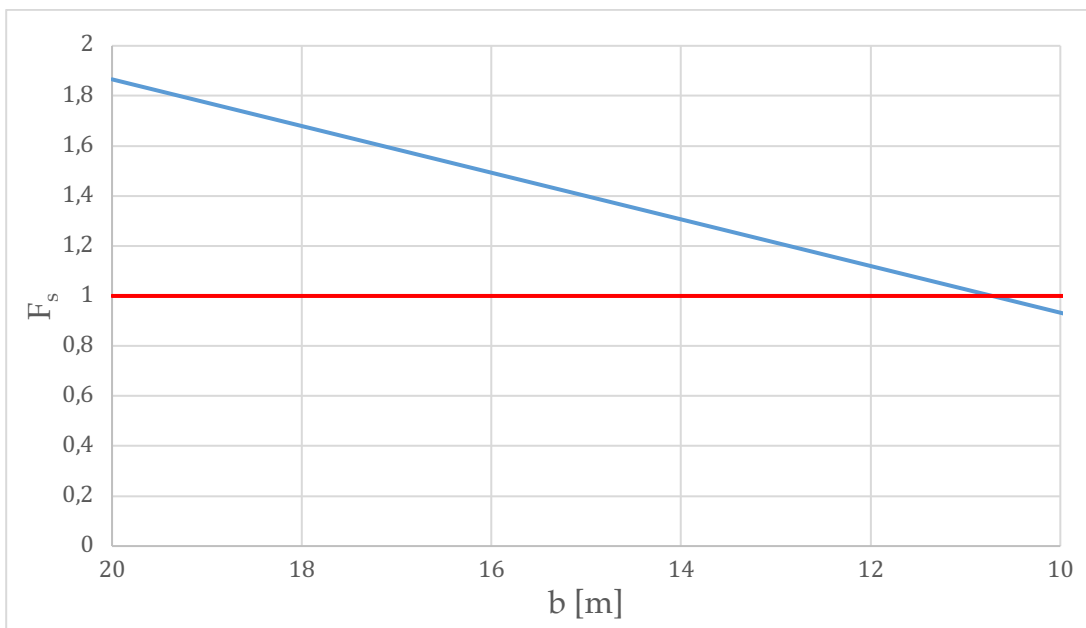


Figure 1.15: Toppling analysis of the unstable cliff

1.7 Concluding remarks

It can be seen that the behaviour of the two sectors is very similar in case of a planar sliding failure (Figure 1.16). The sector A safety factor is pretty bigger for the lower values of persistence and this is due to the smaller volume which leads to lower sliding forces than the sector B. When the persistence increases, instead, the difference between the sector A and sector B factor of safety becomes smaller. This occurs because the cohesion begins to decrease for both sectors and the weight force starts to become more important for the stabilization. In the gravitational case, for example, it is possible to see that the safety factor F_s reaches the critical value before in the sector B (persistence of about 99.7 %) and after with the sector A (persistence 99.8%).

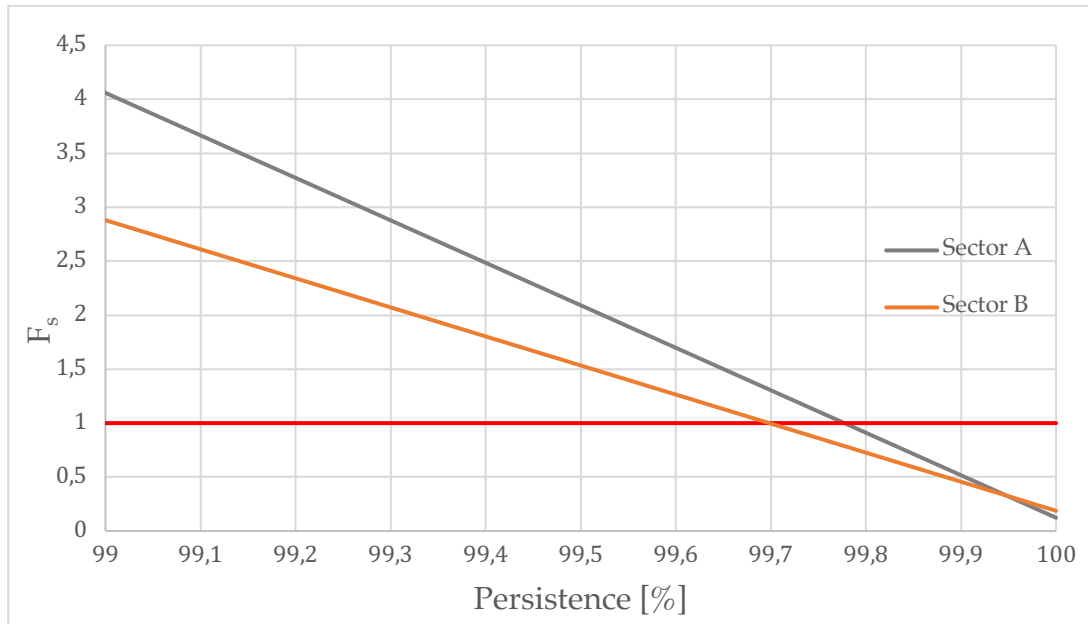


Figure 1.16: Factor of safety comparison between sector A and sector B in the gravitation case

All these considerations were made by considering the discontinuities K_4 and K_2 identical but, in reality, this is not really true: for example the discontinuity K_2 has an aperture of about 50 cm which implies a different behaviour compared to K_4 discontinuity. For this reason, it would be appropriate to perform an analysis of the joint's sets through the 8 parameters ISRM:

- Orientation;
- Spacing and Frequency;
- Continuity or Persistence;
- Roughness;
- Resistance of the walls;
- Opening;
- Filling;
- Infiltration;

In this way it would be possible to estimate parameters such as the "RMR" or the "GSI" index, in order to better characterize the rock slope. For example, the "Hoek and Brown" criterion allows to obtain cohesion and friction angle values of the entire cluster, considering the rock matrix and the discontinuities

as a whole. The potentially unstable rock cliffs behaviour, indeed, is strongly affected by the structural discontinuity pattern affecting the rock mass. Persistence, opening, roughness, and orientation of fractures play, indeed, a fundamental role in the stability of a rock slope. Classical geological surveys and geotechnical analyses on the accessible cliff sides provide useful information about the structural setting, but these data are limited to outcrop observations and they are blind with respect to the inner structure. Finally, the biggest limit of the analysis performed is the lack of mechanical data, in fact, the data used are referred to intact rocks but we need information related to the rock mass. This is the reason why the safety factor obtained is probably higher than the real case.

Chapter 2

Fracture mechanics

The behaviour of rock slopes is strongly affected by their geometric configuration and by the discontinuities in the rock mass. For this reason, in the LEM analysis the rock mass is considered as rigid body and the presence of discontinuities is taken into account by choosing strength parameters lower than the those characteristic of the rock material. However, this continuum assumption leads to ignore the effect of the crack tip stress concentrations. By considering the rock discontinuities as a critical crack, the fracture mechanics offers a new way to study a rock mass stability when the crack tip stress, and hence the propagation of the joints, is the main cause of rock slope instability. In short, LEM analysis is concerned with failure in a continuum sense, where the rock mass undergoes permanent damage, affecting its ability to sustain load. In contrast, fracture mechanics is concerned with the joint propagation. This new approach allows to accurately predict a potential rock mass failure.

2.1 Concepts of linear elastic fracture mechanics (LEFM)

LEFM is based on the assumption [8] that the crack propagation can be studied through the superposition of the effects of three independent loading modes (Figure 2.1). Mode I, which is also called the opening (tensile) mode, is so called because the crack tip is subjected to a normal stress and the crack faces separate symmetrically with respect to the crack front, so that the displacements of the crack surfaces are perpendicular to the crack plane. The crack carries no shear traction and no shear displacement is visible. Mode II is the edge sliding (or in-plane shearing) mode, where the crack tip is

subjected to an in-plane shear stress and the crack faces slide relative to each other so that the displacements of the crack surfaces are in the crack plane and are perpendicular to the crack front. Mode III is the tearing mode, as the crack tip is subjected to an out-of-plane shear stress. The crack faces move relative to each other so that the displacements of the crack surfaces are in the crack plane, but are parallel to the crack front. The Figure 2.2 shows cases of cracks in rock structures subjected to mode I and mode II conditions.

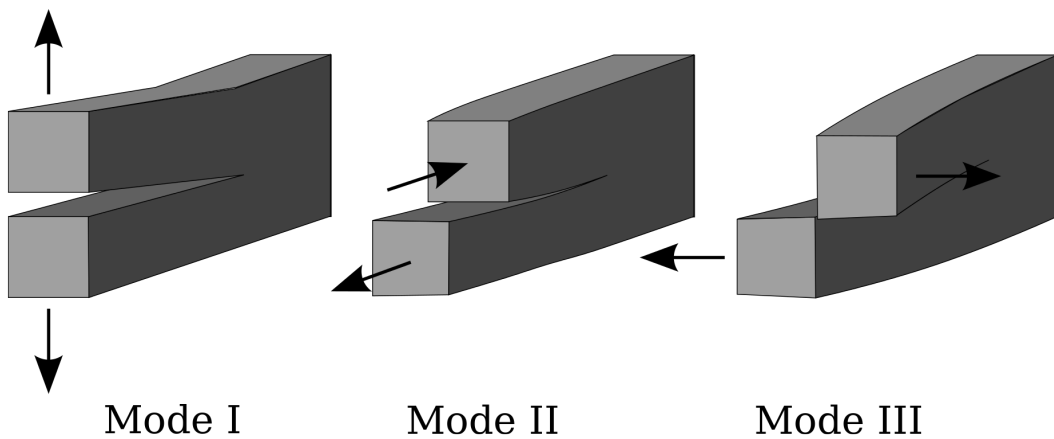


Figure 2.1: Three primary failure modes

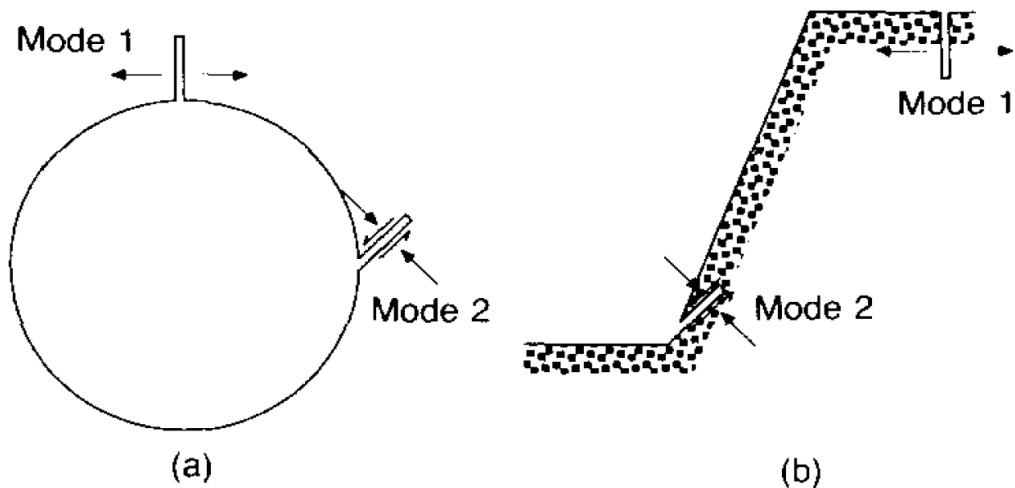


Figure 2.2: Cracks in mode I and mode II conditions in rock structures: (a) tunnel; (b) slope [9]

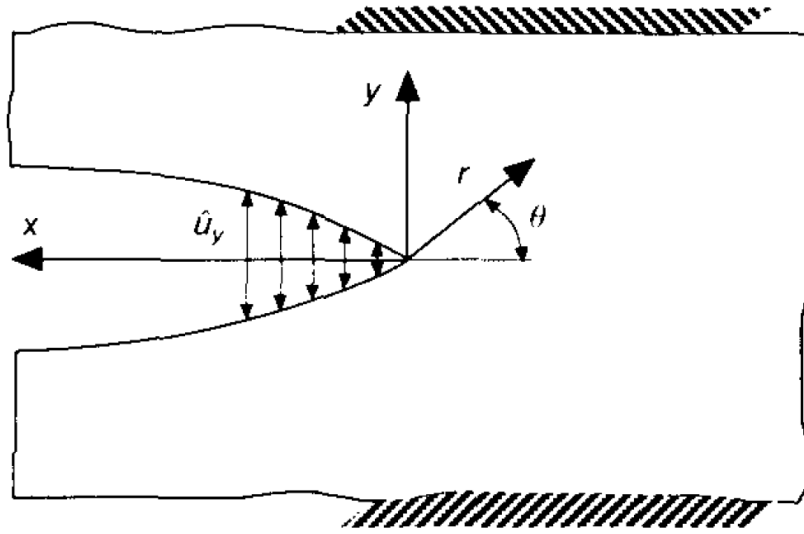


Figure 2.3: Reference axes and variables [9]

LEFM is also based on the stress intensity factor (SIF), K , which quantifies the intensity of the stress singularity at the crack tip. Fracture mechanism states that a crack will propagate when its stress intensity reaches a critical value, K_c , assuming that the crack tip is in a state of planar strain. The state of stress in plane conditions at a point P (Figure 2.3) very close to the crack tip is given as

$$\begin{cases} \sigma_r = \frac{1}{\sqrt{2\pi r}} \cos \frac{\theta}{2} \left[K_1 \left(1 + \sin^2 \frac{\theta}{2} \right) + \frac{3}{2} K_2 \sin \theta - 2K_2 \tan \frac{\theta}{2} \right] \\ \sigma_\theta = \frac{1}{\sqrt{2\pi r}} \cos \frac{\theta}{2} \left[K \cos^2 \frac{\theta}{2} - \frac{3}{2} K_2 \sin \theta \right] \\ \tau_{r\theta} = \frac{1}{2\sqrt{2\pi r}} \cos \frac{\theta}{2} [K_1 \sin \theta + K_2 (3 \cos \theta - 1)] \end{cases} \quad (2.1)$$

where r and θ are the polar coordinates of point P with respect to the crack tip. For $\theta = 0$, i.e. for a point at a distance r along the line of the crack

$$\begin{cases} \sigma_x = K_1/\sqrt{2\pi r} \\ \sigma_y = K_1/\sqrt{2\pi r} \\ \tau_{xy} = K_2/\sqrt{2\pi r} \end{cases} \quad (2.2)$$

In the Equations 2.1 and 2.2, it can be seen that stresses in the immediate vicinity of the tip tend to infinity for $r \rightarrow 0$. This eliminates the traditional strength of materials approach. In these circumstances, even very small loads give rise to stresses at the tip tending to infinity so that the material's finite strength is always exceeded and the crack will invariably propagate.

The meaning of the stress intensity factors can be shown by reference to the simple instance of a crack length $2a$, located in a plate subjected to a uniform vertical tensile stress σ . In this case the vertical stress σ_y around the crack tip is given by the theory of elasticity

$$\sigma_y = \sigma \frac{\sqrt{\pi a}}{\sqrt{2\pi r}} \quad (2.3)$$

Comparison with the Equation 2.2 shows that, whereas the $1/\sqrt{r}$ type variation is common to all crack configuration, the specific boundary condition affect the value of σ_y through a constant term K_1

$$K_1 = \sigma\sqrt{\pi a} \quad (2.4)$$

The value of K is deemed to be representative of the stress field around the crack tip. In fact, because of the extremely high stress values involved, a zone of material exhibiting non-linear behaviour (process zone) always forms at the crack tips, where the actual evolution of stresses is found to deviate from the theoretical elastic values. However, when this zone is small compared with the size of the structure (e.g. in slopes or tunnels), the actual evolution of stresses will still be governed by K , and the LEFM procedure can still be applied.

Finally, the Linear Elastic Fracture Mechanism states that a crack will propagate when its stress intensity factor reaches a critical value K_{IC} (fracture toughness), but natural fractures can grow at lower stress intensities. In such cases, we talk about subcritical crack propagation.

2.2 Fracture mechanism approach

One of the limits of the LEM analysis is the impossibility of considering an evolution over time of the rock's mechanical parameters. The area where the rock formation mostly degrade is concentrated at the discontinuities and at the joints, in fact, if discontinuities are filled with a material that is weaker than the surrounding intact rock, this material might exhibit ductile creep behaviour under shear loading. Furthermore, the asperities along rough joints will likely be concentrators of shear stress, promoting the crack propagation. Therefore, the probability of failure over the life of an unstable rock mass can be much higher compared with the time-independent analysis. A fracture mechanism approach was developed by J. Kemeny [10], where the importance of time-dependence for brittle fractured rock was illustrated. In particular, it is shown that the effects of degradation of rock joint can be evaluated through a time-dependent reduction of rock bridge along the discontinuity. In this model the rock bridge is modelled as a patch of intact material between two coplanar cracks (Figure 2.4). The boundary conditions consist of a rock bridge of width $2a$ contained in a body of width $2w$ under a far-field shear stress τ and normal stress σ_n .

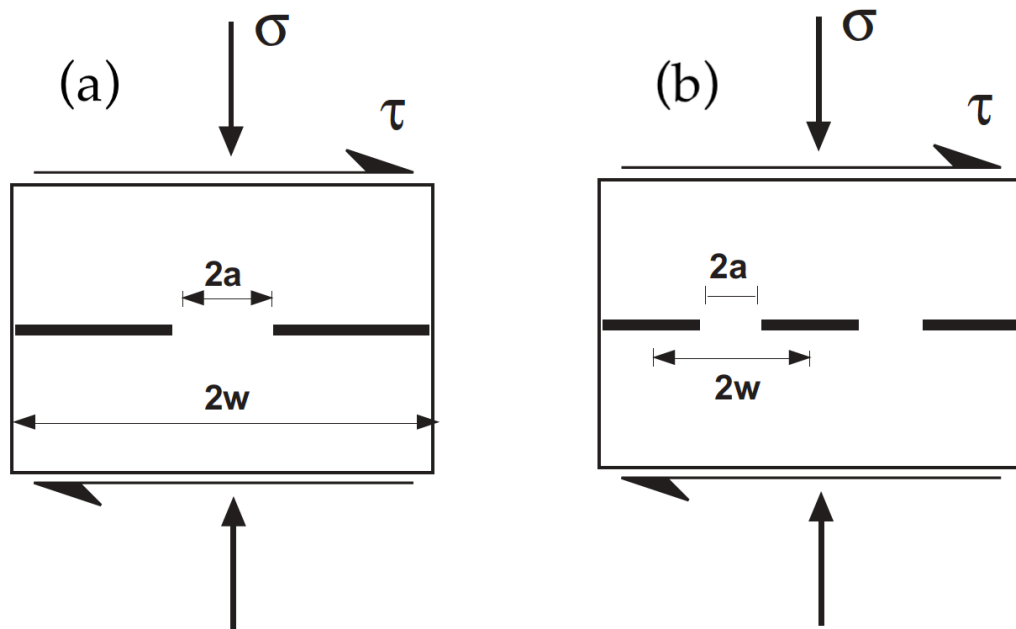


Figure 2.4: Fracture mechanics models, a) single rock bridge under far field normal and shear stresses, b) multiple rock bridges under far field normal and shear stresses [10]

The rock bridge decreases due to subcritical crack growth, which is analysed in a closed-form solution for joint cohesion as a function of time. The formulation for the reduction of the rock bridge, thus, is developed on the subcritical crack growth theory and it is a function of applied loads and of time. Furthermore, tests on rock fractures subjected to quasi-static loading or creep indicate a power-law dependence of crack velocity on the stress intensity factor. According to the Charles power-law [11], the variation of rock bridge width over the time is given by:

$$a'(t) = A \left(\frac{K_I}{K_{IC}} \right)^n \quad (2.5)$$

where $a'(t)$ is the derivative of time-dependent reduction in the rock bridge width, and A and n are subcritical crack growth parameters.

Developing the Charles' power formulation, Kemeny arrived at the following formula:

$$a(t) = \left[a_0^{1+\frac{n}{2}} - \left(1 + \frac{n}{2} \right) At \left[\frac{2w(\tau - \sigma_n \tan \varphi)}{K_{IIC} \sqrt{\pi}} \right]^n \right]^{1/(2+n)} \quad (2.6)$$

where t is the time expressed in seconds. Therefore, the goal is to identify the subcritical crack growth parameters A and n , the mode-I fracture toughness K_{IC} and the mode-II fracture toughness K_{IIC} .

2.3 Fracture toughness testing method

The International Society for Rock Mechanics (ISRM) in 1988 suggested the use of the two-core based specimens with chevron-notches for the determination of static fracture toughness of rock: the Chevron Bend (CB) and the Short Rod (SR) specimens. These two methods to determine rock Mode I fracture toughness have several disadvantages, such as very low loads required to initiate failure, relatively large amounts of intact rock core

required at the correct orientation, complicated loading fixtures and complex sample preparation for SR specimens. A first attempt to solve these problems was done with the Semi-Circular Bend specimen [12], but these limits have been overcome finally with the Cracked Chevron Notched Brazilian Disc (CCNBD) and the Cracked Straight Through Brazilian Disc (CSTBD) specimens which are also suitable for mixed fracture mode testing [13][14][15].

2.3.1 Semi-Circular Bend (SCB) specimen

The specimen is semi-circular in shape and made from typical cores taken from the rock with any relative material directions noted (Figure 2.5). The specimens are tested in three-point bending using a laboratory compression test instrument. The failure load along with its dimensions is used to determine the fracture toughness. Most sedimentary rocks which are layered in structure may exhibit fracture properties that depend on the orientation and therefore measurements in more than one material direction may be necessary. The fracture toughness measurements are expected to yield a size-independent material property if certain minimum specimen size requirements are satisfied [12]. The advantages of using the SCB specimens are represented by the small material requirement per specimen, the relatively simple machining and the only maximum compressive load required to determine the fracture toughness.

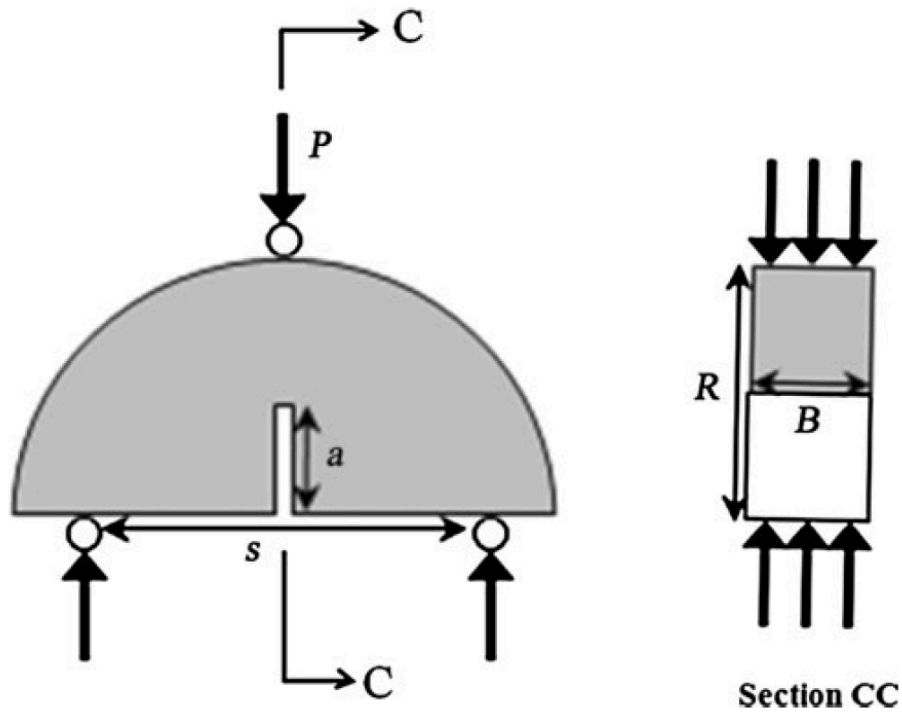


Figure 2.5: SCB specimen geometry and schematic loading arrangement [12]

2.3.2 Cracked Chevron Notched Brazilian Disc (CCNBD) specimen

The main advantage of the CCNBD specimen is the possibility to achieve a complete anisotropic fracture toughness investigation because the crack orientations of three specimens can be easily arranged to be orthogonal to each other if they are machined from the same rock core. The general case for the cracked Brazilian disc problem is when the sample is loaded diametrically with the crack inclined at an angle θ to the loading direction (Figure 2.6). In this way, different combinations of mode I and mode II fractures intensities can be obtained simply by changing the angle. For the special case when $\theta = 0^\circ$ the problem is reduced to the mode I fracture situation. For the mode II CCNBD test proposed in the literature, mode II loading is achieved by inclining the notch at a specific angle β with respect to the diametrical loading direction.

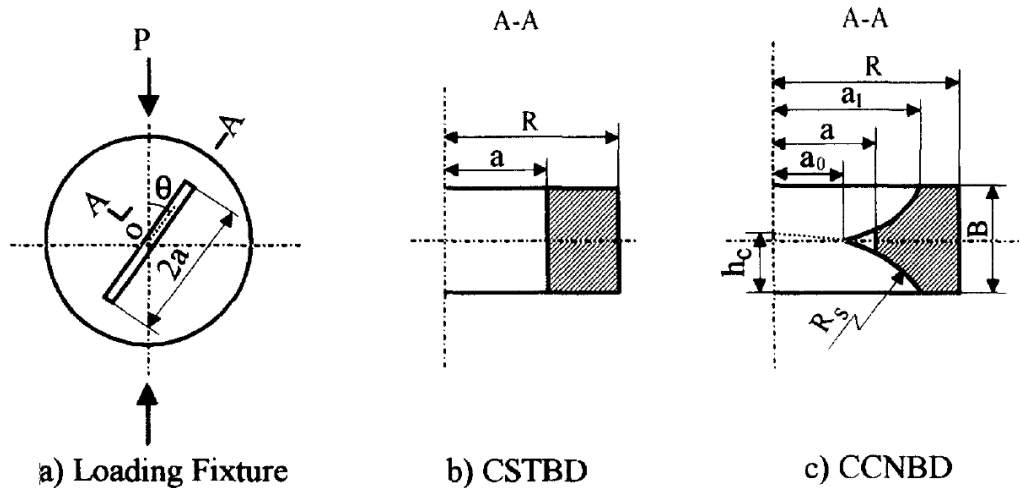


Figure 2.6: CSTBD and CCNBD specimen geometries [14]

Additional advantages are also the higher failure loads and the larger tolerance on the specimen machining error. The CCNBD specimen is characterized by a chevron or “V-shaped notch” cut along the core diameter. The chevron notch causes a crack propagation which starts from the tip of the V alignment proceeds radially outwards in a stable fashion until the point where the fracture toughness is evaluated. Finally, the CSTBD specimen is very similar to CCNBD one, but there is the difference in the shape of the notch cut that is straight and not “V”-shaped, and this leads to a lower stability in the crack propagation.

2.3.3 Discussion about the most suitable test

After the description of the suggested method to determinate the fracture toughness, it was decided to perform the tests using the CCNBD specimen: it allows to analyse mixed modes in a simple way (by the rotation of the specimen), and it requires only an ordinary laboratory equipment. In addition, it has been proved theoretically and experimentally that the failure load of the CCNBD rock specimen is respectively 6.6 times and 15 times bigger than the CB and SR specimen’s failure load. This is of great significance for engineering purposes as the accuracy requirement on the testing rigs’ low load range test abilities and the system error can be reduced. Finally, I preferred the CCNBD instead of the CSTBD specimen because the chevron notch causes a crack propagation that starts from the tip of the V alignment

and proceeds radially outwards in a stable fashion until the point where the fracture toughness is evaluated. On the contrary, in the CSTBD specimen, the propagation of the fracture is less controlled.

Table 2.1: Comparison between the various rock fracture toughness testing methods

Item of comparison	CCNBD	CSTBD	SCB	CB	SR
Method of obtaining mixed-mode	Rotate specimen	Rotate specimen	Vary notch angle	None	None
Size of specimen	Small	Small	Small	Long	Small
Preparation apparatus	Simple	Simple	Simple	Simple	Complex
Set-up of equipment	Simple	Simple	Simple	Complex	Complex
Loading machines	Compressive	Compressive	Compressive	Compressive	Tensile
Loading method	Compressive loading	Compressive loading	Three-point bending	Three-point bending	Tensile loading
Reproducible data	Excellent	Excellent	Excellent	Reasonable	Reasonable
Requirement of testing machine	Ordinary	Ordinary	Ordinary	High	High
Behaviour of fracture propagation	Stable	Unstable	Unstable	Stable	Stable
Method of obtaining mixed-mode	Rotate specimen	Rotate specimen	Vary notch angle	None	None
Size of specimen	Small	Small	Small	Long	Small
Preparation apparatus	Simple	Simple	Simple	Simple	Complex

Chapter 3

Preliminary characterization of granite of Alzo

The goal of the preliminary characterization is to verify if the two granite blocks (“granite of Alzo”) have the same properties and consequently if they could be used for the same fracture toughness investigation. Little differences are expected since the two blocks of granite seem to have a slightly different mineralogical composition. Several tests were carried out for the characterization of the rock block A and the rock block B such as: the evaluation of porosity, P- and S-wave velocity (dry and saturated case), and electrical tests (with different solutions). The samples of the two rock block have been named respectively GA and GB with the addition of the corresponding number. Some parameters (Formation Factor, Tortuosity, crack density, aspect ratio) have been identified, through the processing of the data, in order to make a comparison between the two rock blocks. As we can see on the following pages, in according to existing works [16][17], elastic properties in rocks are strongly affected by thin microcracks naturally present in the rock microstructure. Because P- and S-wave velocities directly depend on the rock elastic constants, those are also strongly effected by microcracks.

The preliminary analysis was carried out through the following steps:

- Samples cutting in disks of height between 1 and 2 *cm*, and with a diameter of about 3.9 *cm*;
- Sample drying in the oven at a temperature of 105° *C* for one week;

- Dry Sample weighing and measuring, Propagation of seismic waves test and Pycnometer test;
- Air removal from the microcracks of the samples which were left to get saturation for a week in a tap water solution (conductivity of 0.33 mS/cm);
- Saturated samples weighing, Propagation of seismic waves test and Electrical test;
- Saturation for a week in a 0.15 % in weight solution of *NaCl* and water (conductivity of 4 mS/cm);
- Saturated samples weighing, Propagation of seismic waves test and Electrical test;
- Saturation for a week in a 1.5 % in weight solution of *NaCl* and water (conductivity of 32.4 mS/cm);
- Saturated samples weighing, Propagation of seismic waves test and Electrical test;
- Saturation for a week in a 3 % in weight solution of *NaCl* and water (conductivity of 50.9 mS/cm);
- Sample drying in the oven at a temperature of 105° C for one week;
- New propagation of seismic waves test on the dry sample;

3.1 Porosity analysis

In granites, no porosity is expected, in fact the porosity that we measured is due to the existence of microcracks. For this reason, the porosity can give information about the internal state of damage of the rock.

3.1.1 Pycnometer test

The pycnometer allows to evaluate the volume of gas particles (such as the Helium) which flow into the microcracks of the rock formation and therefore the volume of the connected pores V_{pores} . The bulk volume V_{bulk} , on the other

hand, can be calculated by using the volume formula of a cylinder (sample's shape):

$$V_{bulk} = \pi r^2 \cdot H \quad (3.1)$$

Consequently the matrix volume V_{matrix} is given by:

$$V_{matrix} = V_{bulk} - V_{pores} \quad (3.2)$$

Finally, the porosity can be evaluated as (Table 3.1):

$$\phi = \frac{V_{pore}}{V_{Tot}} \quad (3.3)$$

Table 3.1: Final result of the Pycnometer test

Sample	V_{bulk} [mm ³]	V_{matrix} [mm ³]	V_{pore} [mm ³]	ϕ [%]
GA1	13370.3	13134.6	235.7	1.76
GA2	14380.5	14133.7	246.8	1.72
GA3	20309.5	19971.7	337.8	1.66
GA4	15138.7	14886.6	252.1	1.67
GA5	12723.6	12489	234.6	1.84
GB1	22100.5	21724.3	376.2	1.70
GB2	20007.9	19681.1	326.8	1.63
GB3	20170.6	19846.9	323.7	1.60
GB4	16380.8	16112.3	268.5	1.64
GB5	16262.9	15999.6	263.3	1.62

3.1.2 Indirect method

Another way to investigate the porosity is represented by the indirect method. It consists of evaluating the porosity ϕ through the comparison of the saturated mass W_{sat} with the dry one W_{dry} . Indeed, a good approximation of the pores volume is given by:

$$V_{pores} = \frac{W_{sat} - W_{dry}}{\rho_{water}} \quad (3.4)$$

where ρ_{water} is the water density which is used to fill the pores.

Since the achievement of a complete saturation is a very long process in rocks like granite, two indirect analyses have been carried out with different time of saturation (1 week and 2 weeks), in order to be sure to have fully saturated samples (Table 3.2).

Table 3.2: Final results of the indirect method to find the porosity

Sample	$W_{d,1w}$ [g]	$W_{s,1w}$ [g]	$W_{s,2w}$ [g]	$V_{p,1w}$ [mm ³]	$V_{p,2w}$ [mm ³]	ϕ_{1w} [%]	ϕ_{2w} [%]
GA1	34.884	34.990	35.002	106.7	118.5	0.80	0.89
GA2	37.855	37.952	37.973	96.5	118.1	0.67	0.82
GA3	52.857	52.992	53.036	134.7	179.3	0.66	0.88
GA4	39.531	39.643	39.661	112	129.6	0.74	0.86
GA5	32.928	32.996	33.028	67.7	99.4	0.53	0.78
GA6	46.565	46.689	46.712	123.6	146.4	0.70	0.82
GA7	47.654	47.780	47.799	125.8	145	0.70	0.80
GA8	40.225	40.328	40.355	103.3	130	0.64	0.81
GB1	57.615	57.870	57.877	255.4	261.9	1.16	1.19
GB2	52.676	52.890	52.894	213.7	218.1	1.07	1.09
GB3	52.690	52.896	52.922	206.3	232.1	1.02	1.15
GB4	42.936	43.106	43.114	170.5	178.7	1.04	1.09
GB5	42.529	42.714	42.716	185.4	187	1.14	1.15
GB6	46.607	46.806	46.810	199.3	203.2	1.11	1.13
GB7	46.980	47.178	47.184	198.2	203.7	1.10	1.13
GB8	45.786	45.972	45.982	185.4	195.4	1.05	1.11
GB9	47.423	47.610	47.619	187	196.1	1.04	1.09
GB10	56.574	56.800	56.808	226.5	233.7	1.05	1.09

3.1.3 Conclusions

First of all, it is possible to observe that the porosities calculated with the Pycnometer test are almost the same for both rock blocks: the average effective porosity is about 1,7 % for the block A (Figure 3.1) and 1,65 % for the block B (Figure 3.2). Much more interesting results have been obtained from the indirect method. In this test, indeed, porosity is lower for both rock blocks compared with the pycnometer's one, and this is probably due to the microcracks which are so small that the water particles cannot access them, on the contrary the helium particles can get in them because they are smaller. Furthermore, the effective porosity difference between the two tests is more accentuated for the samples of block A than those of block B. This could mean that microcracks of block B are globally more accessible from water in a short time. It is clear that after one more week of saturation (2 weeks in total) we expect to obtain a porosity values equal or slightly higher than those previously calculated. From the data obtained, it is possible to identify an increase in porosity much more accentuated in the block A than in B. This could confirm the hypothesis of the presence of more microcracks hardly reachable from water in samples A. Finally, these results show that during the first week the complete saturations was note completely reached.

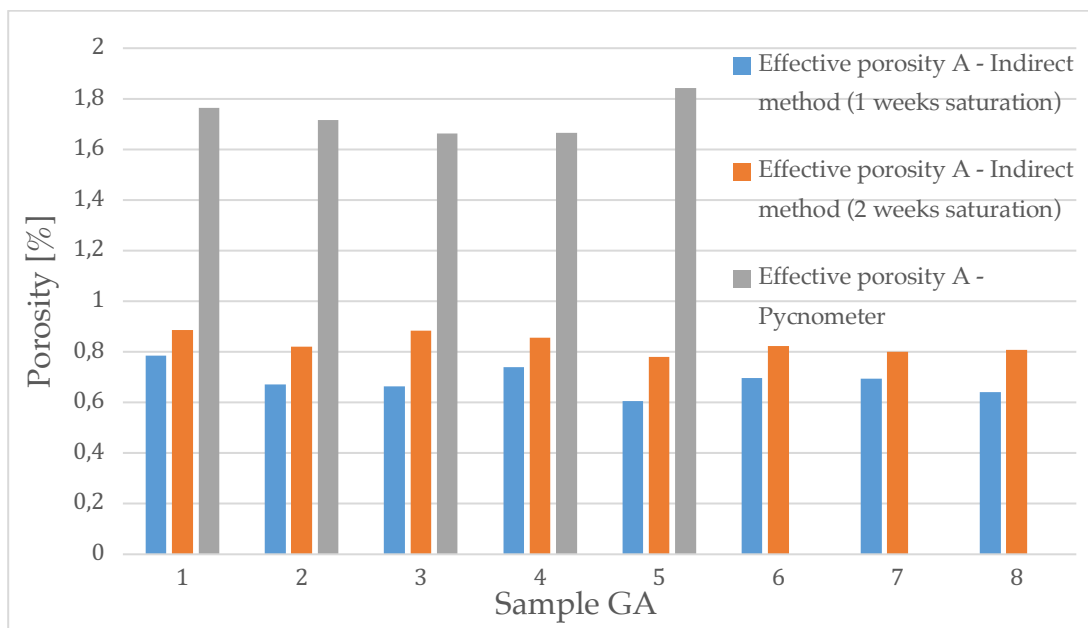


Figure 3.1: Porosity analysis rock A

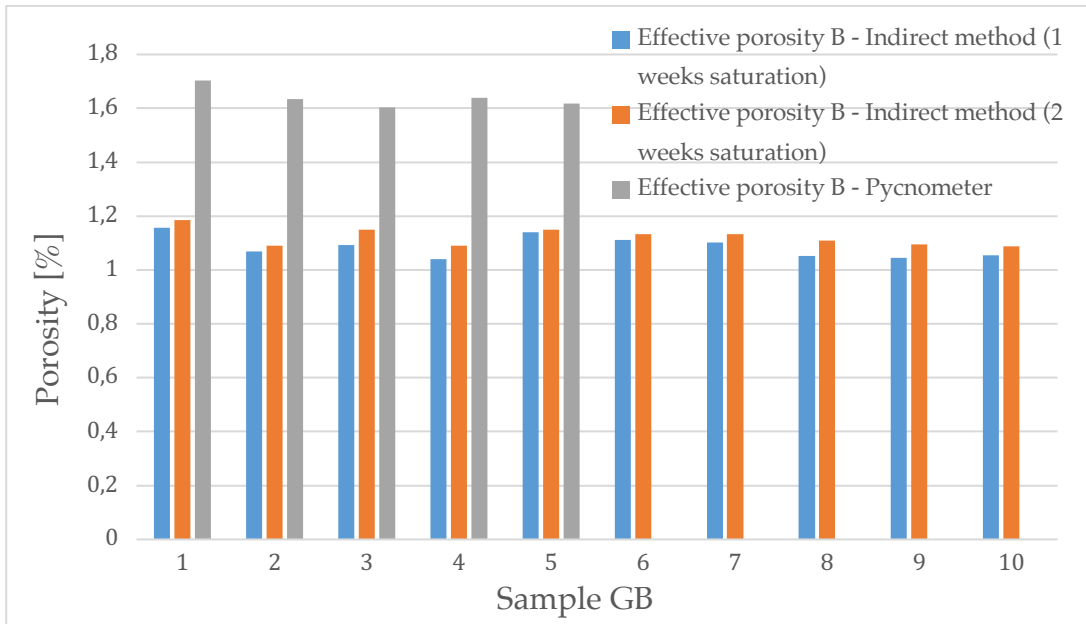


Figure 3.2: Porosity analysis rock B

3.2 Electrical conductivity analysis

The electrical conductivity of a rock formation depends on four kind of electrical conduction:

- Ionic conduction;
- Surface conduction;
- Mineralogical conduction;
- Sulfide conduction;

In the case study, the Sulfide and Mineralogical conductions can be neglected, and we can focus on the Ionic and Surface conductions. In particular, the ionic conduction depends on the pore water conductivity which is related to the temperature, to the kind of ions and to their concentrations. Therefore, an higher salinity solution, through which is saturated the sample, means a more conductive rock formation. Hence, the conduction of the sample saturated with the tap water is expected to be lower than the one of the samples saturated with a salty solution, since the conductivity of the air is practically null.

Through the electrical test, it is possible to calculate the impedance value of the rock samples. This value can be approximated to that of the electrical resistance for a signal frequency value close to 1 kHz. Indeed, in the scientific community, it is a good rule to assume the impedance value obtained by a frequency of 1 kHz as the electrical resistance that often corresponds to a phase close to zero. This choice is necessary because, around this frequency, the resistance values are rather constant, with a low variability, and this allows for replicability of the data in the laboratories. Obviously, the resistance represents an extensive value, and not a parameter of the material. For this reason, it is necessary to calculate the resistivity R through the following relation:

$$R = \frac{r \cdot A}{L} \quad (3.5)$$

where r is the electrical resistance [Ω], R is the electrical resistivity [$\Omega \cdot m$], L is the length of the electrical path [m], A is the cross-sectional area perpendicular to the electrical flow path [m^2].

The value of rock resistivity is influenced by the resistivity of the water that fill the pores of the samples. For this reason, it is necessary to get a dimensionless the value: the Formation Factor F . It is related to the complexity of the electrical flow path inside a rock formation and therefore it is an index of the size, shape and amount of pores channels. According to Waxman & Smith [18], we can define the following formula:

$$C_0 = \frac{C_w}{F} + C_s \quad (3.6)$$

where C_0 is the rock formation conductivity [S/m], C_s is surface conductivity [S/m], C_w is the pore water conductivity [S/m], F is the formation factor. From the first Archies' law, it is possible to compute the formation factor F as:

$$F = a\phi^{-m} \quad (3.7)$$

where, a is an empirical constant (typically $a = 1$ for unconsolidated sediments), m is the cementation index (typically $m = 2$ for unconsolidated sediments), ϕ is the connected porosity.

Finally, in low porosity igneous rocks, the electrical tortuosity τ is more used than the cementation index providing an alternate view at relationships between pore space and electrical transmissivity:

$$F = \tau\phi \quad (3.8)$$

Where τ is related to the geometrical complexity of the path followed by the electrical current in the fractured pore space or, in a more general sense, to the efficiency of electrical flow processes. In the case study, four electrical tests were performed to obtain a better characterization of the rock. These tests differ in the pore water resistivity:

- In the first test, samples were saturated in tap water (conductivity of 0.33 mS/cm);
- In the second test, samples were saturated in a solution of 0.15 % in weight of water and NaCl (conductivity of 4 mS/cm);
- In the third test, samples were saturated in a solution of 1.5 % in weight of water and NaCl (conductivity of 32.8 mS/cm);
- In the fourth test, samples were saturated in a solution of 3 % in weight of water and NaCl (conductivity of 50.9 mS/cm);

In all electrical tests, the conductivity of the solution was calculated by a chemical analysis, except for the third test in which the samples were saturated with a solution of 1,5 % weight of water. In this case, the electrical conductivity of the solution was evaluated by chemical formulation. The electrical conductivity of a fluid S is a function of the ions nature l_i [$\text{mS} \cdot \text{m}^2/\text{mol}$] and their concentrations c_i [mol/L] such that:

$$S = c_1 \cdot l_1 + c_2 \cdot l_2 \quad (3.9)$$

Given that at $25^{\circ}C$, $l_{Na^{+}} = 5.0 \text{ mS} \cdot \text{m}^2/\text{mol}$ and $l_{Cl^{-}} = 7.63 \text{ mS} \cdot \text{m}^2/\text{mol}$, performing the computation also for the different concentrations, we obtain the following data (Table 3.3). Due the similarity between the empirical and theoretical values, we can assume the conductivity approximately equal to 32.4 mS/cm for the third test.

Table 3.3: Electrical resistivity computation

	Na ₊ Cl ₋ 0,15%	Na ₊ Cl ₋ 1,5%	Na ₊ Cl ₋ 3%
C [mol/l]	0.0256	0.256	0.513
S [mS/cm]	3.24	32.4	64.7

The complete chemical analysis is resumed in the following tables (3.4 → 3.7).

Table 3.4: First electrical test on samples saturated with tap water

Sample	H [mm]	D [mm]	r [Ω]	R_r [$\Omega \cdot m$]	C_0 [mS/m]	C_w [mS/m]	R_w [m]	F^* [-]
GA1	11.25	38.90	1843808.0	194783.5	0.005	33.3	0.03003	6486
GA2	12.10	38.90	229632.2	22554.7	0.044	33.3	0.03003	751
GA3	17.08	38.91	343554.7	23917.8	0.042	33.3	0.03003	796
GA4	12.85	38.73	275102.2	25221.8	0.040	33.3	0.03003	840
GA5	10.80	38.73	351364.4	38328.2	0.026	33.3	0.03003	1276
GA6	15.08	38.74	292181.1	22838.1	0.044	33.3	0.03003	761
GA7	15.35	38.74	383254.2	29429.8	0.034	33.3	0.03003	980
GA8	13.00	39.72	706847.3	67373.7	0.015	33.3	0.03003	2244
GB1	18.74	38.75	256109.4	16117.2	0.062	33.3	0.03003	537
GB2	17.08	38.62	246783.7	16925.6	0.059	33.3	0.03003	564
GB3	17.13	38.72	91208.3	6269.6	0.160	33.3	0.03003	209
GB4	13.89	38.75	173163.7	14702.4	0.068	33.3	0.03003	490
GB5	13.79	38.75	167687.5	14340.7	0.070	33.3	0.03003	478
GB6	15.06	38.92	244814.1	19339.6	0.052	33.3	0.03003	644
GB7	15.14	38.90	200166.6	15712.8	0.064	33.3	0.03003	523
GB8	14.83	38.90	290280.4	23263.0	0.043	33.3	0.03003	775
GB9	15.36	38.53	239870.6	18208.5	0.055	33.3	0.03003	606
GB10	18.33	38.63	319864.8	20452.4	0.049	33.3	0.03003	681

Table 3.5: Second electrical test on samples saturated in a 0.15 % salty solution

Sample	H [mm]	D [mm]	r [Ω]	R_r [$\Omega \cdot m$]	C_0 [mS/m]	C_w [mS/m]	R_w [m]	F^* [-]
GA1	11.25	38.90	45476.5	4804.2	0.208	400.0	0.00250	1922
GA2	12.10	38.90	30396.8	2985.6	0.335	400.0	0.00250	1194
GA3	17.08	38.91	40414.1	2813.6	0.355	400.0	0.00250	1125
GA4	12.85	38.73	26678.2	2445.9	0.409	400.0	0.00250	978
GA5	10.80	38.73	20175.7	2200.8	0.454	400.0	0.00250	880
GA6	15.08	38.74	26415.8	2064.8	0.484	400.0	0.00250	826
GA7	15.35	38.74	68548.5	5263.8	0.190	400.0	0.00250	2106
GA8	13.00	39.72	41655.8	3970.5	0.252	400.0	0.00250	1588
GB1	18.74	38.75	24183.6	1521.9	0.657	400.0	0.00250	609
GB2	17.08	38.62	31015.5	2127.2	0.470	400.0	0.00250	851
GB3	17.13	38.72	19061.3	1310.3	0.763	400.0	0.00250	524
GB4	13.89	38.75	21750.5	1846.7	0.542	400.0	0.00250	739
GB5	13.79	38.75	18524.9	1584.3	0.631	400.0	0.00250	634
GB6	15.06	38.92	22964.0	1814.1	0.551	400.0	0.00250	726
GB7	15.14	38.90	21841.2	1714.5	0.583	400.0	0.00250	686
GB8	14.83	38.90	21147.8	1694.8	0.590	400.0	0.00250	678
GB9	15.36	38.53	21754.0	1651.3	0.606	400.0	0.00250	661
GB10	18.33	38.63	24707.0	1579.8	0.633	400.0	0.00250	632

Table 3.6: Third electrical test on samples saturated in a 1.5 % salty solution

Sample	H [mm]	D [mm]	r [Ω]	R_r [$\Omega \cdot m$]	C_0 [mS/m]	C_w [mS/m]	R_w [m]	F^* [-]
GA1	11.25	38.90	7832.7	827.5	1.209	3240.0	0.00031	2681
GA2	12.10	38.90	3698.4	363.3	2.753	3240.0	0.00031	1177
GA3	17.08	38.91	4955.1	345.0	2.899	3240.0	0.00031	1118
GA4	12.85	38.73	4511.5	413.6	2.418	3240.0	0.00031	1340
GA5	10.80	38.73	5452.3	594.8	1.681	3240.0	0.00031	1927
GA6	15.08	38.74	3772.1	294.8	3.392	3240.0	0.00031	955
GA7	15.35	38.74	7573.7	581.6	1.719	3240.0	0.00031	1884
GA8	13.00	39.72	6489.2	618.5	1.617	3240.0	0.00031	2004
GB1	18.74	38.75	3506.7	220.7	4.531	3240.0	0.00031	715
GB2	17.08	38.62	3304.5	226.6	4.412	3240.0	0.00031	734
GB3	17.13	38.72	3141.5	215.9	4.631	3240.0	0.00031	700
GB4	13.89	38.75	4325.0	367.2	2.723	3240.0	0.00031	1190
GB5	13.79	38.75	2617.5	223.9	4.467	3240.0	0.00031	725
GB6	15.06	38.92	2777.5	219.4	4.558	3240.0	0.00031	711
GB7	15.14	38.90	2647.3	207.8	4.812	3240.0	0.00031	673
GB8	14.83	38.90	3310.7	265.3	3.769	3240.0	0.00031	860
GB9	15.36	38.53	3377.6	256.4	3.900	3240.0	0.00031	831
GB10	18.33	38.63	3546.5	226.8	4.410	3240.0	0.00031	735

Table 3.7: Fourth electrical test on samples saturated in a 3 % salty solution

Sample	H [mm]	D [mm]	r [Ω]	R_r [$\Omega \cdot m$]	C_0 [mS/m]	C_w [mS/m]	R_w [m]	F^* [-]
GA1	11.25	38.90	3680.3	388.8	2.572	5090.0	0.00020	1979
GA2	12.10	38.90	1520.1	149.3	6.698	5090.0	0.00020	760
GA3	17.08	38.91	2152.7	149.9	6.673	5090.0	0.00020	763
GA4	12.85	38.73	2612.8	239.5	4.174	5090.0	0.00020	1219
GA5	10.80	38.73	1990.2	217.1	4.606	5090.0	0.00020	1105
GA6	15.08	38.74	1621.6	126.8	7.889	5090.0	0.00020	645
GA7	15.35	38.74	3458.8	265.6	3.765	5090.0	0.00020	1352
GA8	13.00	39.72	2685.0	255.9	3.907	5090.0	0.00020	1303
GB1	18.74	38.75	1299.9	81.8	12.224	5090.0	0.00020	416
GB2	17.08	38.62	1498.0	102.7	9.734	5090.0	0.00020	523
GB3	17.13	38.72	1278.2	87.9	11.381	5090.0	0.00020	447
GB4	13.89	38.75	1882.8	159.9	6.256	5090.0	0.00020	814
GB5	13.79	38.75	977.7	83.6	11.960	5090.0	0.00020	426
GB6	15.06	38.92	1186.7	93.7	10.668	5090.0	0.00020	477
GB7	15.14	38.90	1317.9	103.5	9.666	5090.0	0.00020	527
GB8	14.83	38.90	1313.4	105.3	9.501	5090.0	0.00020	536
GB9	15.36	38.53	1768.6	134.3	7.449	5090.0	0.00020	683
GB10	18.33	38.63	1818.8	116.3	8.599	5090.0	0.00020	592

The formation factor F^* is an approximated value because it has been calculated neglecting the surface conduction C_s . Anyway, it is possible to obtain a graph similar to the Figure 3.3 by plotting the pore fluid conductivity C_w in function of the rock formation conductivity C_0 . The surface conduction can be neglected for high values of the pore fluid conductivity and for this reason the Archie's law is reduced to

$$C_0 = \frac{C_w}{F} \quad (3.10)$$

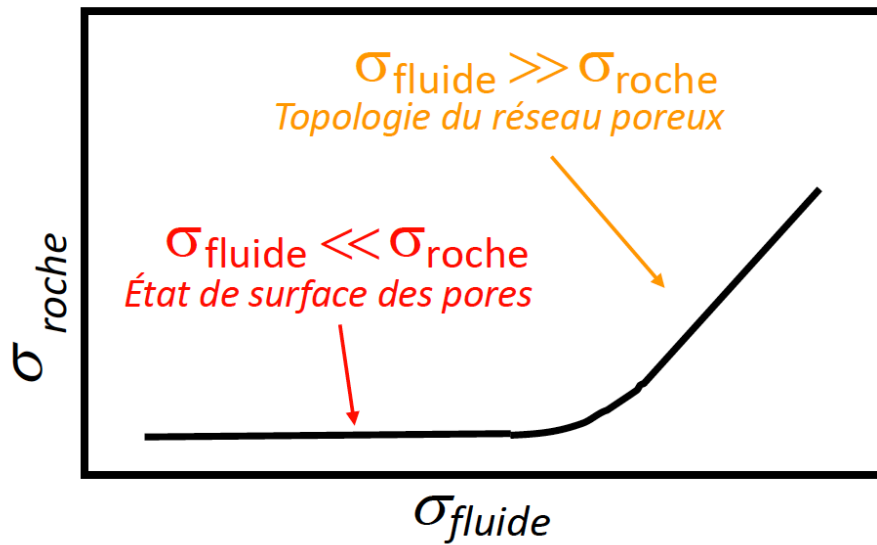
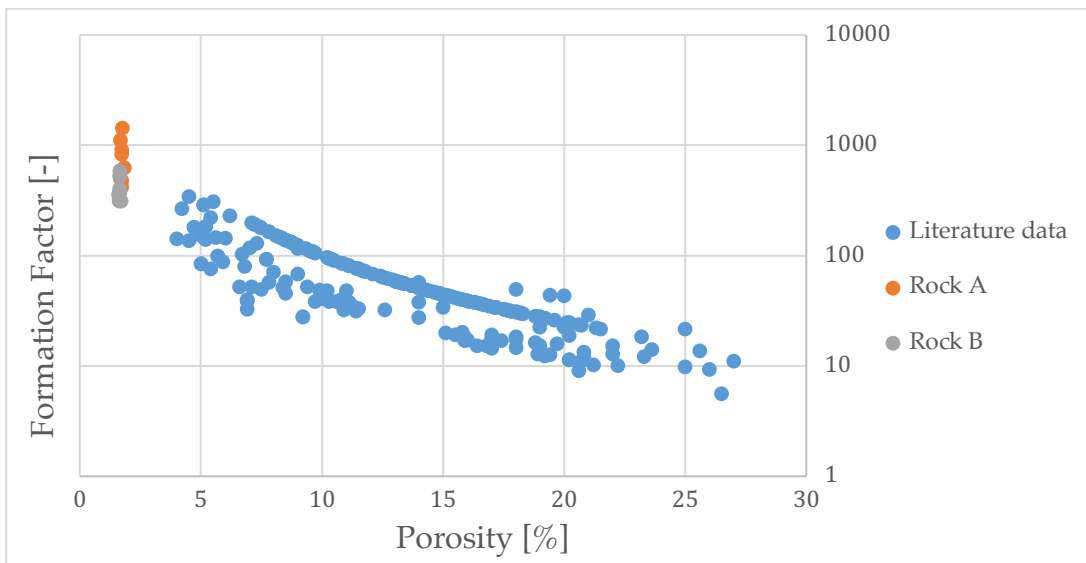


Figure 3.3: Example of fluid's and rock's conductivity relationship (Courtesy of Prof. Violay)

Therefore, the slope of the plot represents the inverse of the formation factor F . On the other hand, when the pore fluid conductivity is low, the surface conductivity is dominant and, for this reason, C_s can be defined as the intercept with the y-axis. In this way, a good approximation of the formation factor and of the surface conductivity have been evaluated, and furthermore the cementation index m and the tortuosity τ were computed by the inverse formula of the Equation 3.7 and 3.8. The porosity found with the pycnometer has been used for the calculations because of the better resolutions, and an average value has been utilized for the sample not analysed for the porosity. It is evident the quite high value of the tortuosity and also of the cementation factor (Table 3.8). This means a great complexity of the electrical flow path, typical of granite rocks. In the Figure 3.4 the actual data of formation factor have been compared with literature's ones and they seem to be consistent. Furthermore, formation factor values are higher for the rock A and this could be due to a greater tortuosity of the microcracks, which could explain why they are less accessible by the water particle.

Table 3.8: Formation factor, tortuosity and cementation index of the samples

Sample	H [mm]	D [mm]	ϕ [%]	F [-]	C_s [mS/m]	m [-]	τ [-]
GA1	11.25	38.90	1.76	1429	0.0252	12.8	2519
GA2	12.10	38.90	1.72	476	0.0067	11.4	817
GA3	17.08	38.91	1.66	500	0.0056	12.2	832
GA4	12.85	38.73	1.67	1111	0.0633	13.8	1850
GA5	10.80	38.73	1.84	625	0.0213	10.5	1152
GA6	15.08	38.74	1.73	417	0.0377	11.0	721
GA7	15.35	38.74	1.73	909	0.0198	12.4	1573
GA8	13.00	39.72	1.73	833	0.0251	12.3	1442
GB1	18.74	38.75	1.70	313	0.0574	10.8	532
GB2	17.08	38.62	1.63	400	0.0218	12.2	653
GB3	17.13	38.72	1.60	357	0.1047	12.4	573
GB4	13.89	38.75	1.64	526	0.025	12.7	863
GB5	13.79	38.75	1.62	313	0.0532	11.9	506
GB6	15.06	38.92	1.64	370	0.0063	12.0	607
GB7	15.14	38.90	1.64	385	0.0165	12.0	631
GB8	14.83	38.90	1.64	385	0.0644	12.0	631
GB9	15.36	38.53	1.64	526	0.0049	12.7	863
GB10	18.33	38.63	1.64	588	0.0461	12.9	965

Figure 3.4: Formation factor F and pycnometer porosity ϕ

3.3 Ultrasonic propagation test

The ultrasonic propagation test is one of the most important analysis for the characterization of the elastic properties of rocks. In fact, it is possible to compute fundamental elastic parameters such as Young's modulus E , Poisson's ratio ν , shear modulus G , bulk modulus K , P-wave modulus M , Lamé's coefficient λ . The purpose of the test is to identify the time travel ΔT of the P- and S- ultrasonic waves which pass through the sample, and then to compute their velocities. Thus, it is essential to calculate initially the height H of the cylindrical specimen and then to use the following formula for speed:

$$V = \frac{H}{\Delta T} \quad (3.11)$$

The experiment procedure is very simple, in fact, the cylindrical sample is placed between two piezoelectric transducers and an electric pulse is converted into a seismic wave by the first piezoelectric transducer and it is sent to the specimen. On the other side of the sample, the other piezoelectric transducer converts the seismic wave into an electric signal, which is displayed on an oscilloscope (Figure 3.5). It is essential to choose adequately the wavelength, which should be bigger than grainsize and not too much bigger than the sample (usually 1 MHz of frequency). In the setup there was also a 10x signal amplifier that allowed me to have easier data to analyse. The precision of the measurement of the time interval is equal to 10^{-2} microsecond. Two tests were carried out on the dry specimens because, during the first test, the results related to the P- seismic wave velocity were too difficult to interpret due to the background noise. On the contrary, during the second test, cleaner graphics have been obtained. For this reason, only the data obtained during the second analysis are considered. In the Figures 3.6 and 3.7, it is possible to observe the difference of data noise between the first and the second dry test. Finally the ultrasonic propagation test was done also for saturated sample in order to identify the variation of the propagation velocity (Table 3.9 and 3.10).

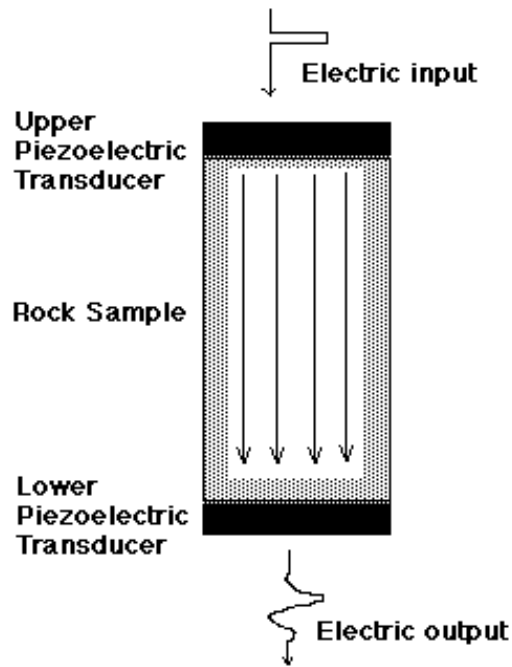


Figure 3.5: Pulse transmission sketch

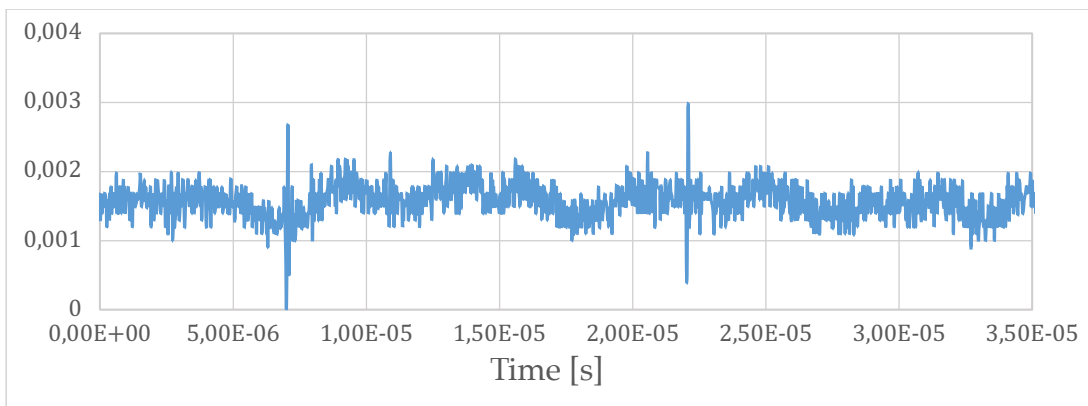


Figure 3.6: P wave of the dry GB1 sample (test 1)

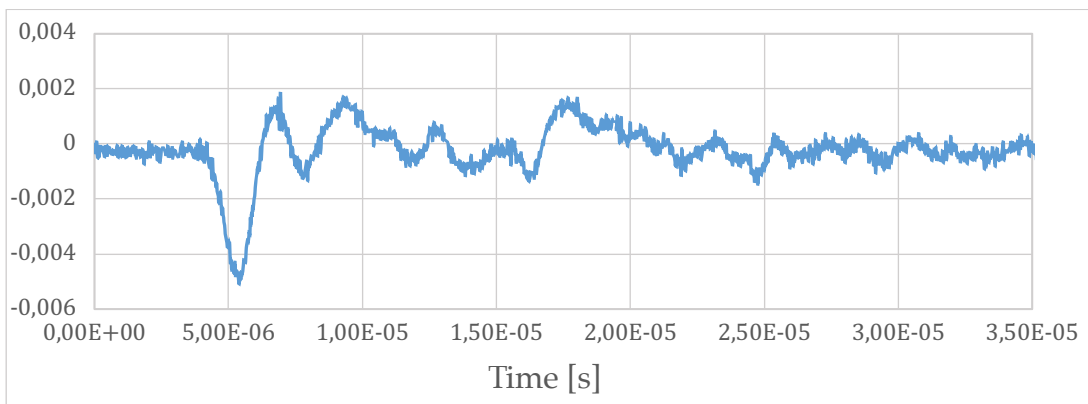


Figure 3.7: P wave of the dry GB1 sample (test 2)

Table 3.9: Final results of the seismic test on the rock A

Sample	$V_p(\text{Dry})$ [m/s]	$V_s(\text{Dry})$ [m/s]	$V_p(\text{Sat 1w})$ [m/s]	$V_s(\text{Sat 1w})$ [m/s]	$V_p(\text{Sat 2w})$ [m/s]	$V_s(\text{Sat 2w})$ [m/s]
GA1	3430	2296	5625	2961	5859	3108
GA2	3580	2101	5708	2867	5874	3010
GA3	3573	2333	5405	2866	5770	2945
GA4	3278	2100	5310	2907	5841	3134
GA5	3699	2379	5806	2951	5870	2967
GA6	3507	2089	5756	3116	5669	3195
GA7	3473	2180	5367	2822	5643	2822
GA8	3533	2338	5556	2708	5752	2802
Average	3509	2227	5567	2900	5785	2998

Table 3.10: Final results of the seismic test on the rock B

Sample	$V_p(\text{Dry})$ [m/s]	$V_s(\text{Dry})$ [m/s]	$V_p(\text{Sat 1w})$ [m/s]	$V_s(\text{Sat 1w})$ [m/s]	$V_p(\text{Sat 2w})$ [m/s]	$V_s(\text{Sat 2w})$ [m/s]
GB1	4021	2421	5645	3023	5679	3042
GB2	4028	2271	5770	3028	5849	3018
GB3	4178	2379	5672	2943	5907	3027
GB4	4159	2420	5836	3186	5836	3186
GB5	3918	2353	5843	3078	5843	3177
GB6	4070	2383	5837	2820	5837	2953
GB7	4092	2388	5649	2957	5735	2992
GB8	4213	2447	5839	3014	5885	3051
GB9	3938	2502	5408	2954	5565	2920
GB10	3917	2477	5623	3076	5875	2938
Average	4053	2404	5712	3008	5801	3030

The average propagation velocities of the seismic P- and S-waves are similar for the two rock blocks, but not identical. On average, there is a greater propagation speed in the B specimens than in the A samples. The difference in velocity could be due to a slightly different structure of the rocks, and this could be supported by different formation factor F of the two rocks. Furthermore, it should be recalled that the A samples have also a slightly

higher porosity, and consequently this could explain the lower seismic waves propagation than the B samples (Figure 3.8 and 3.9). On the other hand, analysing the results of the seismic wave propagation in saturated specimens, it is possible to notice that there is an important increase in velocities in both rocks samples and it is important to underline how the difference in speed that we had between A and B samples decreases in an important way compared to the case of dry samples (Figure 3.10):

- For the P waves velocity, the difference goes from about 500 m/s to 150 m/s ;
- For the S waves velocity, the difference goes from about 180 m/s to 100 m/s ;

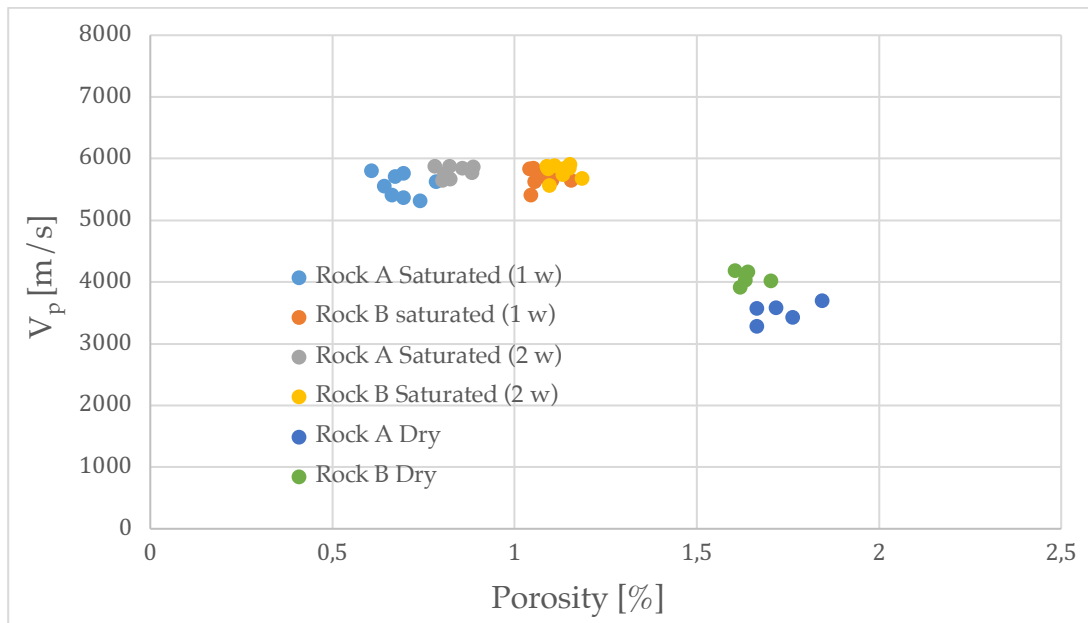


Figure 3.8: (V_p - porosity) plane comparison between saturated samples (1 week), saturated samples (2 weeks) and dry samples

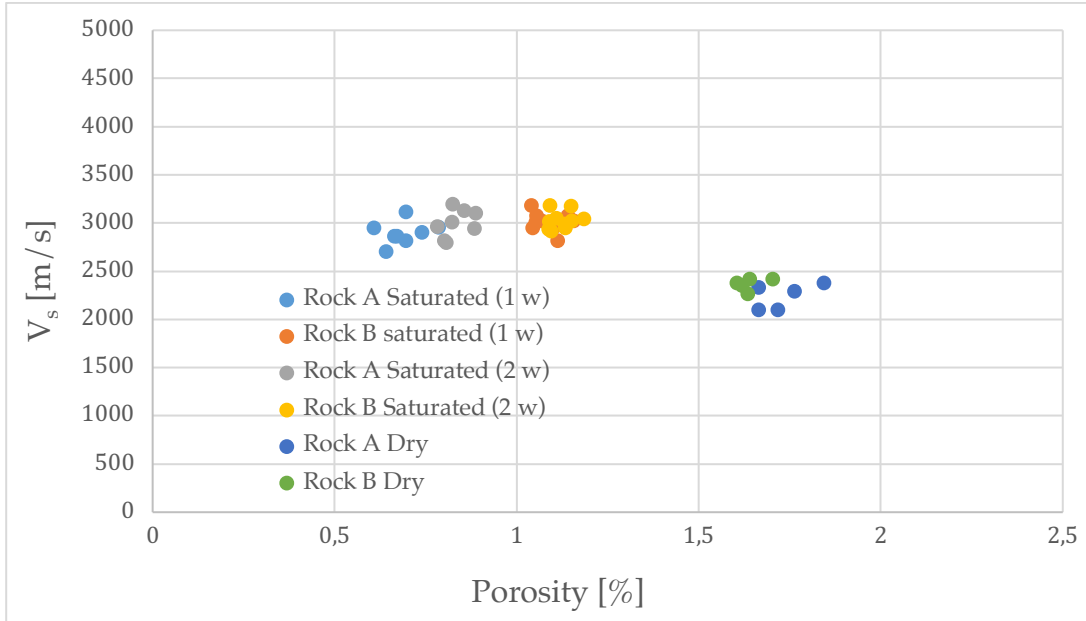


Figure 3.9: $(V_s - \text{porosity})$ plane comparison between saturated samples (1 week), saturated samples (2 weeks) and dry samples

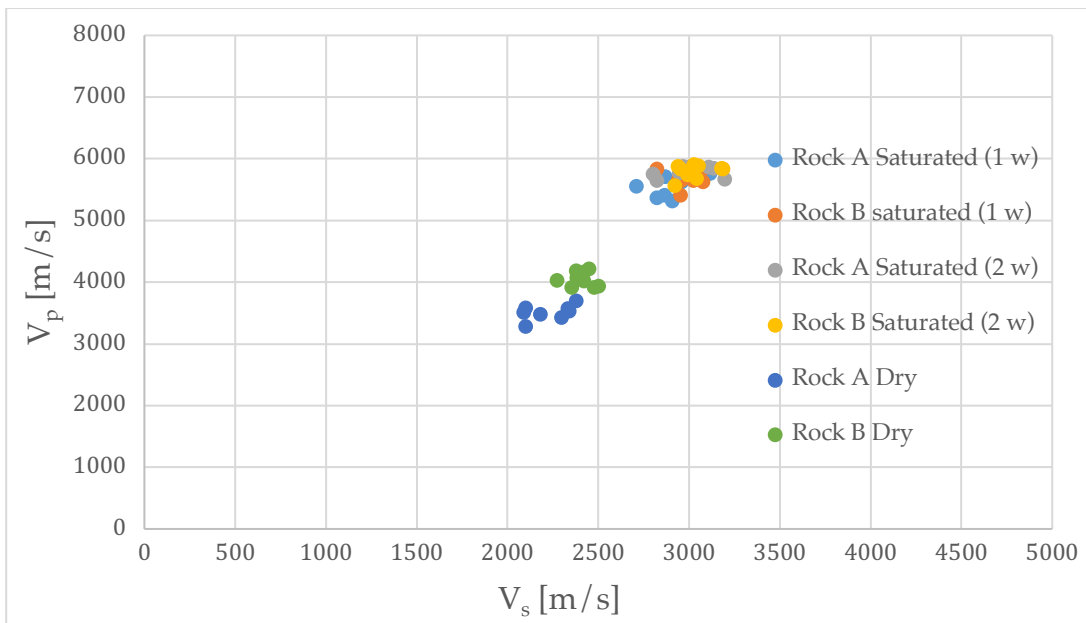


Figure 3.10: $(V_p - V_s)$ plane comparison between saturated samples (1 week), saturated samples (2 weeks) and dry samples

3.3.1 Seismic data comparison with literature and considerations

In the drained case, the measured propagation velocity is about 3500 – 4000 m/s for the P-waves, and 2200 – 2400 m/s for the S-waves. According to existing work [16][17], elastic properties in rocks are strongly affected by microcracks naturally present in the rock microstructure. Since P- and S-wave

velocities directly depend on the rock elastic constants, consequently they are also strongly effected by microcracks. In fact, the typical P- and S-wave velocities in literature are of about 6000 m/s and 3200 m/s in crack-free granites or granites when cracks are closed [19]. In the case study, the velocities of the P-waves and of the S-waves are lower than the theoretical speed in crack-free granite. In order to confirm this analysis, it is sufficient to observe the propagation velocity of the seismic waves in the saturated specimens. In fact, these speeds are equal to 5800 m/s for P-waves and 3000 m/s for S-waves, which are very close to those typical of an intact rock. This happens because the water present in the microcracks has a compressibility module much higher than the air, and when the high frequency seismic wave arrives, the water acts like a solid. This is the reason why we obtain values close to those of an intact rock, and therefore this implies the presence of microcracks within the analysed rock. Then, the next goal is to identify two parameters:

- Crack density ρ ;
- Aspect ratio ε (relation between the smallest and the biggest radius of the microcracks);

The first is the computation of the bulk modulus K , of the shear modulus G and of the Poisson's coefficient ν . The values of the two moduli have been evaluated in the dry case (K_{dry}, G_{dry}), saturated (K_{sat}, G_{sat}), and in the ideal case without microcracks (K_m, G_m) assuming a theoretical P- and S-wave velocities of 6000 m/s and 3200 m/s . The computation has been carried out with the relations reported by Adelinet [20]:

$$V_s = \sqrt{\frac{G_{dry}}{\rho}} \quad V_p = \sqrt{\frac{K + \frac{4}{3}G}{\rho}} \quad V_p = \sqrt{\frac{3K(1-\nu)}{(1+\nu)\rho}} \quad (3.12)$$

Therefore, a system of three unknowns and three equations can be solved identifying a rather high Poisson's coefficient equal to $\nu = 0.3$, that proves the presence of microcracks in the granite tested. The next step is the

determination of the crack density ρ solving one of the following two relationships:

$$\begin{cases} \frac{K_m}{K_{dry}} = 1 + \rho \frac{16}{9} \frac{1 - \nu_m^2}{1 - 2\nu_m} \\ \frac{G_m}{G_{dry}} = 1 + \rho \frac{32}{45} \frac{(5 - \nu_m)(1 - \nu_m)}{(2 - \nu_m)} \end{cases} \quad (3.13)$$

In the drained case, K_{dry} and G_{dry} are independent from the aspect ratio ε . Then, for a better evaluation of the crack density ρ an average was made between the two values identified. Finally, the following equation has been used to calculate the epsilon aspect ratio ε :

$$\frac{K_m}{K_{sat}} = 1 + \rho \frac{16}{9} \frac{1 - \nu_m^2}{1 - 2\nu_m} \left(\frac{\delta_{el}}{1 + \delta_{el}} \right) \quad (3.14)$$

where, $\alpha_{el} = K_f/K_m$ stands for the ratio of fluid-to-solid bulk moduli ($K_f = 2 \text{ GPa}$ for water), δ_{el} accounts for the fluid compressibility and the microcracks geometry characterized by the aspect ratio ε . In the case of an oblate spheroid:

$$\delta_{el} = \frac{\pi \varepsilon}{4} \frac{E_m}{1 - \nu_m^2} \left(\frac{1 - \alpha_{el}}{K_m \alpha_{el}} \right) \quad (3.15)$$

where, E_m is the Young's modulus of the host medium ($E_m = 40 \text{ GPa}$ from triaxial test carried out on the same rock).

The average aspect ratio ε is 0.05 and 0.049 respectively for the rock block A and B (Table 3.11). This means that the microcracks inside the samples are almost similar. On the contrary, a greater microcracks density ρ is found in the A-samples equal to 0.63%, while 0.38% in the B-samples, and this confirms the hypothesis done in the porosity analysis and explains why the P- and S-wave velocities are slightly lower in the A-rock than in the B-rock in dry conditions.

Table 3.11: Results of the microcracks aspect ratio and density investigation

Sample	ρ [kg/m ³]	G_{dry} [GPa]	G_{sat} [GPa]	G_m [GPa]	K_{dry} [GPa]	K_{sat} [GPa]	K_m [GPa]	ρ [%]	ϵ [–]
GA1	2609	13.8	25.2	25.1	12.4	56.0	60.5	0.68	0.074
GA2	2632	11.6	23.8	25.3	18.2	59.0	61.0	0.60	0.028
GA3	2603	14.2	22.6	25.0	14.3	56.6	60.3	0.58	0.053
GA4	2611	11.5	25.7	25.1	12.7	54.9	60.5	0.76	0.108
GA5	2588	14.6	22.8	24.9	15.9	58.8	60.0	0.51	0.014
GA6	2620	11.4	26.7	25.2	17.0	48.5	60.7	0.63	0.022
GA7	2634	12.5	21.0	25.3	15.1	55.9	61.1	0.64	0.080
GA8	2497	13.7	19.6	24.0	13.0	56.5	57.9	0.61	0.021
GB1	2607	15.3	24.1	25.1	21.8	51.9	60.4	0.38	0.086
GB2	2633	13.6	24.0	25.3	24.6	58.1	61.0	0.41	0.028
GB3	2612	14.8	23.9	25.1	25.9	59.2	60.6	0.35	0.011
GB4	2621	15.3	26.6	25.2	24.9	53.8	60.8	0.34	0.061
GB5	2615	14.5	26.4	25.1	20.8	54.1	60.6	0.42	0.070
GB6	2601	14.8	22.7	25.0	23.4	58.4	60.3	0.37	0.017
GB7	2611	14.9	23.4	25.1	23.9	54.7	60.5	0.37	0.053
GB8	2598	15.6	24.2	25.0	25.4	57.7	60.2	0.33	0.019
GB9	2648	16.6	22.6	25.4	19.0	51.9	61.4	0.41	0.102
GB10	2633	16.2	22.7	25.3	18.9	60.6	61.1	0.41	0.086

3.4 Triaxial test

One triaxial test was performed on an intact sample of “granite of Alzo” with the aim of detecting the residual friction angle φ_r . First, an isotropic compression (step 1) was applied until a pressure of 5 MPa with load control, and subsequently only the axial stress was increased until the specimen failure (step 2), while the confining pressure was kept constant. The second step was done in displacement control in order to analyse the post-peak phase. After the peak, when the residual strength value was achieved, the confining pressure value was increased up to 7 MPa. Then, the same procedure was

performed for the confining pressure values of: 10 MPa, 12 MPa, 15.15 MPa (Figure 3.11) The test parameters are the following:

- Diameter $D = 36.75 \text{ mm}$;
- Height $H = 75.80 \text{ mm}$;
- Cross-sectional surface $S = 1060.73 \text{ mm}^2$;
- Hydrostatic load velocity (step 1) = $35 \text{ N/s} = 20 \text{ MPa/min}$;
- Axial displacement velocity (step 2) = 0.000758 mm/s ;

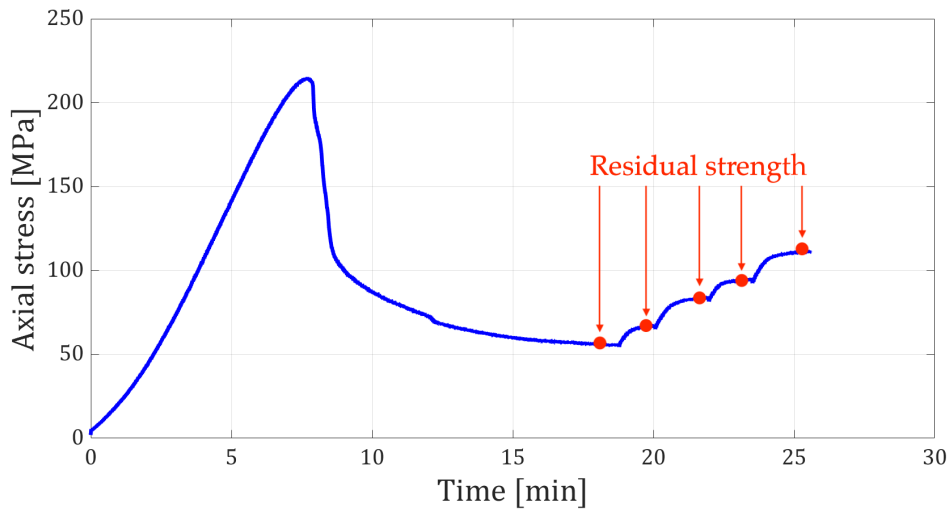


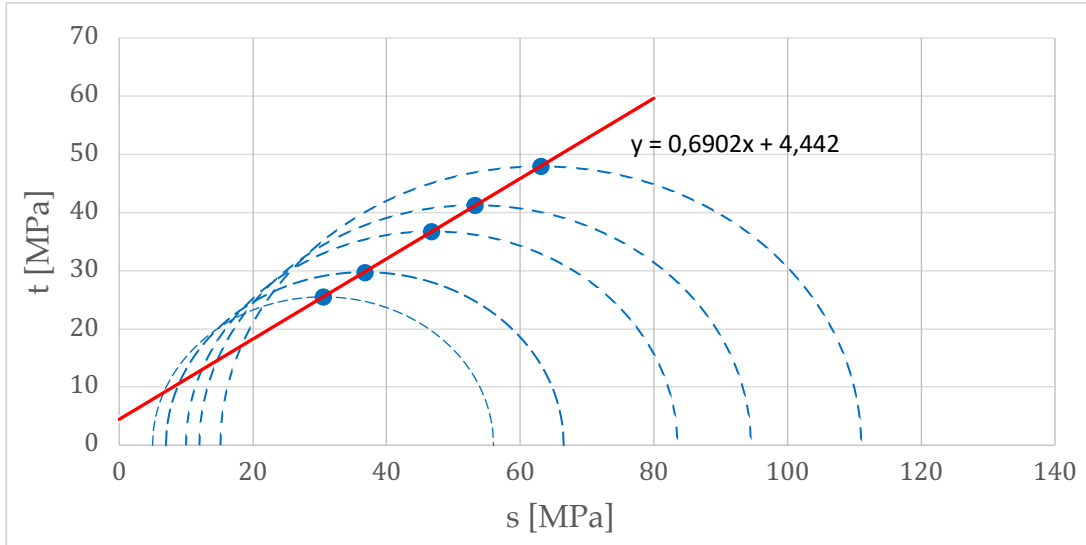
Figure 3.11: Triaxial test result

During the residual phase, an axial stress value σ_a can be identified for each confining pressure σ_r (Table 3.12). Then, the stress state have been plotted in $(t - s)$ deviatoric plane (Figure 3.12).

$$t = \frac{\sigma_a - \sigma_r}{2} \qquad s = \frac{\sigma_a + \sigma_r}{2} \qquad (3.16)$$

Table 3.12: Residual phase stress condition

σ_r [MPa]	σ_a [MPa]
5	56
7	66.5
10	83.5
12	94.5
15.15	111

Figure 3.12: $(t - s)$ deviatoric plane

Finally, the residual friction angle φ_r and the cohesion c (Table 3.13) can be obtained with the following relationship from the equation of the fitting function:

$$\varphi_r = \arcsen(\tan\alpha) \quad c = a/\cos\varphi_r \quad (3.17)$$

where a is the value of the y-axis intercepts, and α is the slope of the line.

Table 3.13: Residual friction angle φ_r and the cohesion c of the rock

$(t - s)$ deviatoric plane		Rock's parameters	
a	$\tan\alpha$	φ_r [°]	c [MPa]
5	56	43	6

3.5 Concluding remarks

The preliminary analyses led to the conclusion that there is a little difference between the two rock blocks, but the variation of the analysed parameters are so small that it is reasonable to think that the two rock blocks could have the same mechanical behaviour. For this reason, the mechanical characterization were carried out initially on the rock of block B, but subsequently also the rock block A has been used, after having checked a pretty similar response for both

rocks. For this reason, the samples are named only with the letter G and a number from this point forward. Furthermore, from the triaxial test it is possible to identify the friction angle friction and cohesion of the granite that could have been used in the LEM analysis. Since the analysed rock is intact, the mechanical parameters are very high and consequently, with a conservative approach, it has been chosen to keep using the assumption done in the chapter 1.



Figure 3.13: Photo of the specimen after the triaxial test

Chapter 4

Fracture toughness investigation

In this chapter, the fracture toughness of the granite of Alzo is investigated. In particular, thermally cracked disc specimens have been tested on the mode I fracture toughness response to an increasing, to a constant and to cyclic loading, in order to compare the different responses and to compute the sub-critical crack growth parameters in different cases. Finally, the mode II fracture toughness has been investigated. All the tests were carried out on Cracked Chevron Notched Brazilian Disc (CCNBD) rock specimens. Summing up, the main features of these four types of tests are:

- First type of test with increasing load until the failure in order to analyse the mode I fracture toughness as a function of the degree of internal damage due to the different temperature of thermal treatment;
- Second type of test with constant load lower than the SUL (obtained in the first test) in order to analyse the creep behaviour of the material as a function of the applied load, keeping a constant thermal treatment and internal damage;
- Third type of test with cyclic load in order to investigate the fatigue behaviour of the granite of Alzo as a function of the applied load, keeping a constant thermal treatment and internal damage and comparing the results with the creep ones;
- Fourth type of test with increasing load until the failure in order to analyse the mode II fracture toughness response.

4.1 Sample preparation

As discussed in the section 2.3, the Cracked Chevron Notched Brazilian Disc (CCNBD) specimen has been chosen to carry out the fracture toughness investigation.

4.1.1 Cutting phase

Therefore, cylindrical samples with a thickness of 30 mm and a diameter of 80 mm were obtained from the original rock block. Subsequently, the chevron notch was made with a circular diamond saw with a diameter of 50 mm . Two cuts from both sides of the disc and a special designed jig recommended by the ISRM [21] was used to ensure that the chevron notched were exactly in the centre of the disc (Figure 4.1).

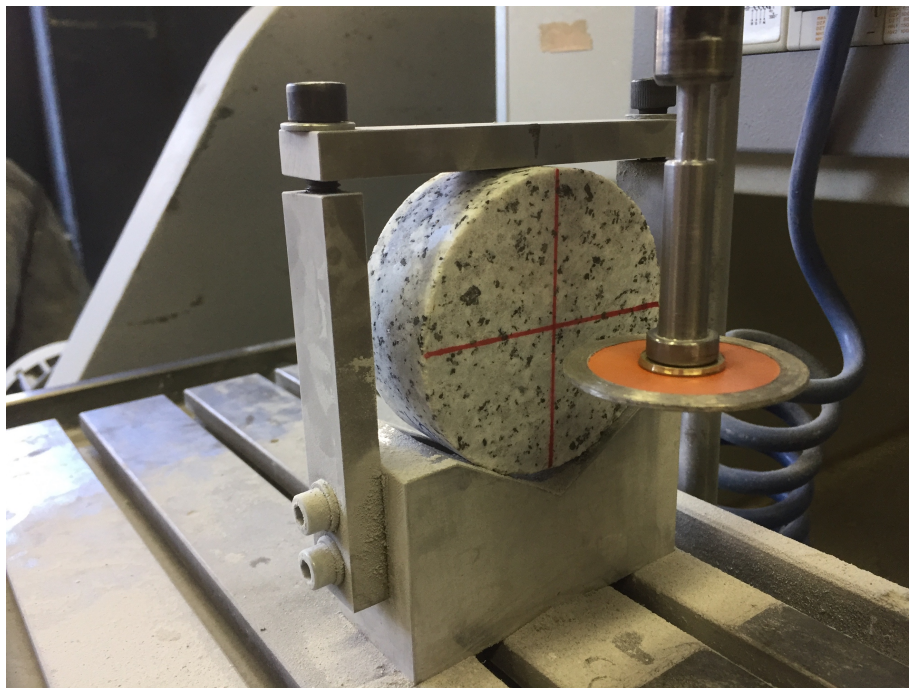


Figure 4.1: Special jig recommended by the ISRM with the circular diamond saw

4.1.2 Thermal treatment

After cutting the sample, a thermal treatment was performed by increasing the temperature with a rate of $1\text{ }^{\circ}\text{C}/\text{min}$ until the attainment of the target temperature, in order to avoid an excessive difference between the outside and the inside of the sample. Once the desired temperature has been reached,

it has been kept constant for one hour, and finally the sample has been left to cool down inside the off oven (Figure 4.2). The thermal treatment purpose is to emulate the degradation that the rock can may undergo in situ. Indeed, the two rock blocks analysed before are pretty intact, while it is reasonable to think that the in situ rock formation is degraded in particular along the discontinuities. The temperature variation caused microcracks in rock because the mineralogical components have a different thermal expansion coefficients. For the first type of test, with increasing load until the failure, the specimens has been tested in absence of thermal treatment, and also with a thermal treatment of 100°C , 200°C , 300°C , and 400°C , in order to analyse the decreasing mode I fracture toughness in function of the increasing thermal damage. The thermal treatment was stopped before to reach 500°C , close to the temperature of α/β phase transition in quartz. All the other tests have been carried out with a fixed thermal damage, in order to represent the unfavourable weathered conditions of the rock mass on site, and it has been chosen an average degree of internal damage corresponding to a 200°C thermal treatment.



Figure 4.2: CCNBD sample into the oven ready for the thermal treatment

4.1.3 Sensors positioning

Two radial and two axial strain gauges were positioned close to the crack tips in order to investigate the local deformation and to determine where the first crack propagation occurred. The crack mouth opening displacement (CMOD) was measured, instead, by an extensometer placed on two metal plates glued across the notch. The CMOD data are fundamental in order to determinate the exact time of the specimen's failure and also the subcritical crack growth parameters. Only for the mode II fracture toughness investigation the CMOD and the strain gauges were not placed on the sample because only the force applied was needed.

4.1.4 Acoustic emission's sensors

Only for the second type of test with constant load lower than the SUL in order to analyse the creep behaviour of the rock, twelve piezoelectric transducers have been positioned on the samples, four of them radially, four on the upper face and four on the lower face (Figure 4.3). The aim of these sensors it to detect the evolution of acoustic emissions during the test, indeed, they are elastic waves generated during the crack propagation.

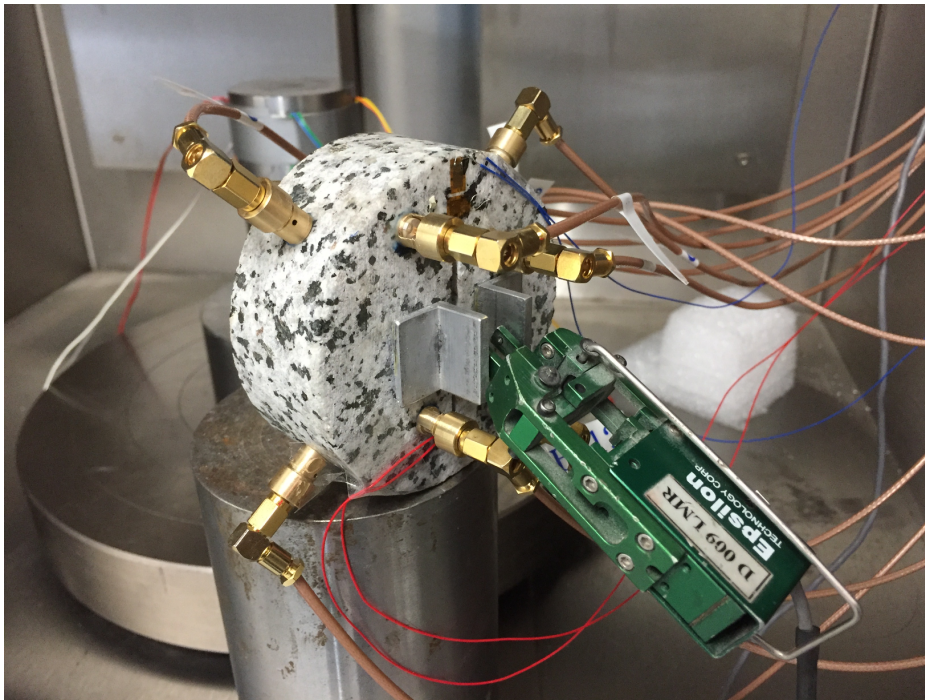


Figure 4.3: CCNBD specimen with all the sensors placed on it (AE sensors, strain gauges and extensometer) and ready for the test

4.1.5 CCNBD geometry

According to the ISRM suggestions [21], all the dimensions of the CCNBD specimen geometry (Figure 4.4) should be converted into dimensionless parameters with respect the radius R and diameter D .

$$\begin{cases} \alpha_0 = a_0/R \\ \alpha_1 = a_1/R \\ \alpha_B = B/R \\ \alpha_s = D_s/D \\ \alpha_m = a_m/R \end{cases} \quad (4.1)$$

where D is the diameter, B is the thickness, a_0 is the initial chevron-notched crack length, a_1 is the final chevron-notched crack length, a_m is the critical crack length, and finally D_s is the saw's diameter.

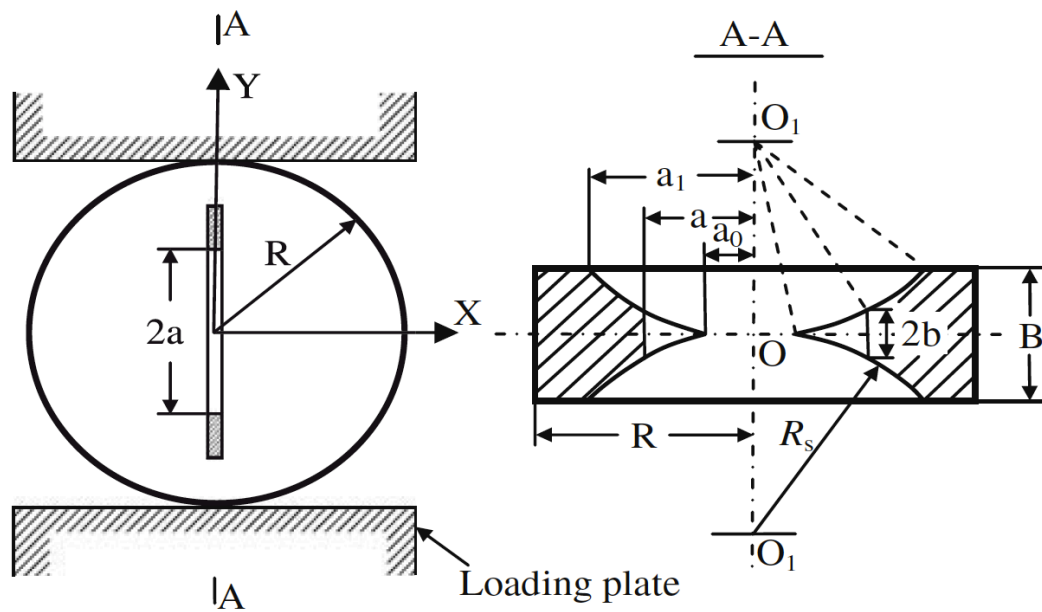


Figure 4.4: CCNBD specimen's geometry [15]

However, due to the plane strain constraint, not all geometries of the CCNBD are valid to be used for fracture testing. Studies [13] [14] showed that CCNBD geometries must fall within a particular range in order to yield valid fracture toughness results. These ranges can also be expressed below:

$$\begin{cases} \alpha_1 \geq 0,4 \\ \alpha_1 \geq a_B/2 \\ \alpha_B \leq 1,04 \\ \alpha_1 \leq 0,8 \\ \alpha_B \geq 1,1729 \cdot \alpha_1^{1,6666} \\ \alpha_B \geq 0,44 \end{cases} \quad (4.2)$$

Surveys proved that the CCNBD specimens within the outlined range will generate valid fracture toughness values, which are consistent with the results obtained by reference tests with the ISRM suggested CB and SR methods. The fracture toughness values obtained from the specimens with geometries far outside the range vary considerably. Therefore, in order to have a valid fracture toughness test, the valid geometry requirements should be strictly observed. The initial crack length a_0 for specimen preparation could be set between $(0,2 - 0,3)R$. Surveys show that, in order to have a valid test, the CCNBD specimen diameter D is recommended to be at least 75 mm unless a smaller size has been validated beforehand, furthermore, the diameter D should be related to the size of the largest grain in the rock by the ration of at least 10:1. After the test, the geometrical dimension $2a_0$ should be measured from the broken sample and the result should be considered invalid if the crack deviates from symmetrical crack plane more than $0,05D$. The Table 4.1 contains the geometrical data of the samples used in the tests, while in the Figure 4.5 the validity of the chosen geometry is respected.

Table 4.1: Summary of geometrical data

Sample	Test	Thermal treatment	B [mm]	D [mm]	$2a_1$ [mm]	$2a_0$ [mm]
G1	Mode II	200° C	29.66	79.60	49.45	20.0
G2	Mode II	200° C	30.01	79.55	49.24	23.0
G4	Mode I	400° C	30.65	79.57	49.42	22.0
G9	Mode I	300° C	30.64	79.56	48.37	16.0
G6	Mode I	200° C	30.44	79.57	48.96	19.0
G7	Mode I	100° C	30.87	79.64	48.79	17.0
G8	Mode I	none	30.78	79.58	48.18	16.0
G10	Mode I (creep)	200° C	30.57	79.52	48.48	17.0
G12	Mode I (creep)	200° C	30.49	79.55	48.65	19.0
G16	Mode I (creep)	200° C	31.07	79.49	48.75	19.0
G18	Mode I (creep)	200° C	27.33	79.72	49.38	26.0
G17	Mode I (cyclic)	200° C	30.68	79.52	48.68	19.0
G24	Mode I (cyclic)	200° C	30.12	79.50	48.94	21.0
G36	Mode I (cyclic)	200° C	30.10	79.62	48.58	23.0

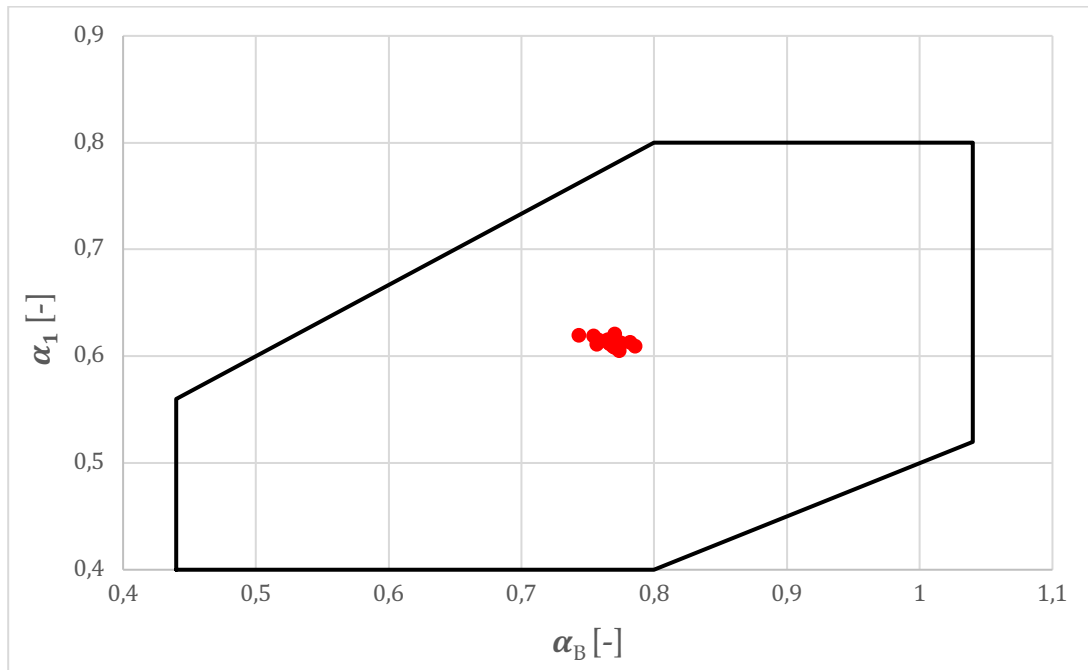


Figure 4.5: ISRM suggested valid geometry for CCNBD specimen's valid geometry

4.2 Mode I fracture toughness investigation

The CCNBD specimen is subjected to pure mode I failure when the angle φ between the crack line and the loading direction is zero. According to ISRM suggestions [21], mode I fracture toughness for the CCNBD specimen can be evaluated as:

$$K_{IC} = \frac{P_{max}}{B\sqrt{R}} Y_{min}^* \quad (4.3)$$

where P_{max} is the maximum load at the failure, R is the radius of the disc, B is the disc's thickness, and Y_{min}^* is a critical non-dimensional stress intensity factor, which depends on the dimensionless parameters α_0 , α_1 and α_B , and calculated as:

$$Y_{min}^* = f(\alpha_0, \alpha_1, \alpha_B) = ue^{v\alpha_1} \quad (4.4)$$

where u and v are the constants given by the ISRM recommendation [21] in terms of on α_0 and α_B .

4.2.1 Mode I fracture toughness with increasing load until failure

CCNBD samples were axially loaded with a crack inclination angle of zero ($\varphi = 0^\circ$) to provide a pure mode I loading condition. The tests were carried with displacement control until failure and with a displacement rate of 0.01 mm/s . Five specimens with different internal damage were analysed following the ISRM instruction [21] and the final aim is to investigate the variation of the mode I fracture toughness in function of the internal damage of the rock. The axial load, the axial displacement, the crack mouth opening displacement (CMOD), and the radial and axial strain closer the two crack tips were continually recorded during the test with an acquisition frequency of 200 Hz . Finally the acoustic emission recording were performed with a frequency of 10 MHz in a continuous way.

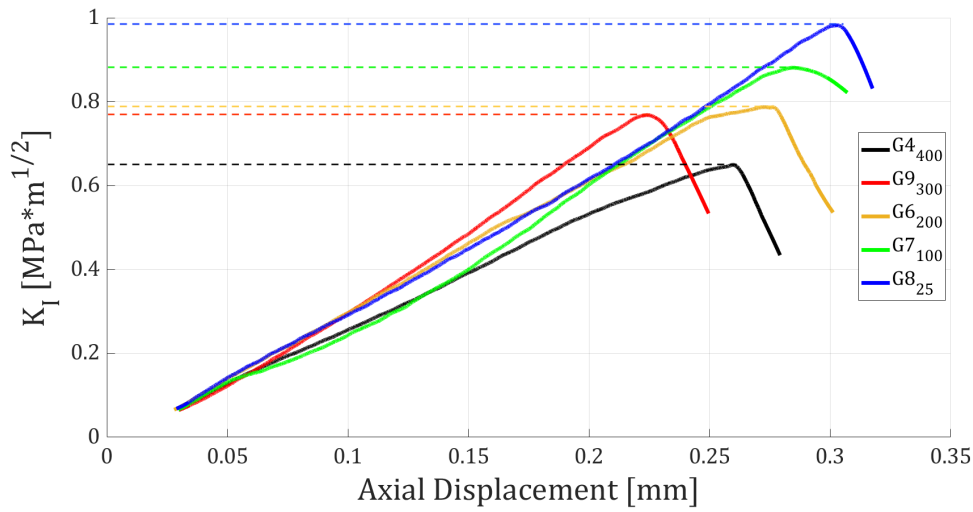


Figure 4.6: Stress intensity factor in function of the axial displacement for each samples during the mode I fracture toughness tests (increasing load)

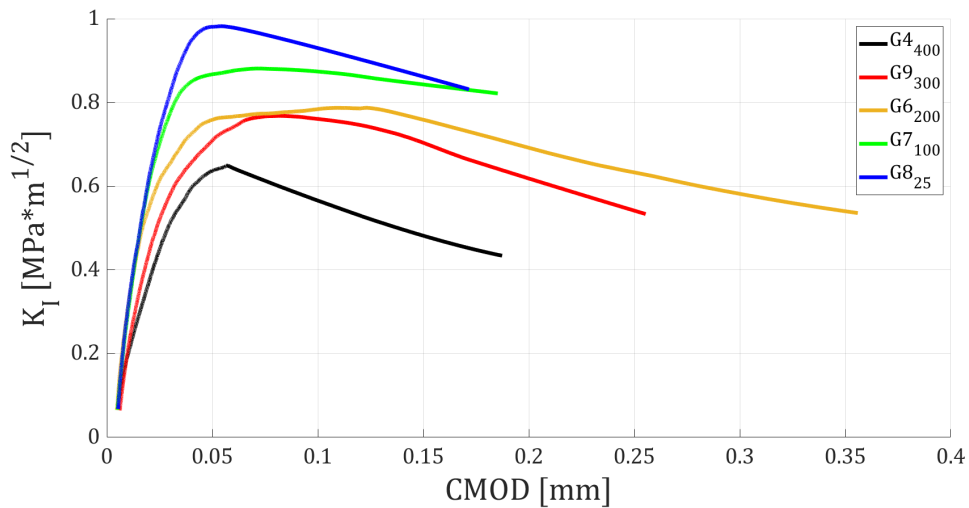
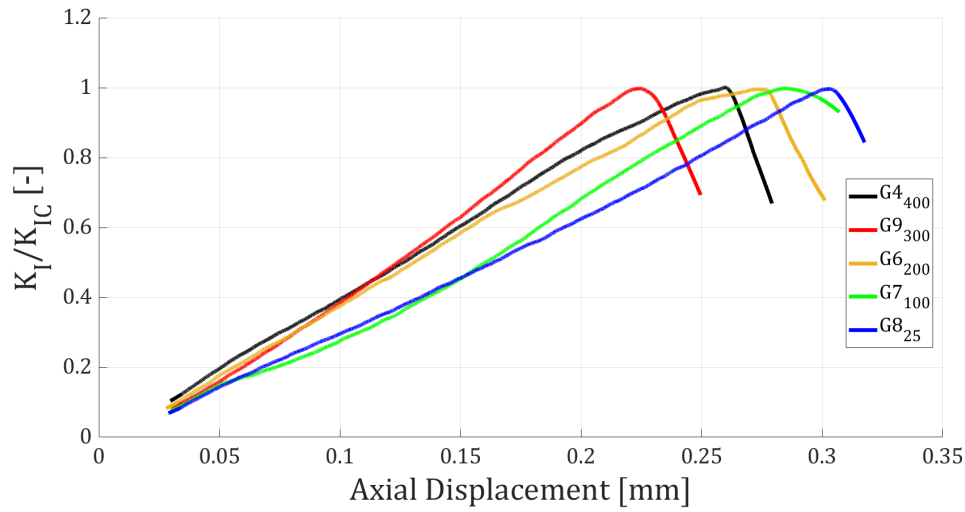
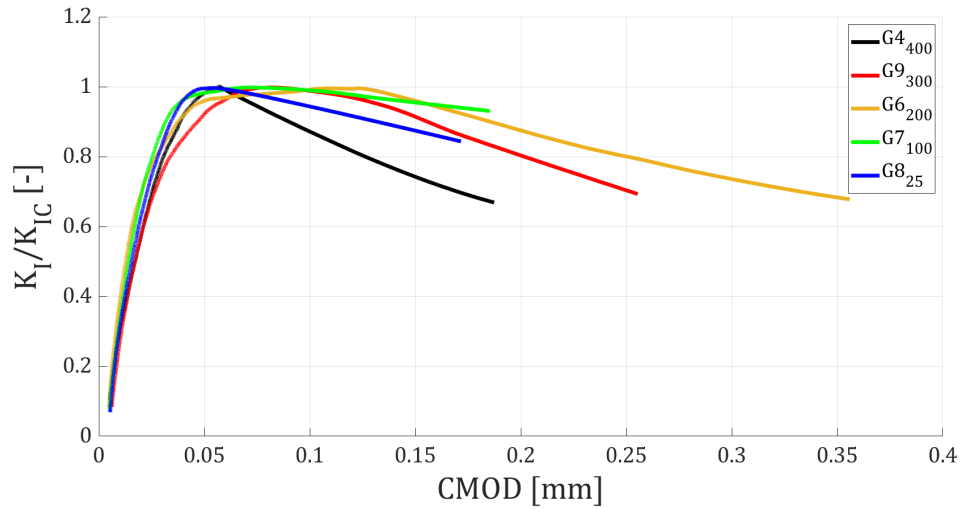
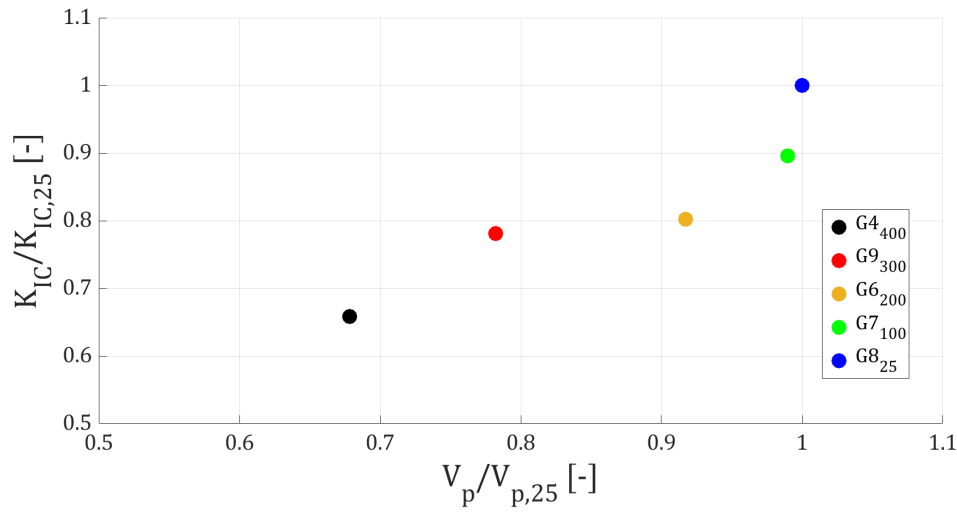
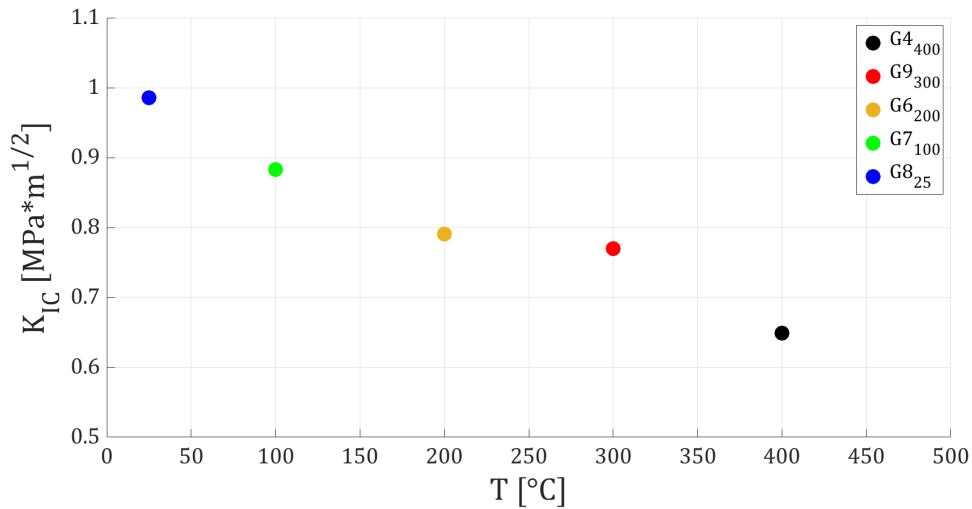


Figure 4.7: Stress intensity factor in function of the CMOD for each samples during the mode I fracture toughness tests (increasing load)

In the Figures 4.6 and 4.7, it is plotted respectively the axial displacement and CMOD in function of the increasing stress intensity factor K_I for each sample thermally cracked. The highest point of each curve represents the mode I fracture toughness K_{IC} of a specific thermal treated specimen. Then, from these first two graphs, it is possible to appreciate the reduction of the mode I fracture toughness due to the increase of internal damage, and also how the failure occurs for similar values of Crack Mouth Opening Displacement CMOD.

Figure 4.8: K_I/K_{IC} in function of the axial displacement (increasing load tests)Figure 4.9: K_I/K_{IC} in function of the CMOD (increasing load tests)

Finally, in the Figures 4.8 and 4.9, the ratio K_I/K_{IC} is plotted in function respectively of the axial displacement and CMOD for each thermally treated sample. This helps to investigate any difference in the ultimate axial displacement and in the ultimate CMOD, which is almost identical in all the specimens at the failure.

Figure 4.10: $K_I/K_{IC,25}$ in function of $V_p/V_{p,25}$ Figure 4.11: $K_I/K_{IC,25}$ in function of the temperature of the thermal treatment

In the Figure 4.10, the ratio between the fracture toughness of the thermal treated sample K_{IC} and the intact one $K_{IC,25}$ is provided as a function of the ratio between the P-waves velocity of the thermal treated sample V_p and the intact one $V_{p,25}$. In the Figure 4.11, instead, it is shown the decrease of the fracture toughness in relation to the temperature of the thermal treatment.

All the main data related to the mode I fracture toughness test with increasing load are summarized in the Table 4.2. Furthermore, the K_{IC} values obtained seem to be consistent because they are very similar to the results of past studies [19][22][23][24][25][26].

Table 4.2: Summary of the mode I fracture toughness investigation

Sample	Thermal treatment	P_{max} [kN]	K_{IC} [$MPa\sqrt{m}$]	$K_{IC}/K_{IC,25}$ [%]	V_p [m/s]
G4	400° C	4.93	0.65	65.6	2712
G9	300° C	6.13	0.77	77.7	3127
G6	200° C	6.09	0.79	79.8	3667
G7	100° C	7.01	0.88	88.9	3882
G8	none	7.93	0.99	100	3998

In the following figures (4.12 → 4.26), the number of acoustic emissions per second is plotted in function of the stress intensity factor K_I and of the CMOD. It is possible to notice how the number of microcracks increases exponentially close to the failure point, and then it decreases progressively after the breakage. Furthermore, it is evident that the amount of recorded events tends to be lower for the most damaged samples with the thermal treatment. In fact, in the damaged samples there is already a high number of microcracks, which favours the rupture of the sample. Then, it is reasonable to expect that the energy generated by the microcracks is also lower for the damaged samples. The number of acoustic events has been calculated by analysing the acoustic emission signals filtered with a high threshold value of the energy. Thus, the amount of events in the plots is related to quite big crack propagation in the rock formation. This choice was necessary in order to avoid the saturation of the signal nevertheless all the unfiltered signals will be used in the energetic dissipation analysis.

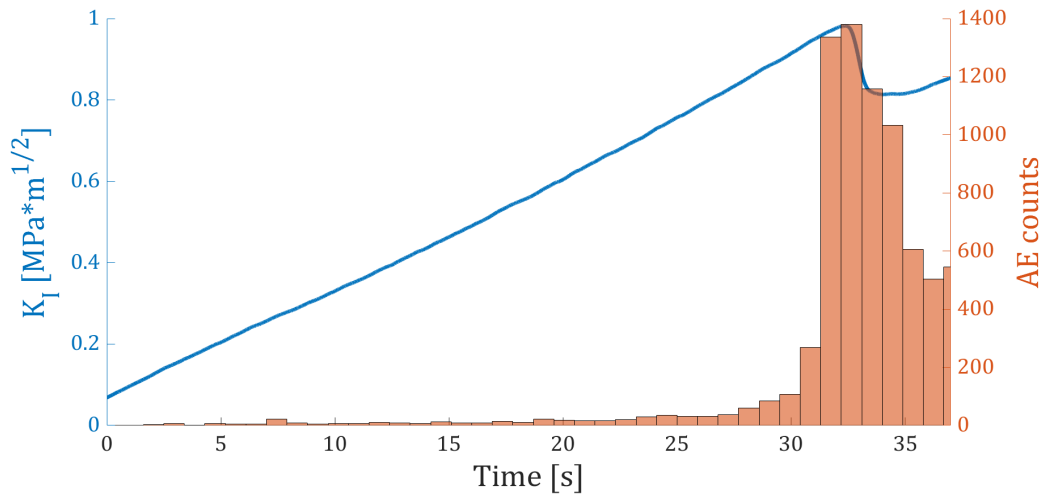


Figure 4.12: Stress intensity factor evolution coupled with AE of test G8 (no treated)

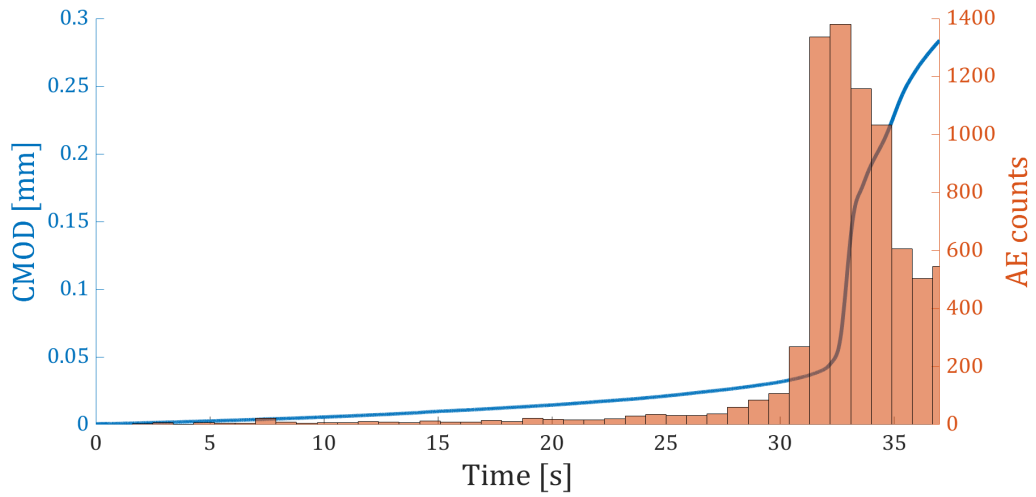


Figure 4.13: CMOD evolution coupled with AE of test G8 (no treated)

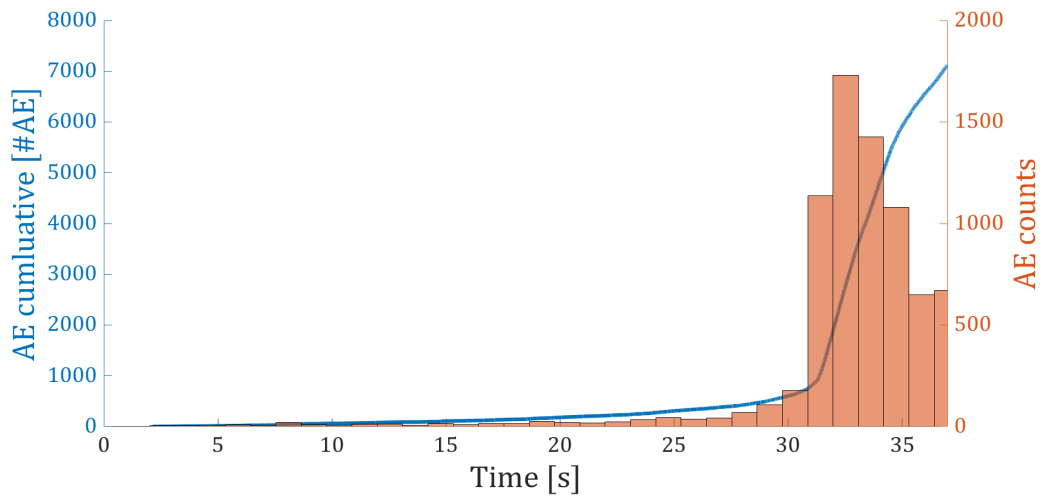


Figure 4.14: Acoustic emission cumulative evolution of test G8 (no treated)

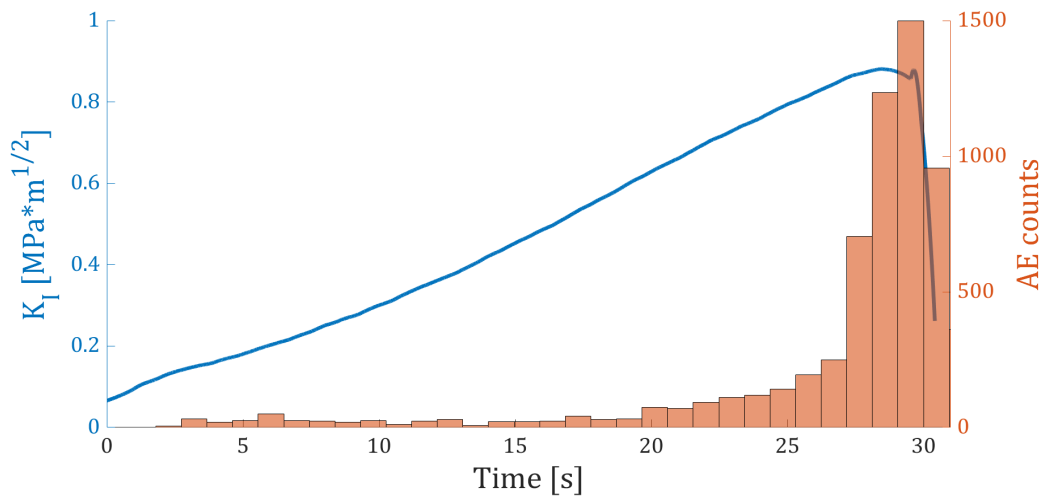


Figure 4.15: Stress intensity factor evolution coupled with AE of test G7 (100° C)

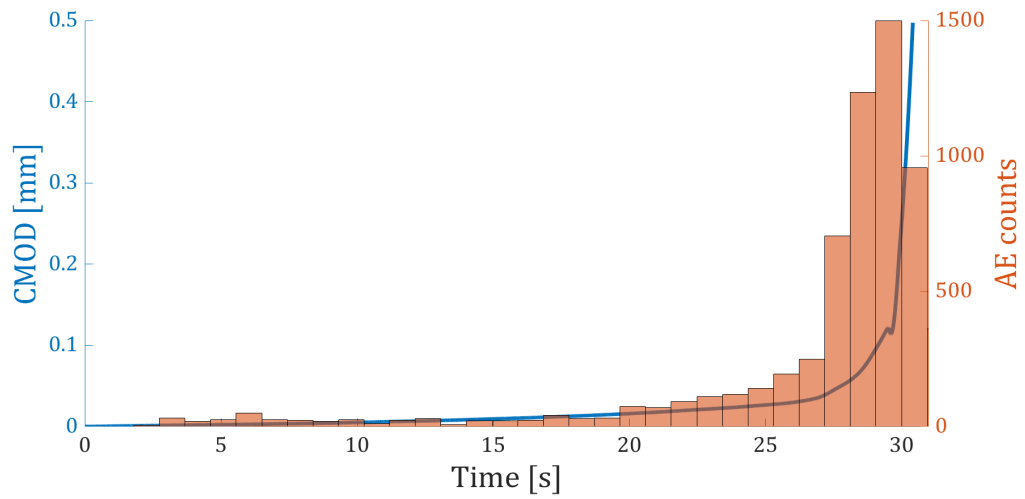


Figure 4.16: CMOD evolution coupled with AE of test G7 (100° C)

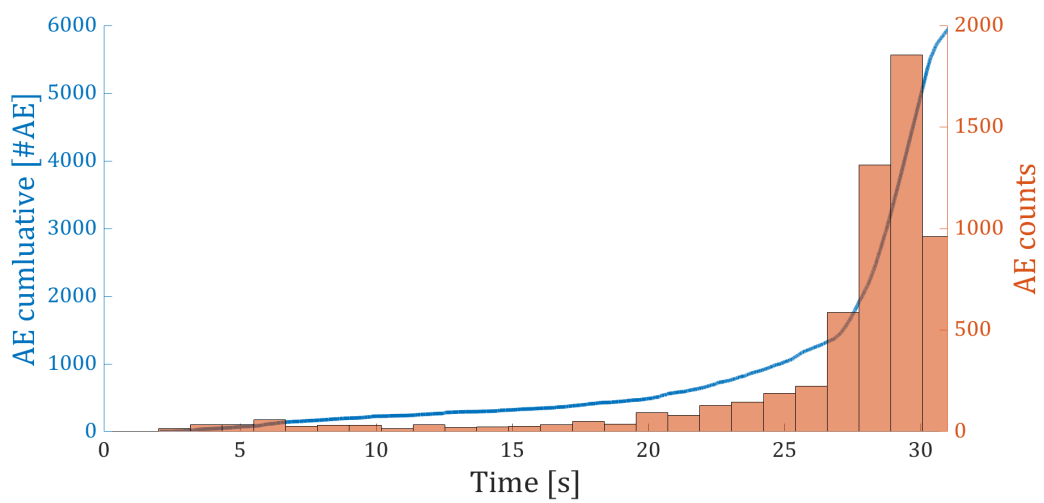


Figure 4.17: Acoustic emission cumulative evolution of test G7 (100° C)

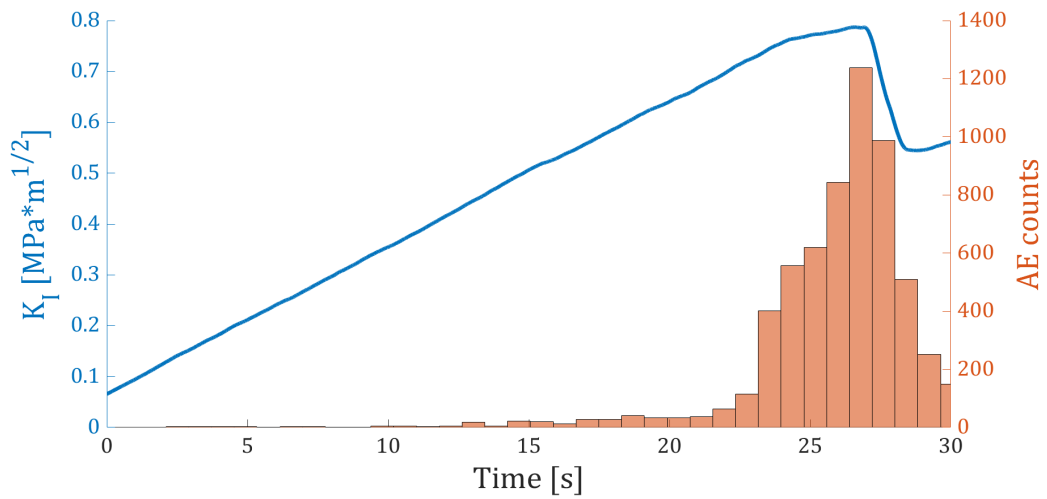


Figure 4.18: Stress intensity factor evolution coupled with AE of test G6 (200° C)

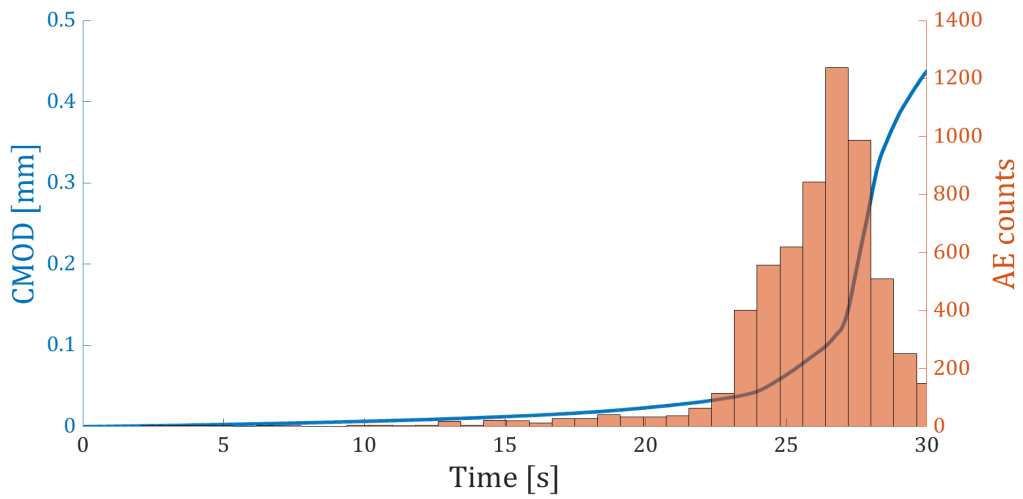


Figure 4.19: CMOD evolution coupled with AE of test G6 (200° C)

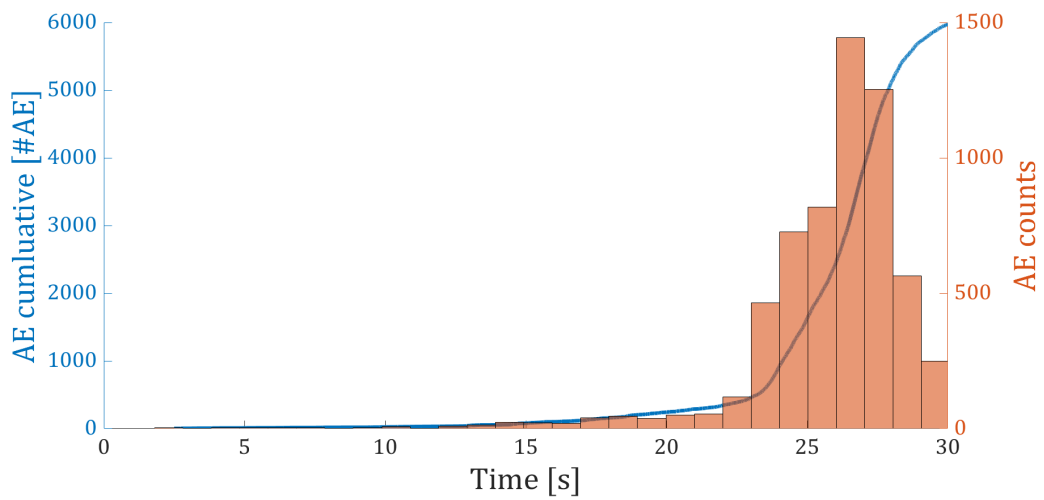


Figure 4.20: Acoustic emission cumulative evolution of test G6 (200° C)

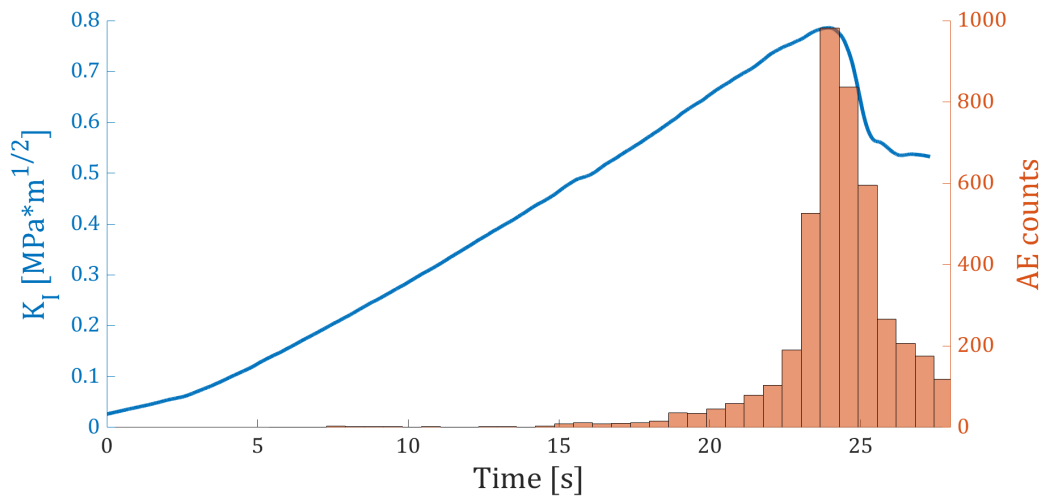


Figure 4.21: Stress intensity factor evolution coupled with AE of test G9 (300° C)

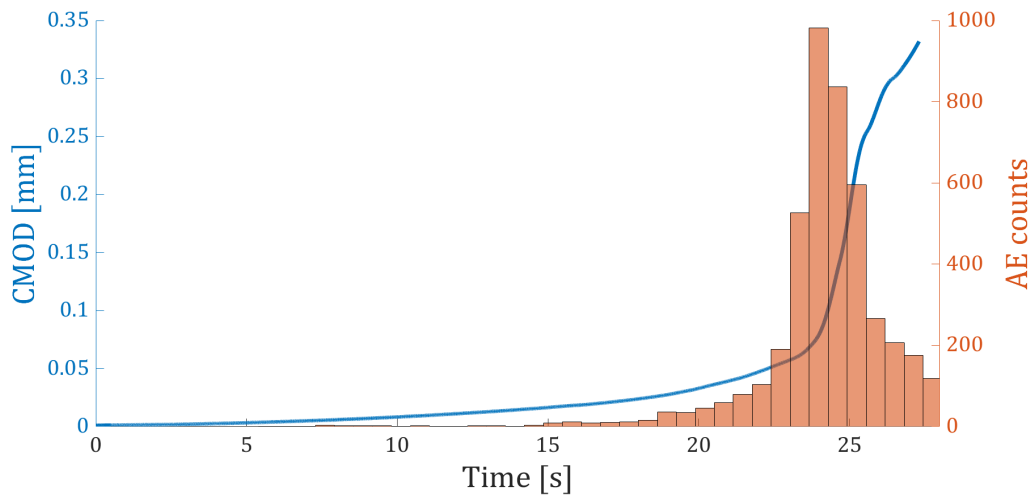


Figure 4.22: CMOD evolution coupled with AE of test G9 (300° C)

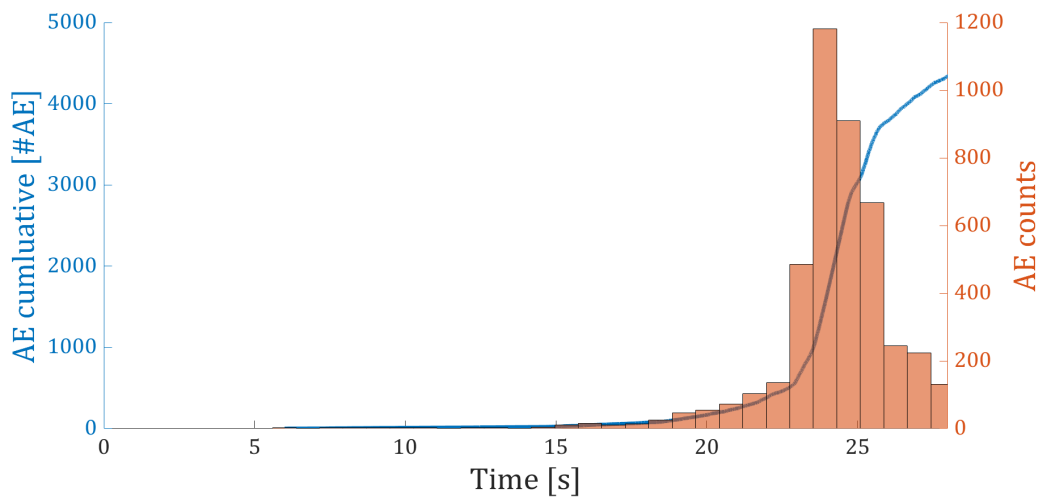


Figure 4.23: Acoustic emission cumulative evolution of test G9 (300° C)

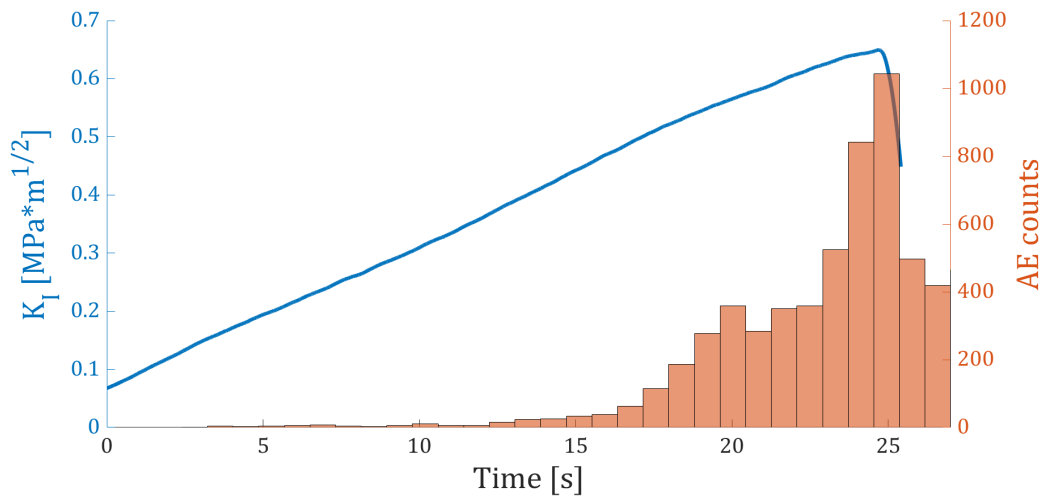


Figure 4.24: Stress intensity factor evolution coupled with AE of test G4 (400° C)

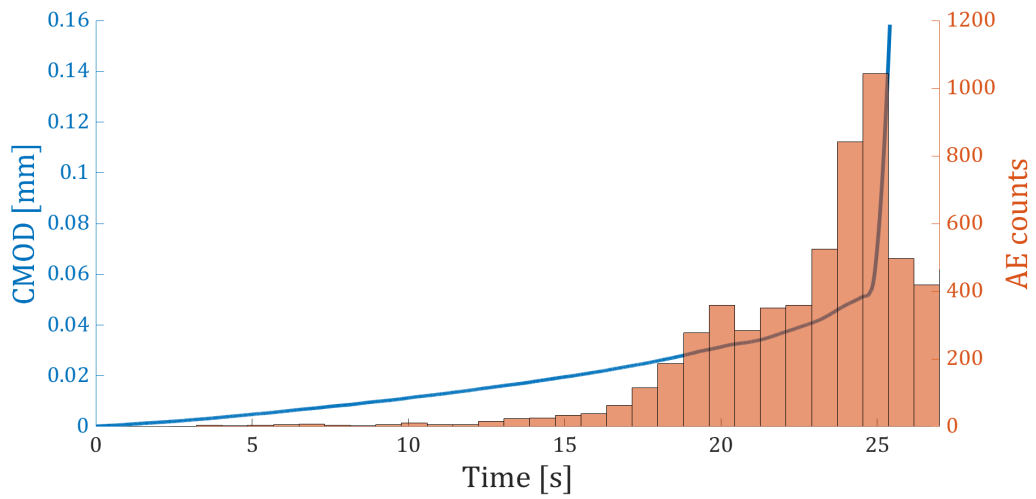


Figure 4.25: CMOD evolution coupled with AE of test G4 (400° C)

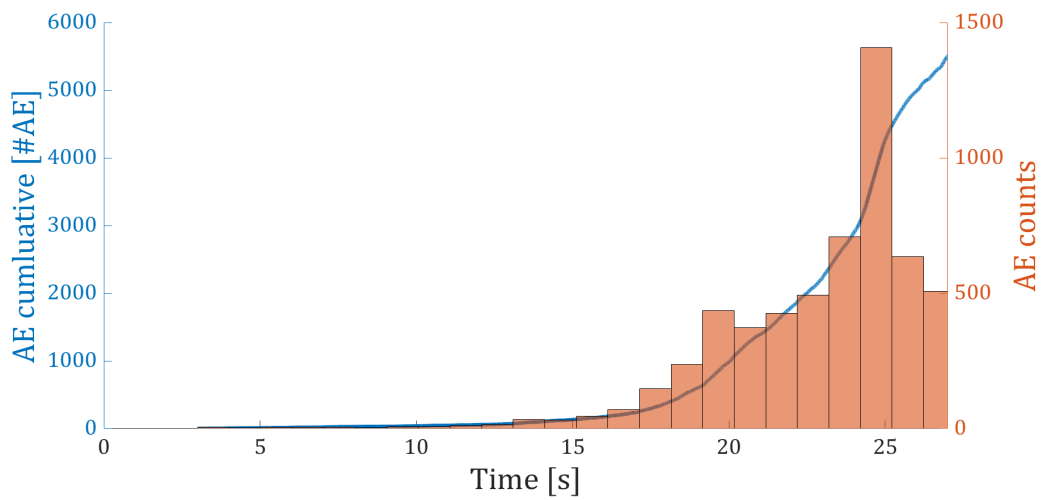


Figure 4.26: Acoustic emission cumulative evolution of test G4 (400° C)

In the following figures (4.27 → 4.31), it is possible to appreciate the samples before and after the mode I failure. The fracture propagations are linear according to ISRM standards for all the samples. Furthermore, we can see a greater tendency to linear propagation of the fracture in the samples thermally treated at higher temperatures. Finally, the Figure 4.32 shows the sample G8 while the test was running and just after the crack propagation .

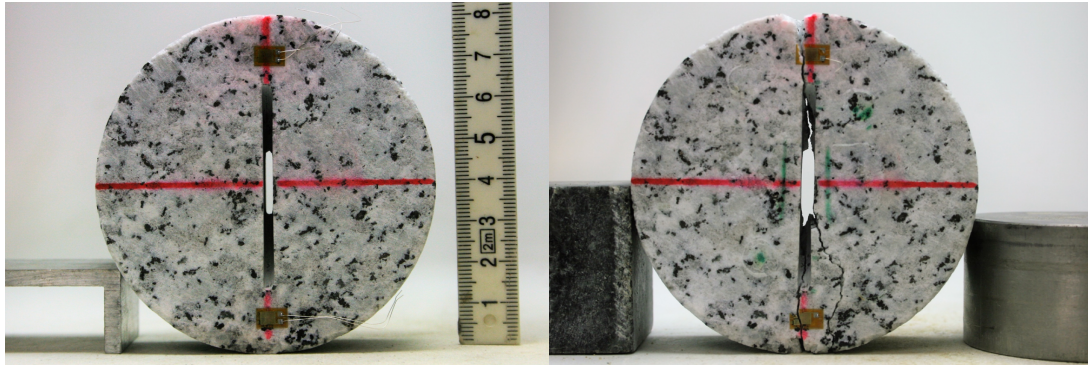


Figure 4.27: Picture of G8 sample (no thermally treated) before and after the test

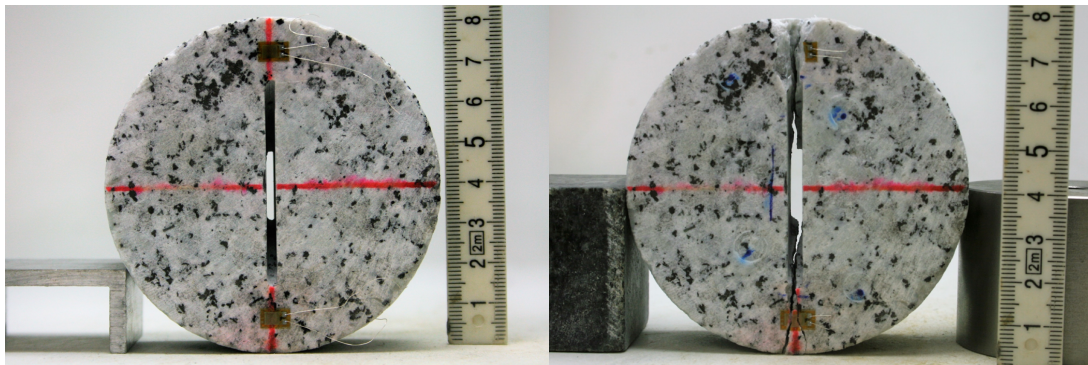


Figure 4.28: Picture of G7 sample (100° C) before and after the test

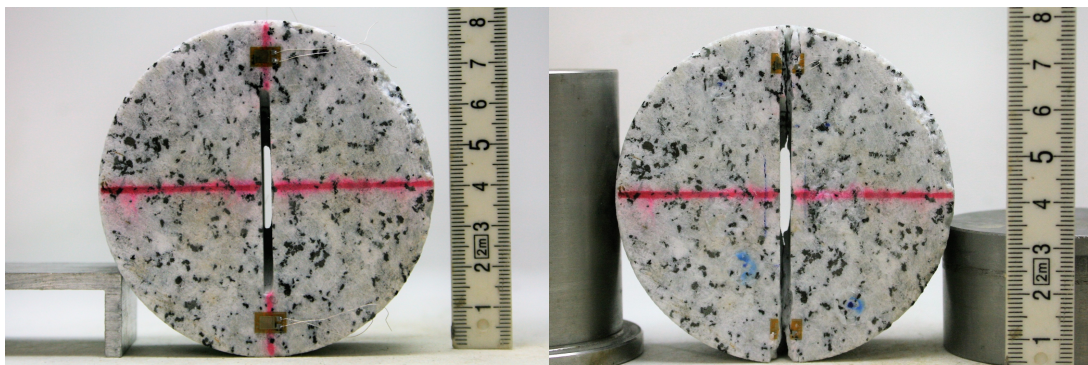


Figure 4.29: Picture of G6 sample (200° C) before and after the test

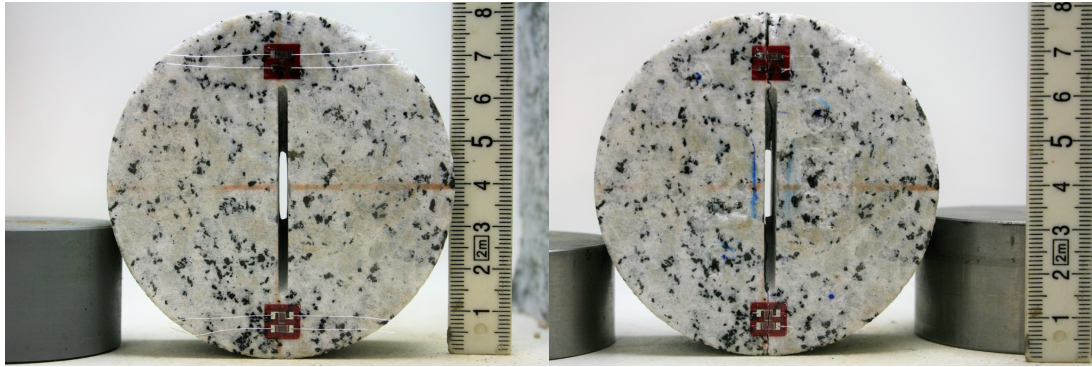


Figure 4.30: Picture of G9 sample (300° C) before and after the test



Figure 4.31: Picture of G4 sample (400° C) before and after the test

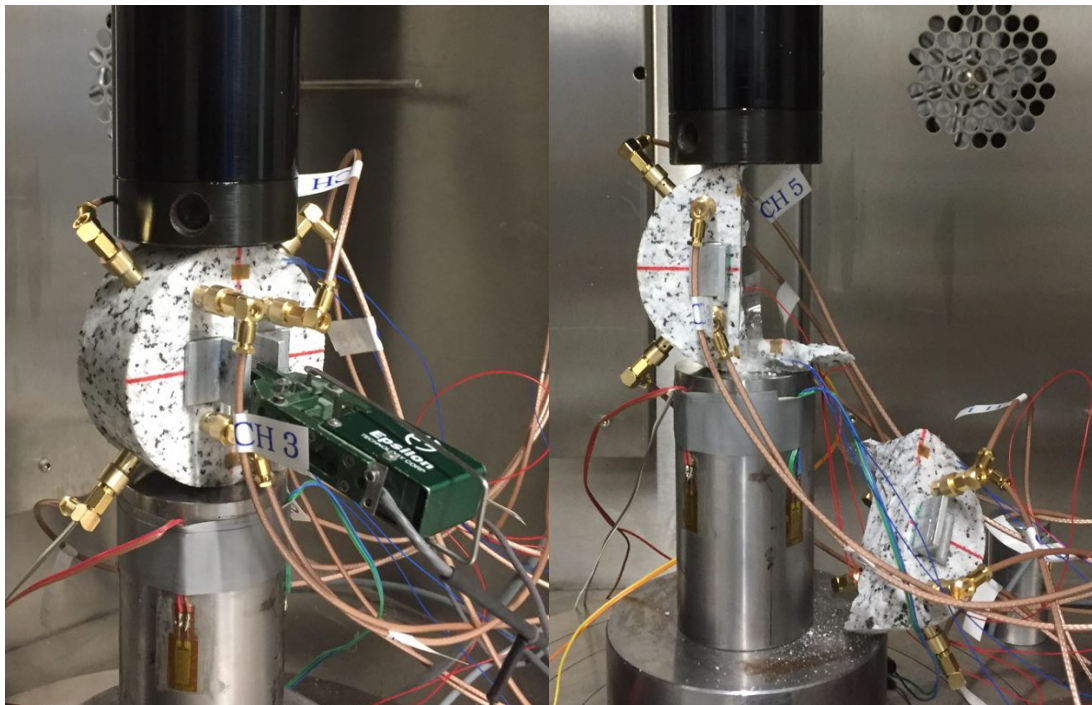


Figure 4.32: G8 sample during the test and just after the crack propagation

4.2.2 Mode I fracture toughness with constant load (creep)

CCNBD samples were axially loaded with a crack inclination angle of zero ($\varphi = 0^\circ$) to provide a pure mode I loading condition. Four tests were carried out on $200^\circ C$ thermally treated samples in order to investigate the behaviour in relation to different values of load. It has been decided to analyse a thermally damaged sample, instead of an intact one, in order to identify the subcritical crack growth parameters representative of the rock in situ, in fact it is plausible to assume that there is degradation of the rock, especially along the discontinuity. The specimens were initially loaded until the “target load” in such a way to reach it in one minute (loading control), and then the loading was kept constant until failure (Figure 4.33). The axial load, the axial displacement, the crack mouth opening displacement (CMOD), and the radial and axial strain closer the two crack tips were continually recorded during the test with an acquisition frequency of 200 Hz. Finally the acoustic emission recording were performed with a frequency of 10 MHz in a passive way.

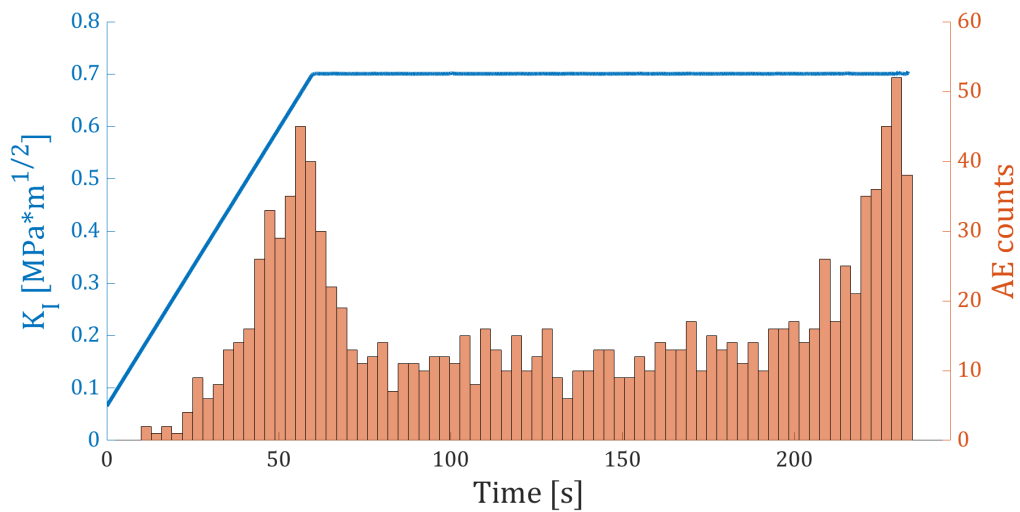


Figure 4.33: Stress intensity factor evolution coupled with AE of test G10 (creep)

According to the Griffith theory, the failure occurs when the stress intensity factor K_I reaches the mode I fracture toughness K_{IC} , but in these creep tests the crack propagation happened for lower K_I value. In this case, we talk about subcritical crack growth.

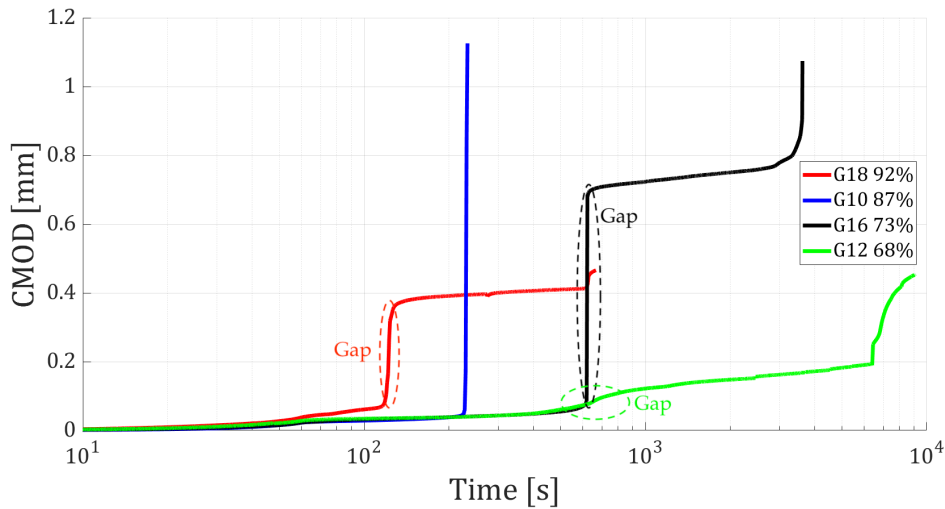


Figure 4.34: Comparison of CMOD between the mode I fracture behaviour in the creep tests

In the Figure 4.34, furthermore, it is possible to observe the same behaviour for all the samples: the presence of a well-defined gap in the ($K_I - \text{CMOD}$) plot before the sample failure. These gaps are probably due to the propagation in different times of the fracture along the superior and inferior side of the sample. This probably depends on the different stiffness of the components in contact with the rock specimen. Furthermore, the lower the failure load, the more this phenomenon is accentuated; in fact, it is not present for the tests with stress intensity factor values close to the fracture toughness. Finally, as expected, it is possible also to notice how the duration of the creep phase increases progressively with the decrease of the applied load. All the main data related to the mode I creep test are summarized in the Table 4.3.

Table 4.3: Summary of the mode I fracture toughness investigation under creep behaviour

Sample	K_I [$\text{MPa}\sqrt{\text{m}}$]	K_I/K_{Ic} [%]	Time 1 st crack propagation [s]
G18	0.73	92	120
G10	0,69	87	230
G16	0,58	73	622
G12	0,54	68	700

In the following figures (4.35 → 4.40), the acoustic emissions are plotted in function of the CMOD. The behaviour of the samples is very clear: there are peaks of acoustic emission in correspondence of the crack propagation. The

recording of acoustic emission was not possible for the test G18 due to the upgrading of the recorder machine. Finally, it is evident that the overall number of acoustic emissions recorded becomes bigger with the increasing duration of the test.

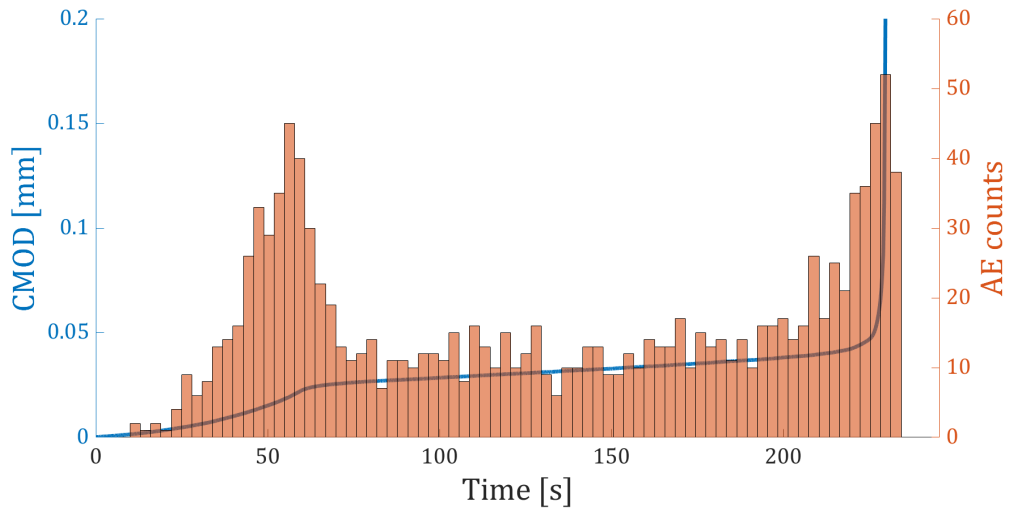


Figure 4.35: CMOD evolution coupled with AE of test G10 (creep)

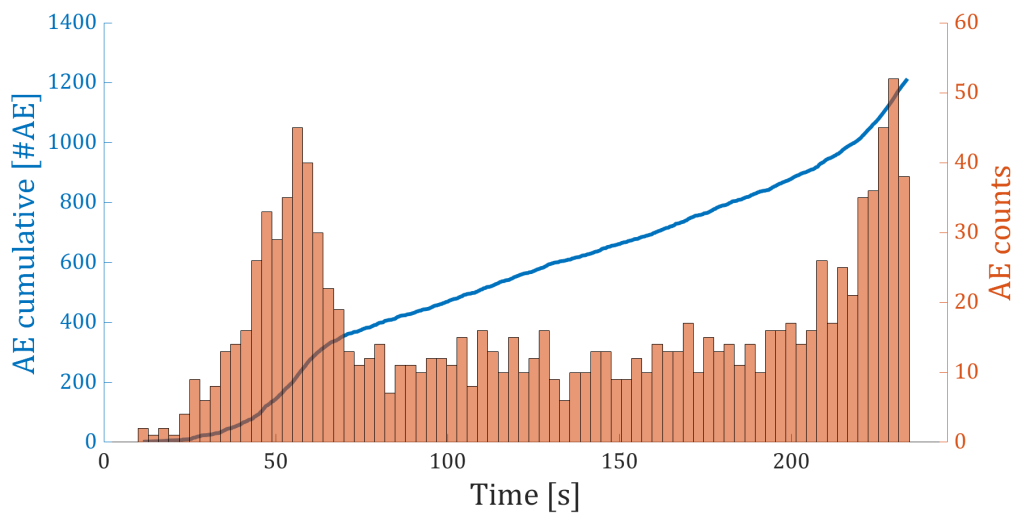


Figure 4.36: Acoustic emission cumulative evolution of test G10 (creep)

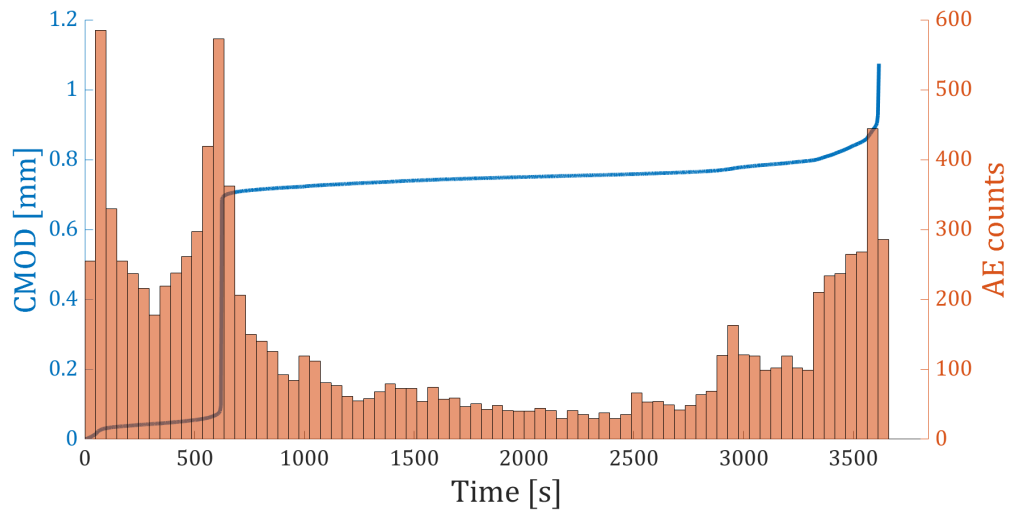


Figure 4.37: CMOD evolution coupled with AE of test G16 (creep)

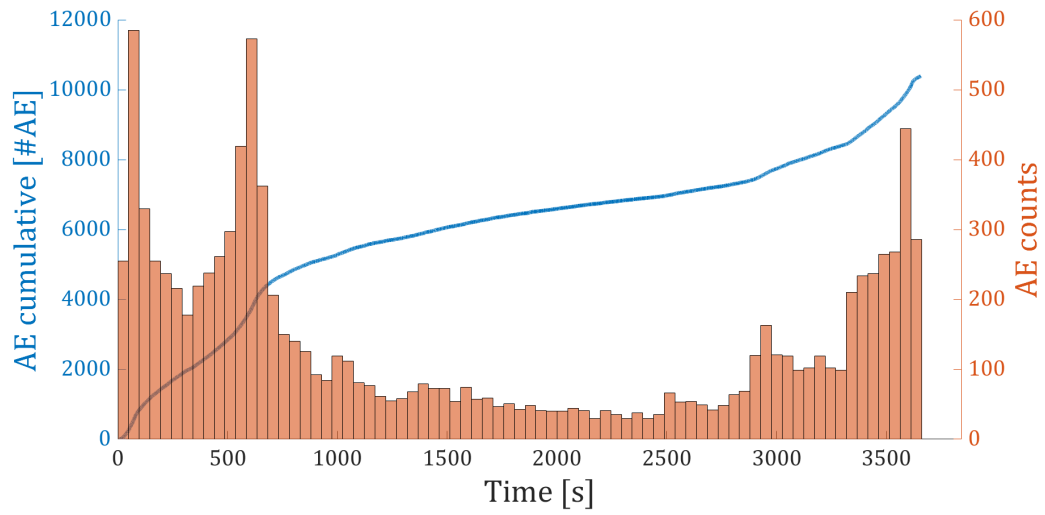


Figure 4.38: Acoustic emission cumulative evolution of test G16 (creep)

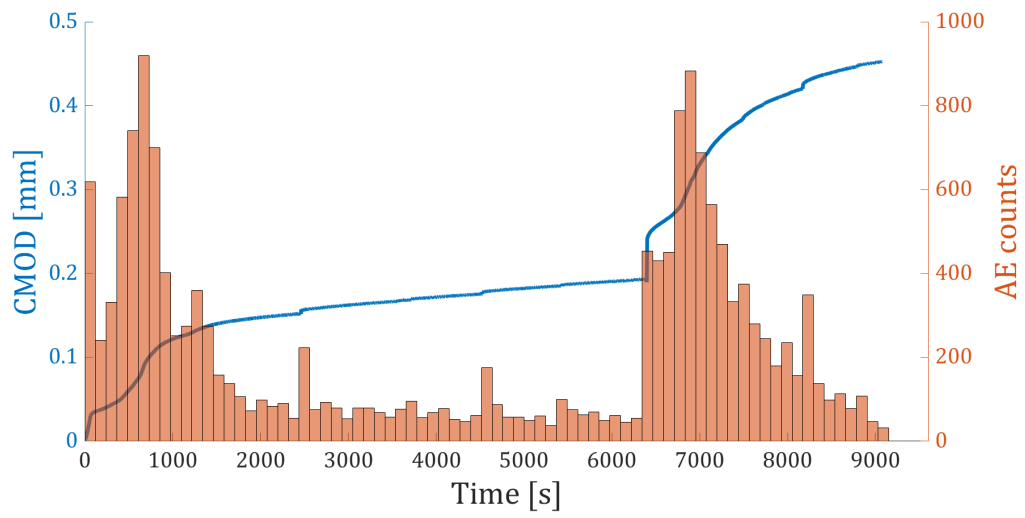


Figure 4.39: CMOD evolution coupled with AE of test G12 (creep)

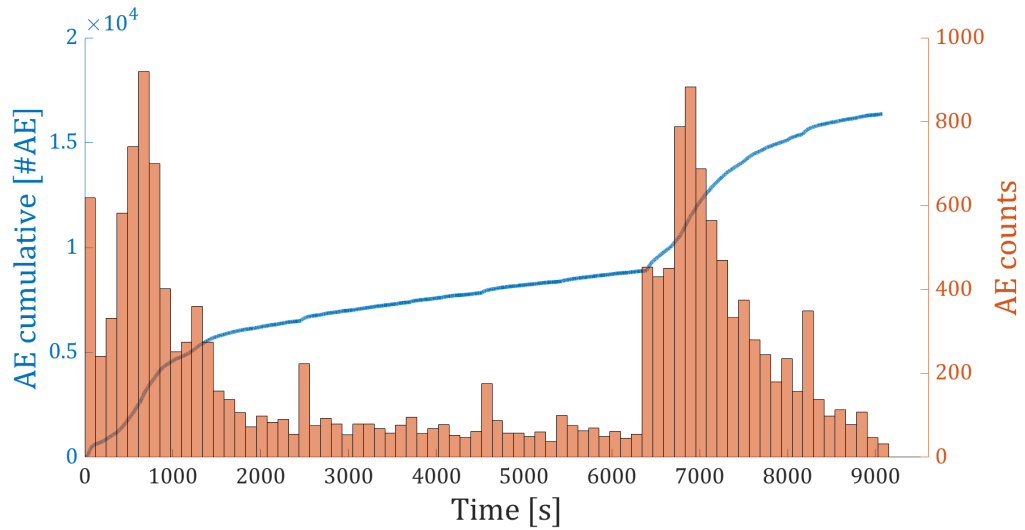


Figure 4.40: Acoustic emission cumulative evolution of test G12 (creep)

4.2.3 Mode I fracture toughness with cyclic load (fatigue)

CCNBD samples were axially loaded with a crack inclination angle of zero ($\varphi = 0^\circ$) to provide a pure mode I loading condition. Three tests were carried out on $200^\circ C$ thermally treated samples in order to investigate the behaviour in relation to different values of load. It has been decided to analyse a thermally damaged sample, instead of an intact one, in order to identify the subcritical crack growth parameters representative of the rock in situ, in fact it is plausible to assume that there is a degradation of the rock, especially along the discontinuity. The specimens were initially loaded with a rate of 0.1 kN/s until the “average load” (loading control), and then the a cyclic load was applied with a total amplitude of 2.2 kN and a frequency of 1 Hz until failure (Figure 4.41). The axial load, the axial displacement, the crack mouth opening displacement (CMOD), and the radial and axial strain closer the two crack tips were continually recorded during the test with an acquisition frequency of 200 Hz .

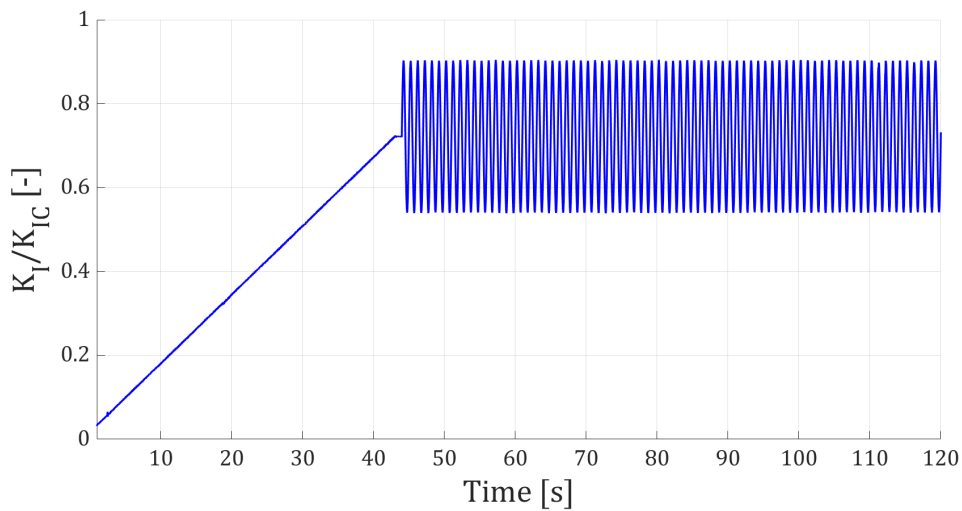


Figure 4.41: K_I/K_{IC} evolution of test G36 (cyclic)

In the following figures (4.42 → 4.48), the three experiments are reported and it is possible to notice how the CMOD rate increases when the cyclic load is applied. In the first two tests a well-defined failure of the samples can be observed while, in the third test (G24), the breakage mechanism starts to be very slow and progressive. All the main data related to the mode I creep test are summarized in the Table 4.4, where $K_{I,max}$ represents the fracture

toughness at the maximum peak of the cyclic load, $K_{I,min}$ the fracture toughness at the minimum peak of the cyclic load and $K_{I,avg}$ is the average fracture toughness applied on the sample.

Table 4.4: Summary of the mode I fracture toughness investigation under cyclic load

Sample	$K_{I,max}/K_{IC}$ [%]	$K_{I,avg}/K_{IC}$ [%]	$K_{I,min}/K_{IC}$ [%]	Time of failure [s]
G36	90	72	54	110
G17	87	69.5	52	340
G24	81.5	63.5	45.5	1500

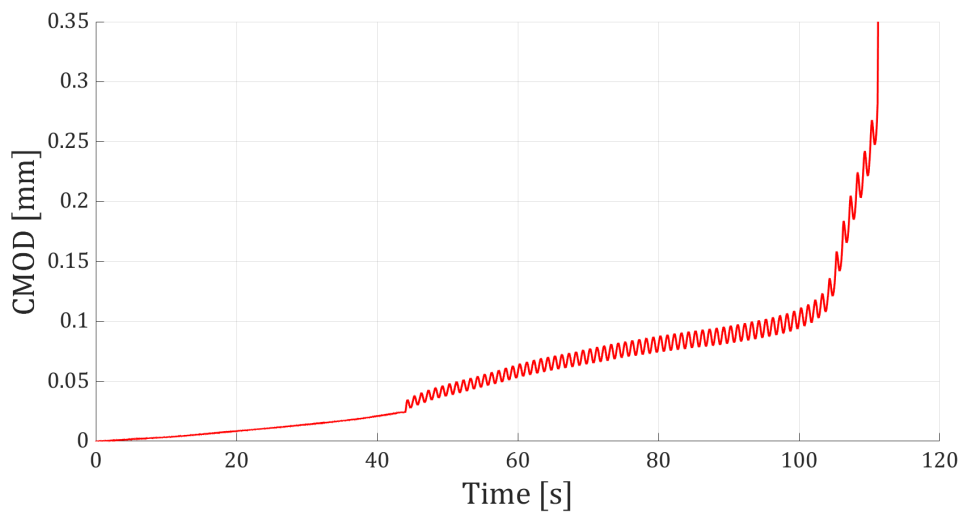


Figure 4.42: CMOD evolution of test G36 (cyclic)

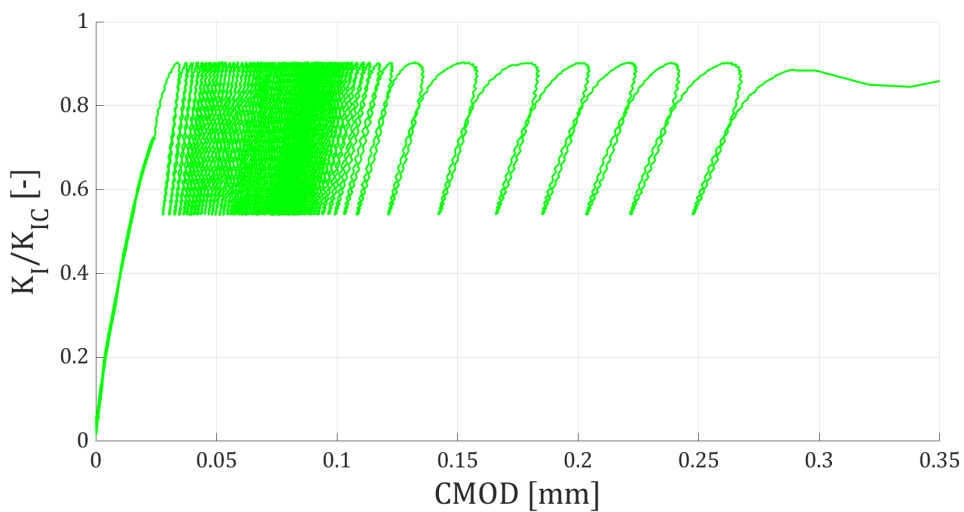


Figure 4.43: K_I/K_{IC} in function of the CMOD of test G36 (cyclic)

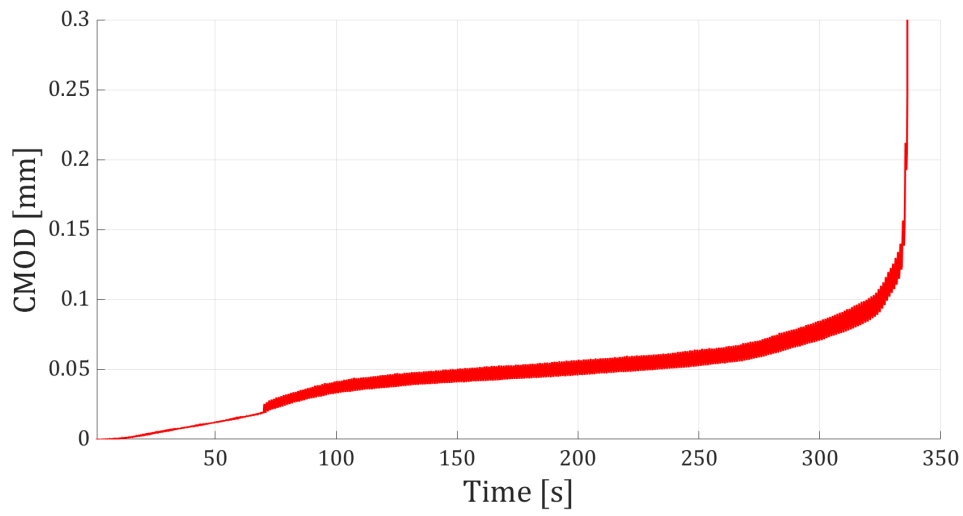


Figure 4.44: CMOD evolution of test G17 (cyclic)

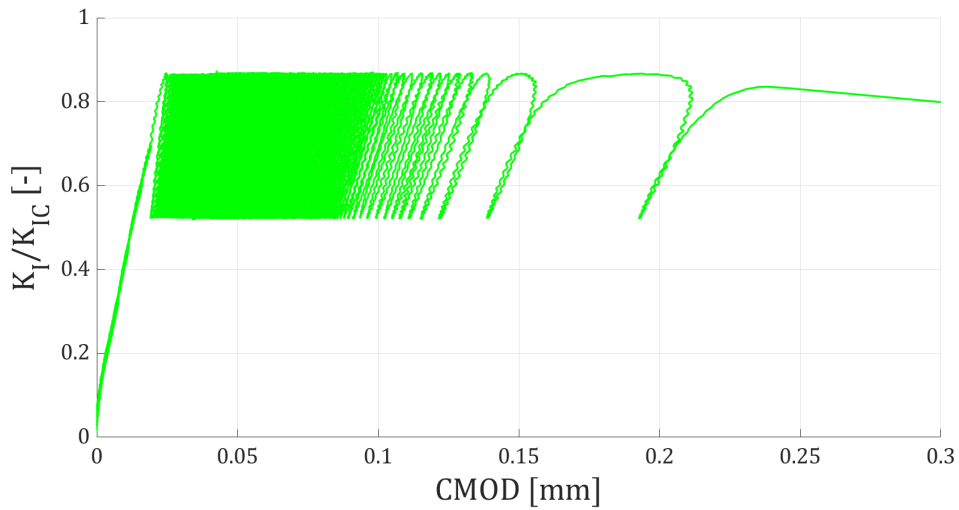


Figure 4.45: K_I/K_{Ic} in function of the CMOD of test G17 (cyclic)

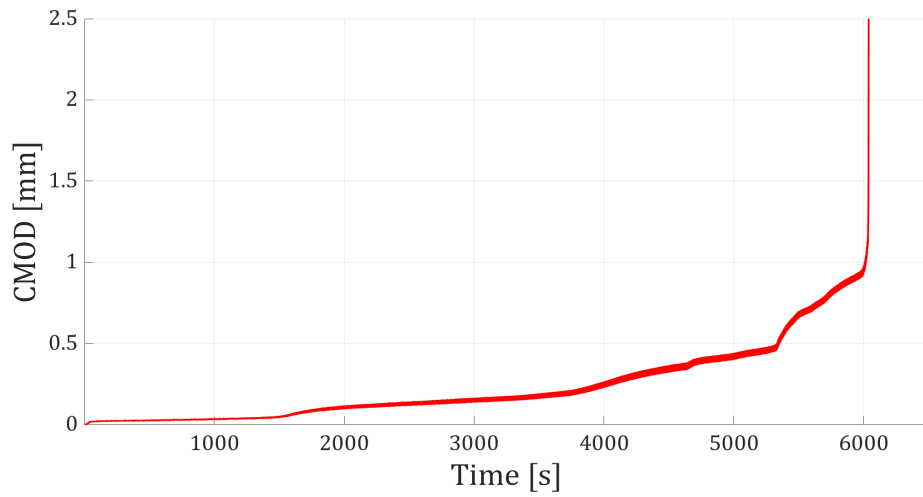


Figure 4.46: CMOD evolution of test G24 (cyclic)

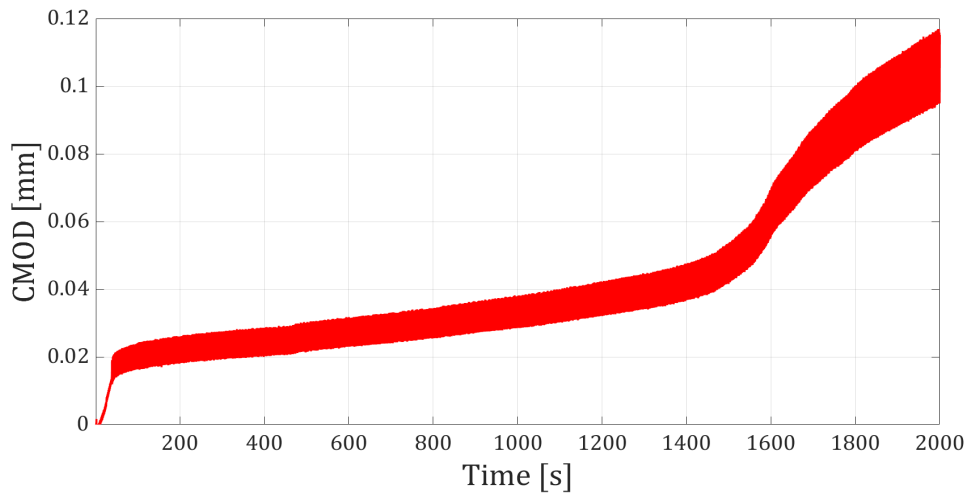


Figure 4.47: Detail of the first crack propagation in the CMOD evolution of test G24 (cyclic)

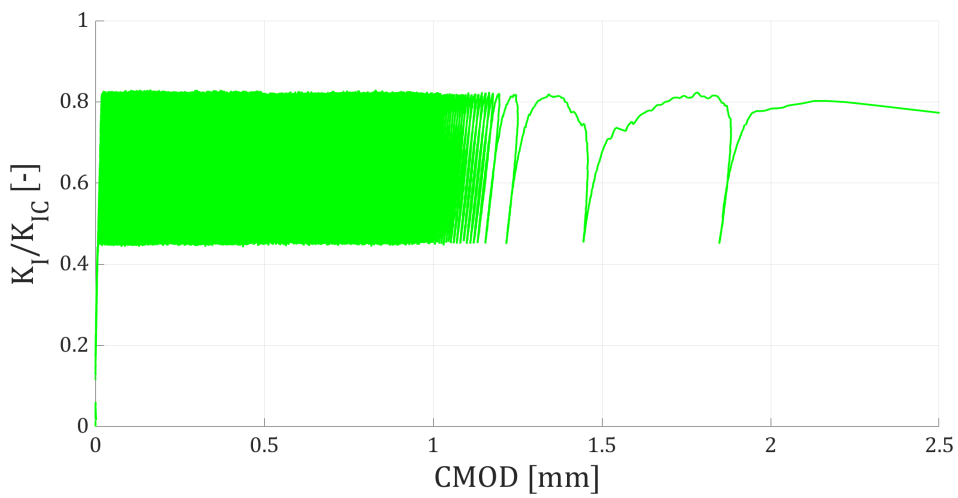


Figure 4.48: K_I/K_{IC} in function of the CMOD of test G24 (cyclic)

The comparison between the static and cyclic tests is also very interesting. In the Table 4.5, a comparison between these two types of test has been done considering the maximum stress intensity factor $K_{I,max}$ applied during the tests. The specimen's failure occurs almost at the same moment for the highest percentage of loading, while the more the force applied decreases, the more there is difference between the tests. In particular, the creep test results more damaging for the rock than the cyclic test: the G16 samples failure occurs in 620 s with a percentage of 73.5 % of fracture toughness applied, while, in the sample G24, it occurs in 1500 s with an higher percentage of fracture toughness applied.

Table 4.5: Comparison between creep and cyclic tests based on $K_{I,max}$

Creep tests			Cyclic tests		
Sample	K_I/K_{IC} [%]	Time of failure [s]	Sample	$K_{I,max}/K_{IC}$ [%]	Time of failure [s]
G18	92	120	G36	90	110
G10	86.5	230	G17	87	340
G16	73.5	620	G24	81.5	1500

In the Table 4.6, instead, the comparison has been done considering the average stress intensity factor $K_{I,avg}$ applied during the tests. For example, this could be the case of a cyclic thermal load which overlaps the pre-existing stress state. In this case the failure is reached much faster in the cyclic tests, indeed, the G16 samples failure occurs in 620 s while, in the sample G36, it occurs in 110 s.

Table 4.6: Comparison between creep and cyclic tests based on $K_{I,avg}$

Creep tests			Cyclic tests		
Sample	K_I/K_{IC} [%]	Time of failure [s]	Sample	$K_{I,avg}/K_{IC}$ [%]	Time of failure [s]
G18	92	120	G36	72	110
G10	86.5	230	G17	69.5	340
G16	73.5	620	G24	63.5	1500

4.3 Mode II fracture toughness investigation

The mode II fracture toughness for the CCNBD specimen can be evaluated from:

$$K_{IIc} = \frac{P_{max}}{\sqrt{\pi RB}} \sqrt{\frac{a}{R}} \sqrt{\frac{a_1 - a_0}{a - a_0}} N_{II}(a/R) \quad (4.5)$$

where the mode II geometry factor N_{II} is a function of the non-dimensional crack length ratio (a/R), where R is the radius and a is the initial chevron-notched crack length. The crack inclination angle ϕ corresponding to pure mode II depends also on a/R . The Table 4.7 shows the values of N_{II} and ϕ for the CCNBD specimen derived from previous numerical and analytical analysis [22].

Table 4.7: Values of ϕ and N_{II} for different crack length ratios a/R in the CCNBD specimen

a/R [-]	0.1	0.2	0.3	0.4	0.5	0.6
ϕ [°]	29.6	28.7	27.2	25.4	23.3	21.3
N_{II} [-]	1.764	1.804	1.865	1.992	2.184	2.481

Following the values indicated in the Table 4.7, two mode II fracture toughness tests were performed on samples G1 and G2, which were tilted of 24.7° and 24.2° with respect to the vertical loading axis. The tests were carried with displacement control until failure and with a displacement rate of 0.01 mm/s . The axial load, the axial displacement, the crack mouth opening displacement (CMOD), and the radial and axial strain closer the two crack tips were continually recorded during the test with an acquisition frequency of 200 Hz . The samples have been thermally treated at 200° C in order to have the most consistent parameters possible in order to emulate the rock degradation in situ. During the two tests, although the geometries of the samples were not identical, I obtained an almost identical mode II fracture toughness which is higher than the mode I value, as expected. The final results are rather low compared to the values of the literature [22][23][24], but it has

to be considered that the test was performed on thermally treated samples. The results are shown in the Table 4.8.

Table 4.8: Geometrical and mechanical parameters of mode II fracture toughness test

Sample	a [mm]	R [mm]	a/R [-]	φ [°]	N_{II} [-]	K_{IIc} [MPa \sqrt{m}]
G1	17.4	39.9	0.435	24.7	2.059	1.158
G2	18.1	39.8	0.454	24.2	2.096	1.146



Figure 4.49: G1 sample during the mode II fracture toughness test

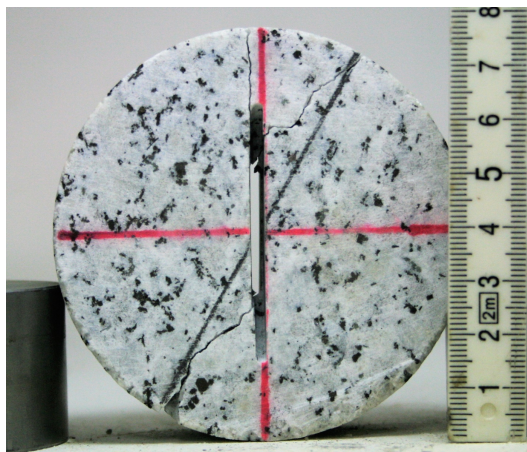


Figure 4.50: Picture of the G1 sample after the failure with a tilted crack propagation

Chapter 5

Subcritical crack growth

Subcritical crack growth is time-dependent crack growth at a value of stress intensity factor that may be lower than the critical value of the fracture toughness K_{IC} . Subcritical crack growth is an important way to evaluate the long-term stability problems of structures in rocks and it can be described by a relationship between the stress intensity factor and the crack velocity. According to the subcritical crack growth velocities, they were calculated through the derivative of the crack mouth opening displacement (CMOD) starting from the beginning of the creep phase until the reaching the first crack propagation. The lowest values were approximated to the nearest integer value. The results of the subcritical crack growth velocities is reported in the Table 5.1 and it has been done only for the creep test.

Table 5.1: Subcritical crack growth velocity computed from the creep tests

Sample	Thermal treatment	K_I/K_{IC} [%]	Subcritical crack growth velocity [mm/s]
G18	200° C	92	$5 \cdot 10^{-4}$
G10	200° C	87	$8 \cdot 10^{-5}$
G16	200° C	73.5	$3 \cdot 10^{-5}$
G12	200° C	68	$5 \cdot 10^{-6}$

5.1 Investigation for 200° C thermally treated granite

Under static loads, due to stress corrosion by an environment agent, crack velocity is often characterized by the Charles power-law [11]:

$$v = v_0 e^{\left(\frac{-H}{RT}\right)} K_I^n \quad (5.1)$$

where, v is the crack propagation velocity, v_0 and n are constants, H is the activation enthalpy, R is the gas constant, T is the absolute temperature, and K_I is the mode I stress intensity factor. In many studies [27][28][29], it is shown that the equation 5.1 can be reduced as:

$$v = A^* K_I^n = A \left(\frac{K_I}{K_{IC}}\right)^n \quad (5.2)$$

where, A and n are subcritical crack growth parameters, and K_{IC} is the mode I fracture toughness. Sometimes n is also called the subcritical crack growth index, and it is a function of the internal damage of the rock (Figure 5.1), while A represents the crack propagation velocity when the stress intensity factor K_I is equal to the mode I fracture toughness K_{IC} [30]. By using the logarithm rules the following formula is derived:

$$\log(v) = \log(A) + n \log\left(\frac{K_I}{K_{IC}}\right) \quad (5.3)$$

The crack propagation velocity v has been already calculated for each K_I/K_{IC} ratio, then it is sufficient to plot $\log(K_I/K_{IC})$ along the x-axis and $\log(v)$ along the y-axis (Figure 5.2). In this way, through the points' interpolation, the slope of the graph obtained represents the parameter n , while the parameter A is the intercept with the y-axis.

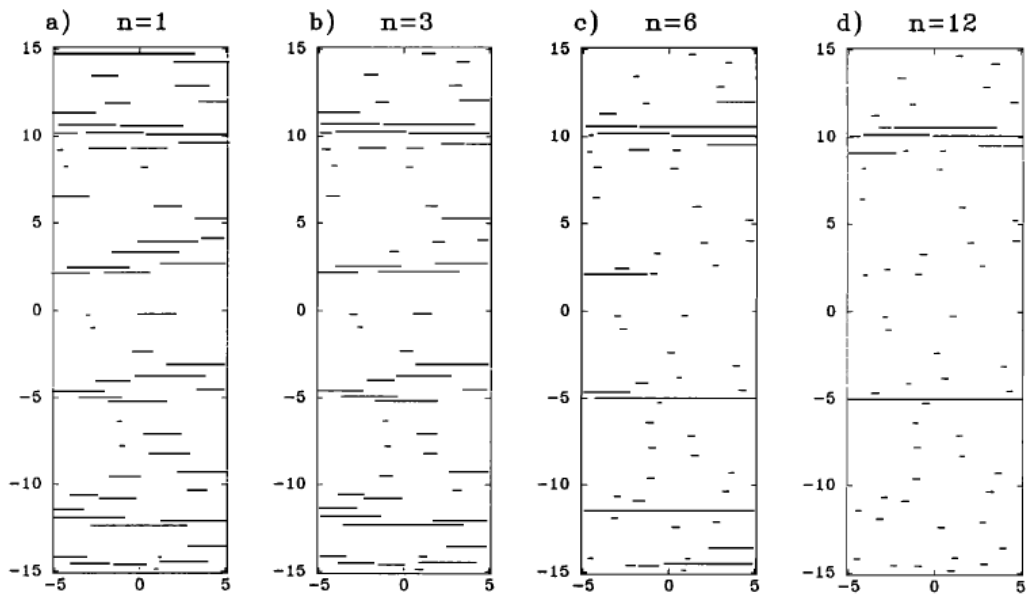


Figure 5.1: Subcritical fracture growth patterns [29]

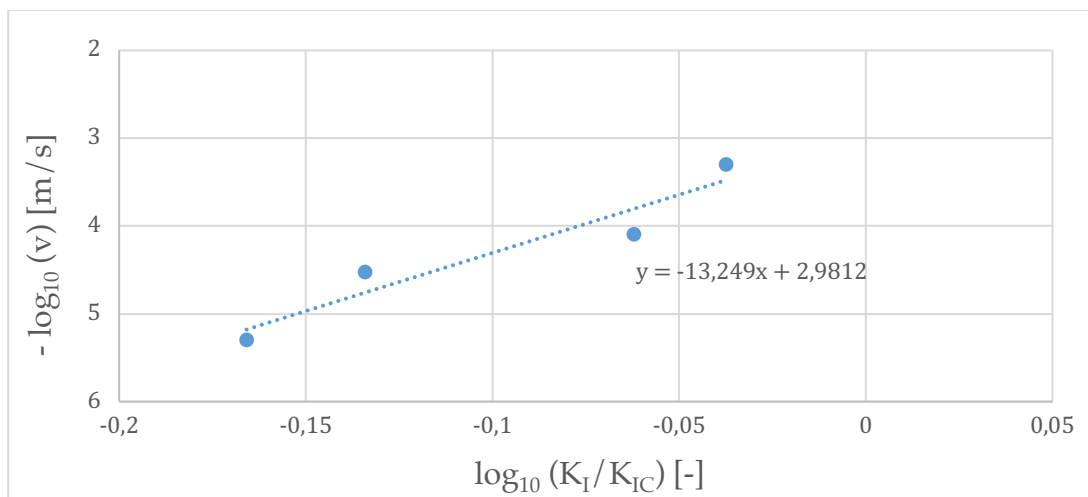


Figure 5.2: Subcritical crack growth parameters determination for creep tests

From the Figure 5.1, n is 13.2 while A is equal to $1 \cdot 10^{-3} \text{ mm/s}$. The value n is rather low if compare with the literature [30][31], but it is necessary to consider that these parameters are referred to a thermally treated granite, therefore it is reasonable to expect a lower parameters n than an intact granite.

5.2 Investigation for different thermally treated granites

In the chapter 5.1, the subcritical crack growth parameters of the 200°C thermally treated granite have been computed through the analysis of the four creep tests. Then, we searched for a way to calculate these parameters only with one test. For this reason, two more tests on 200°C samples (G3 and G23) have been performed by applying different increasing loads. The loads have been kept constant for 90 s in order to give time to the sample to creep, in fact, in the previous tests the minimum value of the subcritical crack velocity was often reached after about 50 s from the application of the load. Then, the load has been increased with a rate of 0.1 kN/s (Figure 5.3 and 5.5). The plan of the two tests is summarized in the Tables 5.2 and 5.3.

Table 5.2: Loading path for the test on G3

Step	Control	Time [s]	Initial load [kN]	Final load [kN]	K_I/K_{Ic} [%]
1	Load	31	0	3.1	-
2	Load	90	3.1	3.1	55
3	Load	3	3.1	3.4	-
4	Load	90	3.4	3.4	60
5	Load	3	3.4	3.7	-
6	Load	90	3.7	3.7	65.5
7	Load	3	3.7	4	-
8	Load	90	4	4	71
9	Load	3	4	4.3	-
10	Load	90	4.3	4.3	76
11	Load	3	4.3	4.6	-
12	Load	90	4.6	4.6	81.5
13	Load	3	4.6	4.9	-
14	Load	90	4.9	4.9	87
15	Load	3	4.9	5.2	-
16	Load	90	5.2	5.2	92

Table 5.3: Loading path for the test on G23

Step	Control	Time [s]	Initial load [kN]	Final load [kN]	K_I/K_{IC} [%]
1	Load	44	0	4.4	-
2	Load	90	4.4	4.4	71
3	Load	3	4.4	4.7	-
4	Load	90	4.7	4.7	75.5
5	Load	3	4.7	5	-
6	Load	90	5	5	80.5
7	Load	3	5	5.3	-
8	Load	90	5.3	5.3	85
9	Load	3	5.3	5.6	-
10	Load	90	5.6	5.6	90

The failure of the sample G3 occurred at the step 9, while for the sample G23 it happened only at the end of the last step. In the following figures (5.3 → 5.6), the ratio K_I/K_{IC} and the CMOD are plotted in function of the time, and they are referred only to the firsts 9 steps for the sample G3.

The final aim of these tests is to compute the subcritical crack growth velocity v for each ratio K_I/K_{IC} through the derivative of the crack mouth opening displacement (CMOD). In this way a large number of points can be plotted on the plane $\log(K_I/K_{IC}) - \log(v)$ only with one test. Hence, it is possible to evaluate the subcritical crack growth parameters as described in the section 5.1

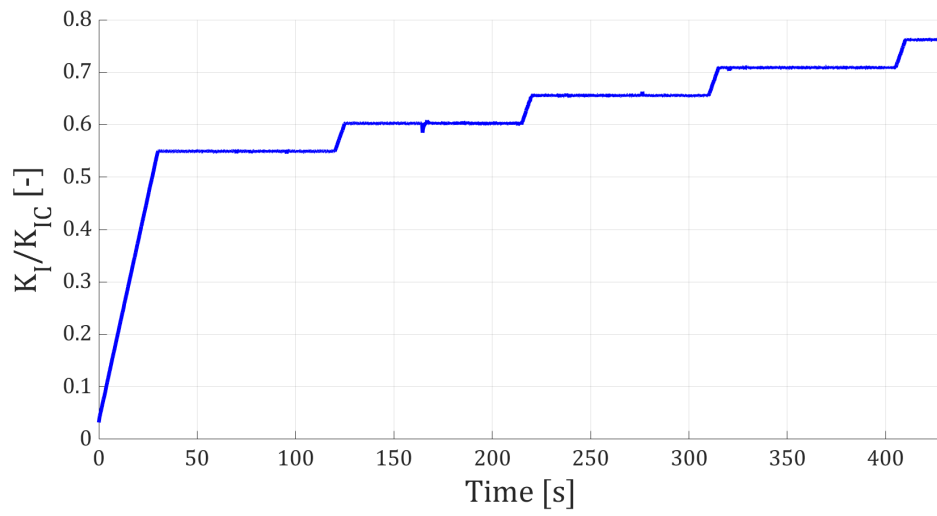


Figure 5.3: K_I/K_{IC} evolution of test G3

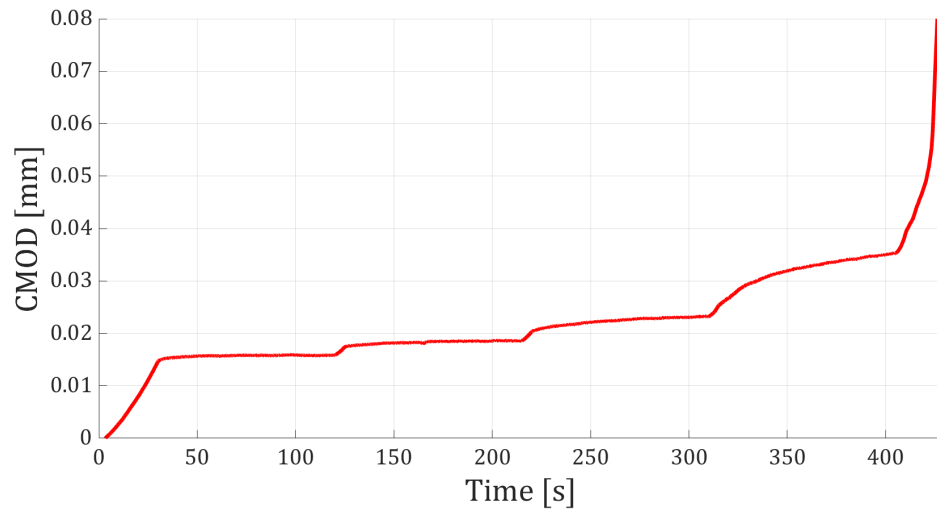


Figure 5.4: CMOD evolution of test G3

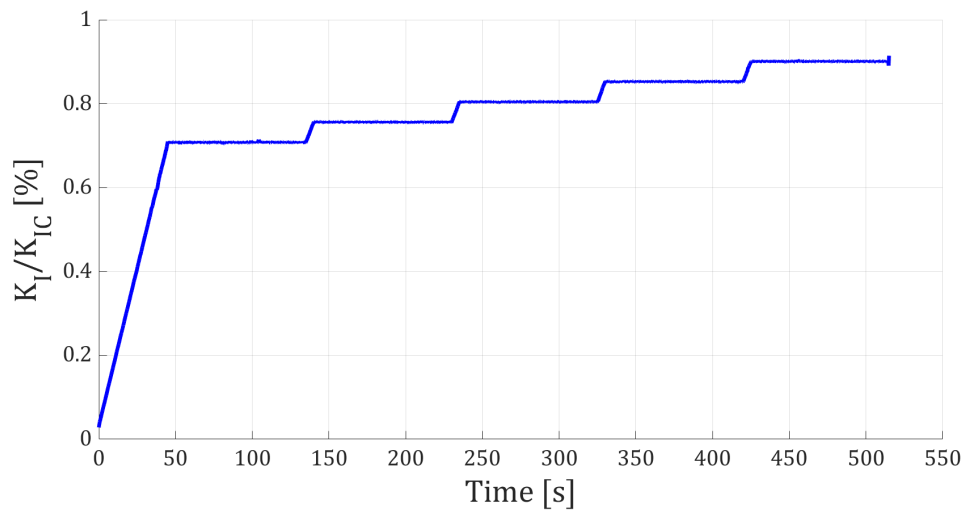
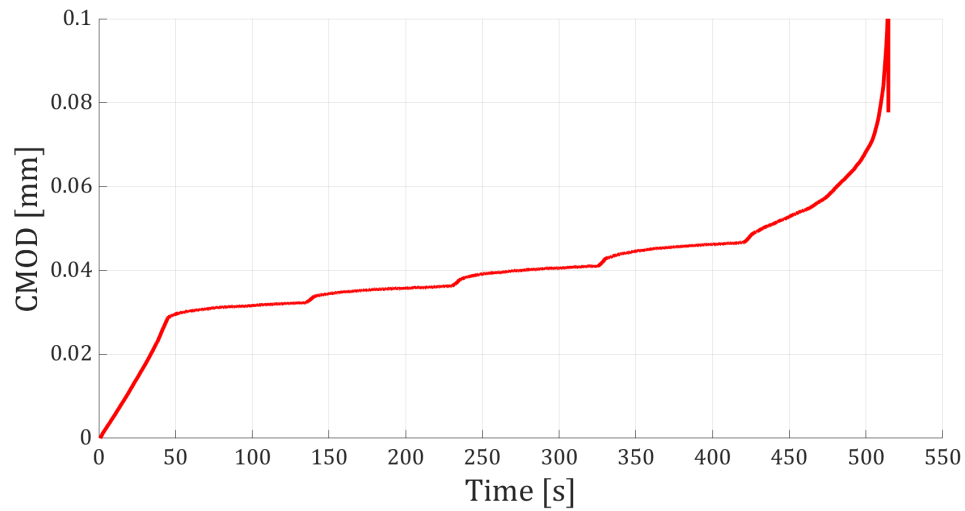
Figure 5.5: K_I/K_{IC} evolution of test G23

Figure 5.6: CMOD evolution of test G23

In the Tables 5.4 and 5.5, the subcritical crack growth velocity v are reported for each ratio K_I/K_{IC} , while the subcritical crack growth parameters are analysed in the Figures 5.7 and 5.8.

Table 5.4: Subcritical crack growth velocity computation for G3 sample

Step	K_I/K_{IC} [%]	Subcritical crack growth velocity [mm/s]
2	55	$1 \cdot 10^{-6}$
4	60	$3 \cdot 10^{-6}$
6	65.5	$7.5 \cdot 10^{-6}$
8	71	$3.5 \cdot 10^{-5}$

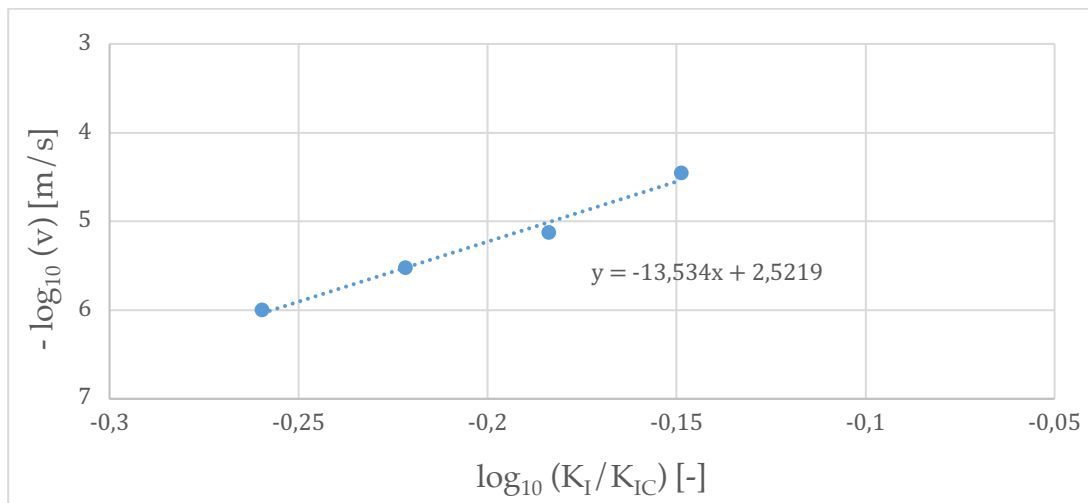


Figure 5.7: Subcritical crack growth parameters determination for sample G3

Table 5.5: Subcritical crack growth velocity computation for G23 sample

Step	K_I/K_{IC} [%]	Subcritical crack growth velocity [mm/s]
2	71	$1.25 \cdot 10^{-5}$
4	75.5	$2.5 \cdot 10^{-5}$
6	80.5	$4 \cdot 10^{-5}$
8	85	$7 \cdot 10^{-5}$
10	90	$3 \cdot 10^{-4}$

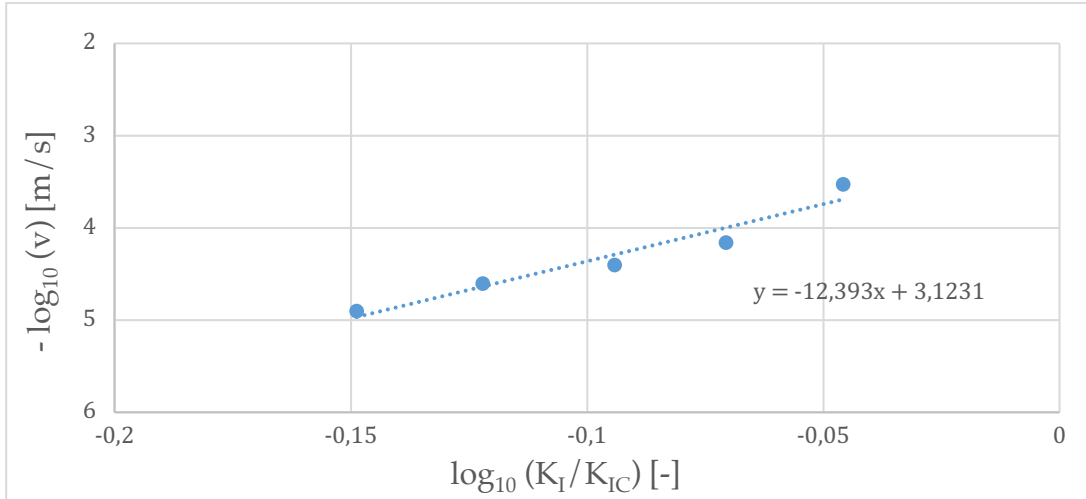


Figure 5.8: Subcritical crack growth parameters determination for sample G23

The consistency of these tests can be demonstrated through the comparison of the subcritical crack growth parameters (Table 5.6). The differences between the values obtained are very small and this confirms the possibility of carrying out this type of experiment for the calculation of the subcritical parameters for different thermally treated samples. Finally, in the Figure 5.9 all the points, calculated throughout all the tests, show a well-defined trendline. Thus, the next goal will be to analyse:

- 100°C thermally treated;
- 300°C thermally treated;
- 400°C thermally treated;

Table 5.6: Comparison of subcritical crack growth parameters for 200° C treated samples

	Creep tests	G3	G23
$n [-]$	13.2	13.5	12.4
$A [mm/s]$	$1 \cdot 10^{-3}$	$3 \cdot 10^{-3}$	$8 \cdot 10^{-4}$

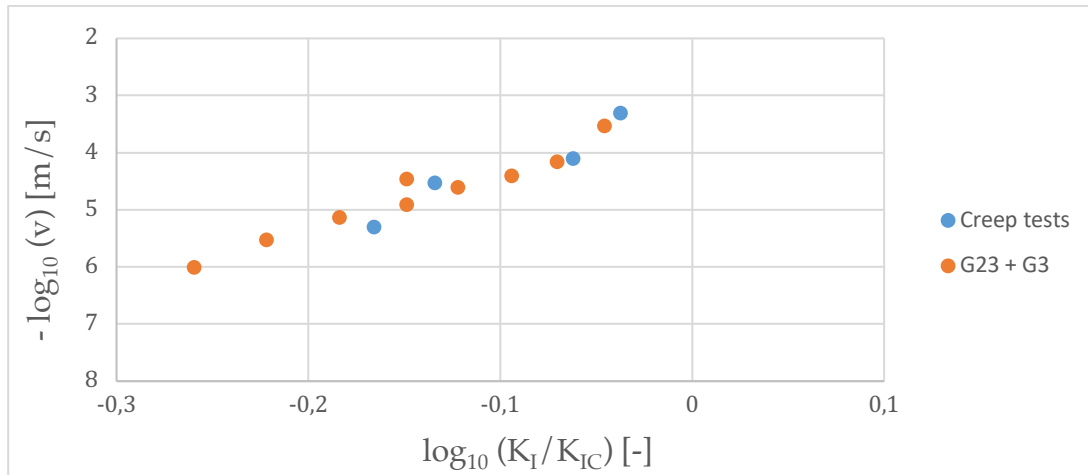


Figure 5.9: Comparison between subcritical crack growth parameters

5.2.1 100° C thermally treated sample (G32)

The sample G32 has been tested according to the schedule shown in the Table 5.7, leaving the sample deforming for creep 115 s. The failure occurred after the step 12 (Figure 5.10 and 5.11), and the subcritical crack growth was visible only during the steps 10 and 12 (Table 5.8) that means only two points for the determination of the subcritical crack growth parameters (Figure 5.12).

Table 5.7: Loading path for the test on G32

Step	Control	Time [s]	Initial load [kN]	Final load [kN]	K_I/K_{IC} [%]
1	Load	46	0	4.6	-
2	Load	115	4.6	4.6	65
3	Load	4	4.6	5	-
4	Load	115	5	5	70,5
5	Load	4	5	5.4	-
6	Load	115	5.4	5.4	76
7	Load	4	5.4	5.8	-
8	Load	115	5.8	5.8	82
9	Load	4	5.8	6.2	-
10	Load	115	6.2	6.2	87,5
11	Load	4	6.2	6.6	-
12	Load	115	6.6	6.6	93

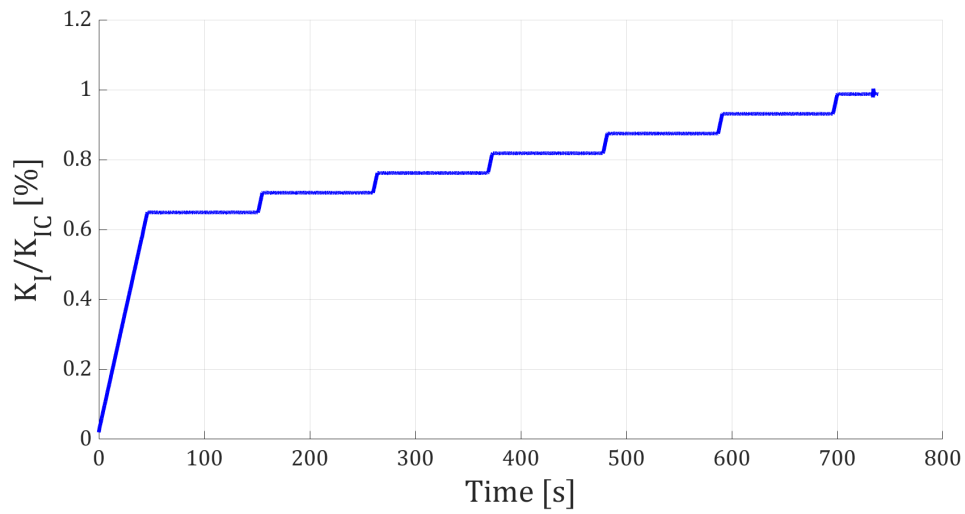
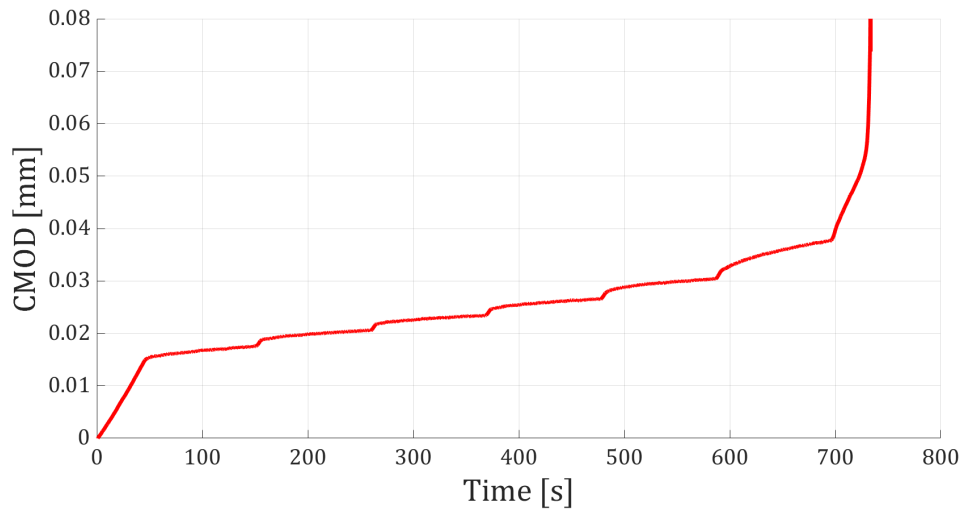
Figure 5.10: K_I/K_{IC} evolution of test G32

Figure 5.11: CMOD evolution of test G32

Table 5.8: Subcritical crack growth velocity computation for G32 sample

Step	K_I/K_{IC} [%]	Subcritical crack growth velocity [mm/s]
10	87.5	$1.5 \cdot 10^{-5}$
12	93	$4.5 \cdot 10^{-5}$

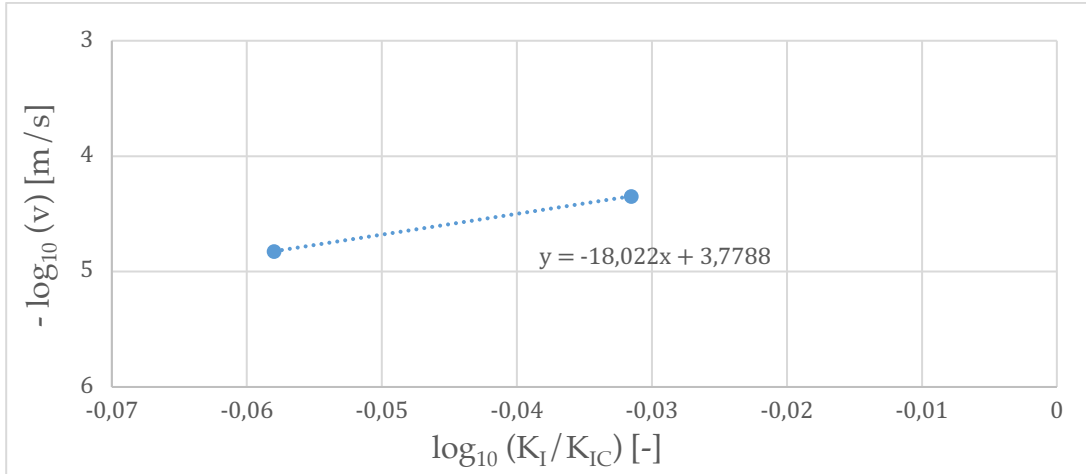


Figure 5.12: Subcritical crack growth parameters determination for sample G32

From the Figure 5.12, n is 18 while A is equal to $1.5 \cdot 10^{-4} \text{ mm/s}$.

5.2.2 300° C thermally treated sample (G31)

The sample G31 has been tested according to the schedule shown in the Table 5.9, leaving the sample deforming for creep 75 s. The failure occurred after the step 8 (Figure 5.13 and 5.14), and the subcritical crack growth was analysed during the steps 2, 4, 6 and 8 (Table 5.10) that means four points for the determination of the subcritical crack growth parameters (Figure 5.15).

Table 5.9: Loading path for the test on G31

Step	Control	Time [s]	Initial load [kN]	Final load [kN]	K_I/K_{IC} [%]
1	Load	35	0	3.5	-
2	Load	75	3.5	3.5	59
3	Load	3	3.5	3.8	-
4	Load	75	3.8	3.8	64
5	Load	3	3.8	4.1	-
6	Load	75	4.1	4.1	69
7	Load	4	4.1	4.5	-
8	Load	75	4.5	4.5	76

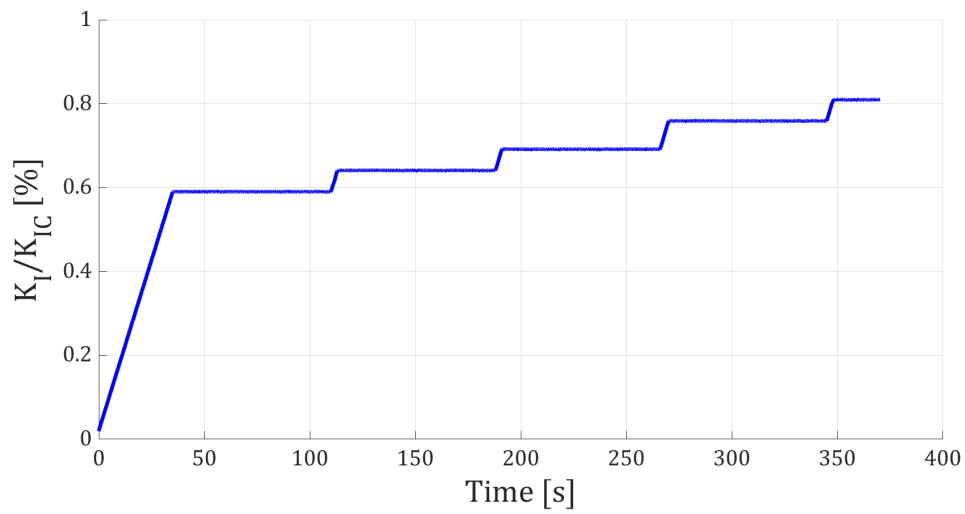
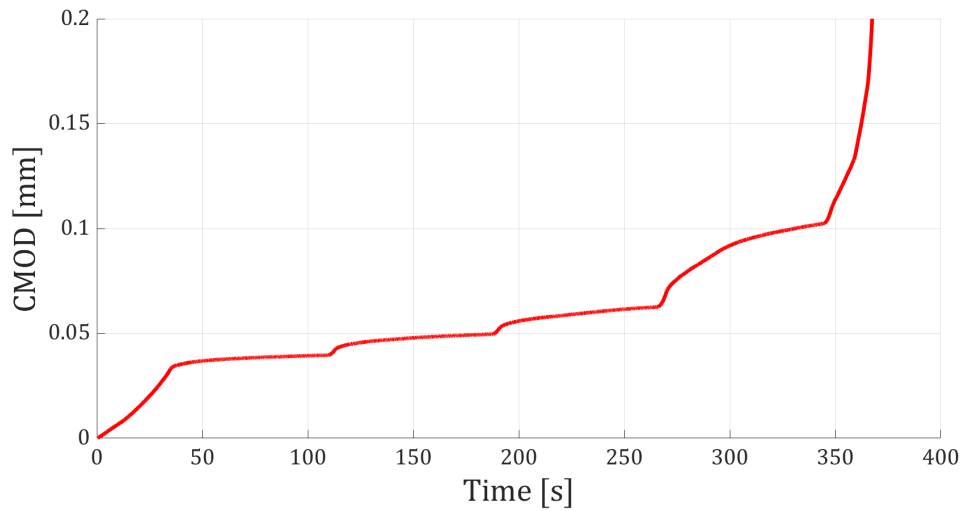
Figure 5.13: K_I/K_{IC} evolution of test G31

Figure 5.14: CMOD evolution of test G31

Table 5.10: Subcritical crack growth velocity computation for G31 sample

Step	K_I/K_{IC} [%]	Subcritical crack growth velocity [mm/s]
2	59	$2 \cdot 10^{-5}$
4	64	$4 \cdot 10^{-5}$
6	69	$7 \cdot 10^{-5}$
8	76	$2 \cdot 10^{-4}$

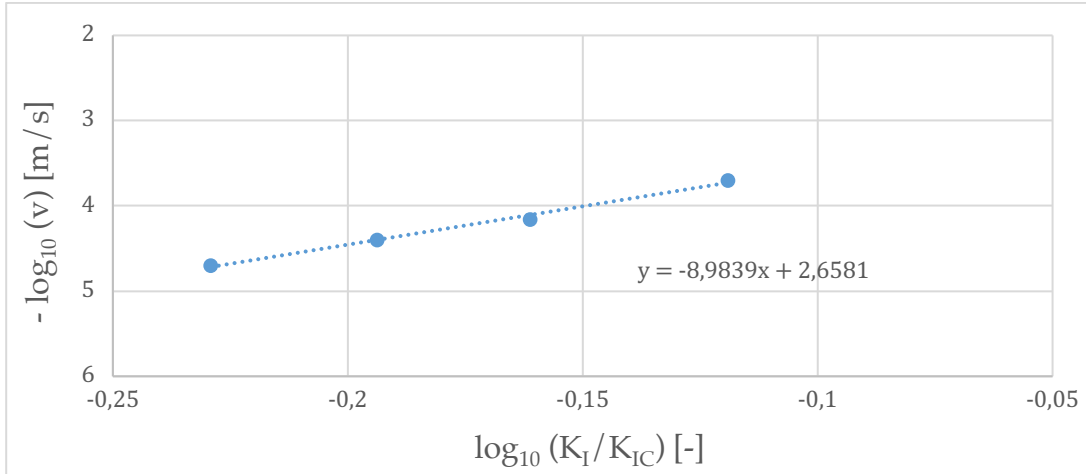


Figure 5.15: Subcritical crack growth parameters determination for sample G31

From the Figure 5.15, n is 9 while A is equal to $2 \cdot 10^{-3} \text{ mm/s}$.

5.2.2 400° C thermally treated sample (G30)

The sample G30 has been tested according to the schedule shown in the Table 5.11, leaving the sample deforming for creep 60 s. The failure occurred after the step 10 (Figure 5.16 and 5.17), and the subcritical crack growth was analysed during the steps 2, 4, 6, 8 and 10 (Table 5.12) that means five points for the determination of the subcritical crack growth parameters (Figure 5.18).

Table 5.11: Loading path for the test on G30

Step	Control	Time [s]	Initial load [kN]	Final load [kN]	K_I/K_{IC} [%]
1	Load	31	0	3.1	-
2	Load	60	3.1	3.1	60.5
3	Load	3	3.1	3.4	-
4	Load	60	3.4	3.4	66
5	Load	3	3.4	3.7	-
6	Load	60	3.7	3.7	72
7	Load	3	3.7	4	-
8	Load	60	4	4	78
9	Load	3	4	4.3	-
10	Load	60	4.3	4.3	84

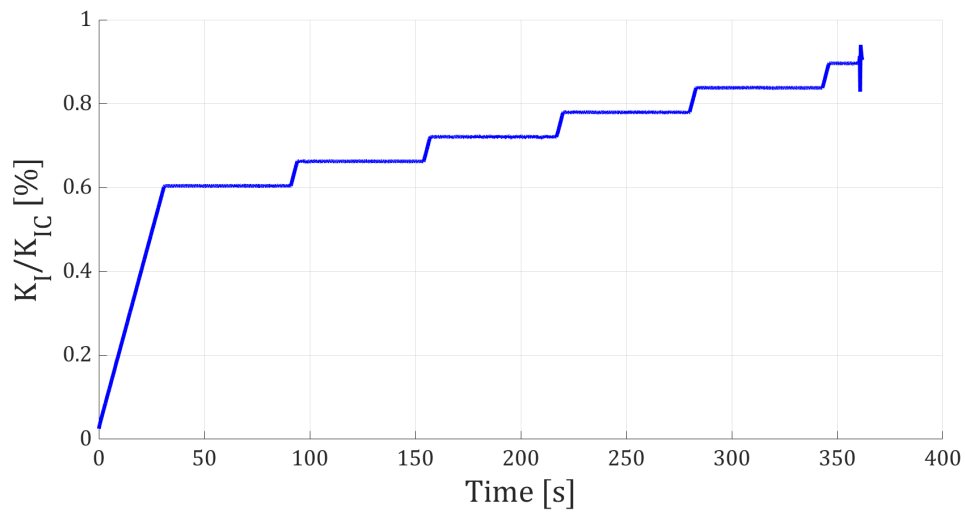
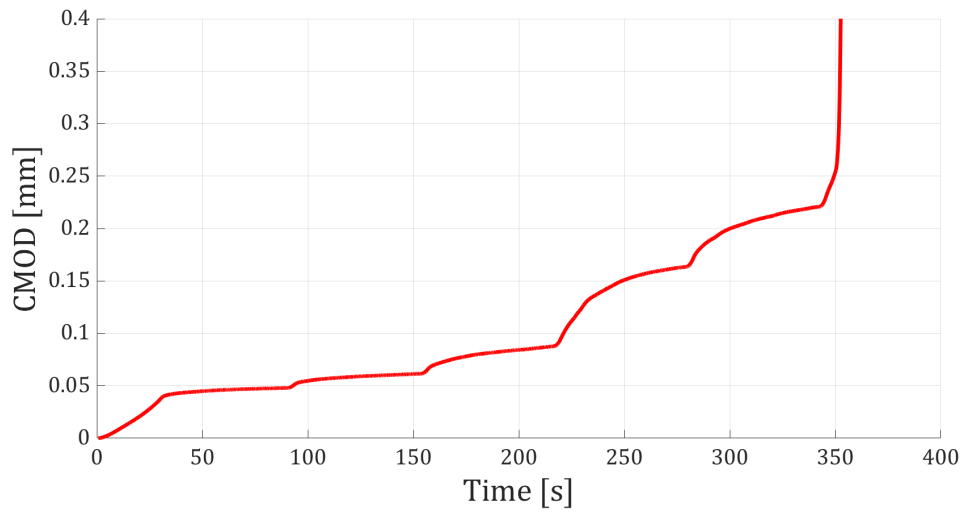
Figure 5.16: K_I/K_{IC} evolution of test G30

Figure 5.17: CMOD evolution of test G30

Table 5.12: Subcritical crack growth velocity computation for G30 sample

Step	K_I/K_{IC} [%]	Subcritical crack growth velocity [mm/s]
2	60.5	$5.5 \cdot 10^{-5}$
4	66	$8.5 \cdot 10^{-5}$
6	72	$2 \cdot 10^{-4}$
8	78	$4 \cdot 10^{-4}$
10	84	$5.5 \cdot 10^{-4}$

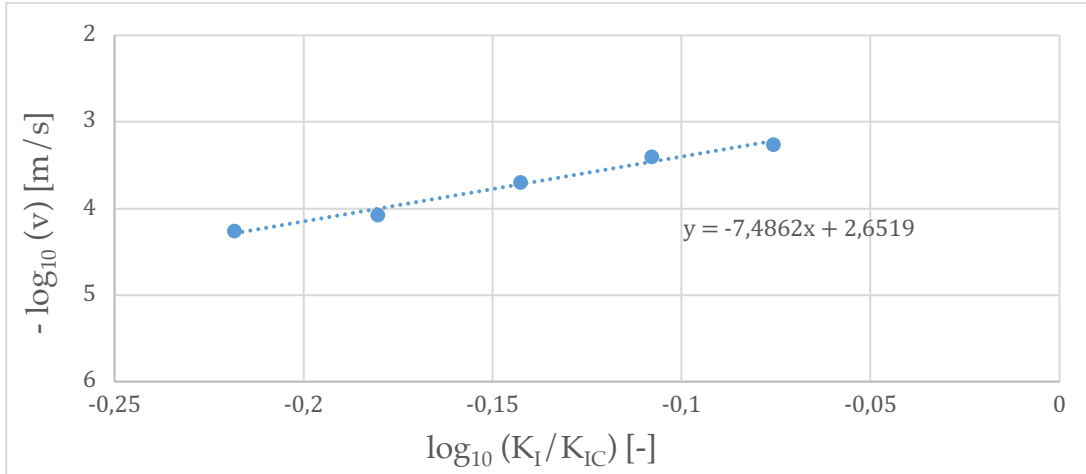


Figure 5.18: Subcritical crack growth parameters determination for sample G30

From the Figure 5.18, n is 7.5 while A is equal to $2 \cdot 10^{-3} \text{ mm/s}$.

5.3 Concluding remarks

The data obtained seem to be very consistent. In fact, as expected, the internal damage index n progressively decreases to increasing the temperature of the thermal treatment (Table 5.13). The velocity A , instead, is almost constant for all the samples which could mean that it is not a function of the internal damage. Finally, in the Figure 5.19 the difference between the tested specimen are clearly visible, recalling that the slope of the lines is related to the parameter n .

Table 5.13: Comparison between subcritical crack growth parameters

	100° C	200° C	300° C	400° C
$n [-]$	18	13.2	9	7.5
$A [mm/s]$	$1.5 \cdot 10^{-4}$	$1 \cdot 10^{-3}$	$2 \cdot 10^{-3}$	$2 \cdot 10^{-3}$

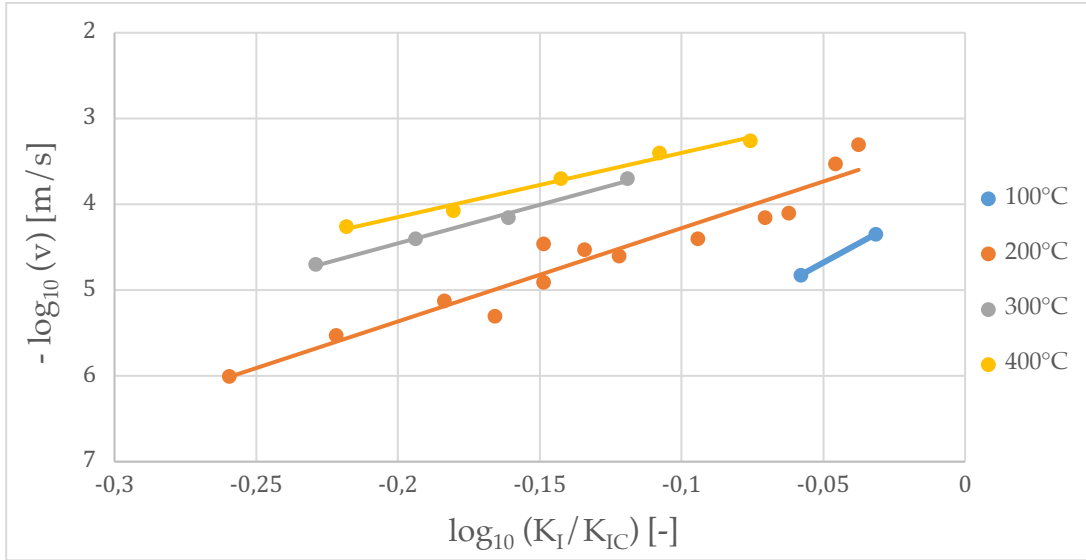


Figure 5.19: Summary of all the thermally treated sample about the subcritical crack growth

Chapter 6

Fracture mechanism application to the LEM analysis

In this chapter the fracture mechanism approach (equation 2.6), described in the section 2.2, is embedded in the limit equilibrium method used in the first chapter to compute the safety factor of the “Madonna del Sasso” unstable rock mass. In this way, then, it is possible to evaluate the time-dependent reduction in the rock bridge width, and therefore to study the safety factor’s variation over the time.

$$a(t) = \left[a_0^{1+\frac{n}{2}} - \left(1 + \frac{n}{2}\right) At \left[\frac{2w(\tau - \sigma_n \tan\varphi)}{K_{IIC}\sqrt{\pi}} \right]^n \right]^{1/(2+n)} \quad (6.1)$$

6.1 Problem’s assumptions

The first aspect which must be considered in a stability analysis is the level of degradation of the rock along the discontinuity. In fact, the majority of tests has been done on 200°C thermally treated samples, because we supposed that it could be a reasonable degree of internal damage existing along the joints. Therefore, the subcritical crack growth parameters and the mode II fracture toughness are referred to the 200°C thermally treated samples.

According to the second assumption, only the stability of sector A is carried out with an initial persistence value of 99% and rock bridge is assumed in the

middle of the discontinuity (Figure 6.1). Thus, the parameter $2w$ is equal to 40.6 m and $2a$ is 0.4 m , by considering the geometry of the sector A.

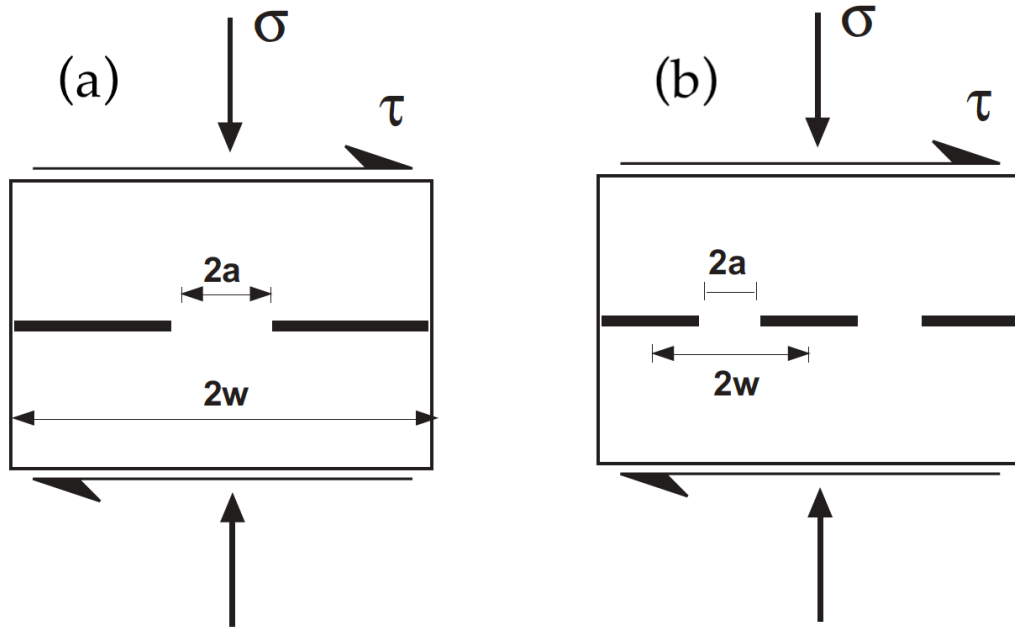
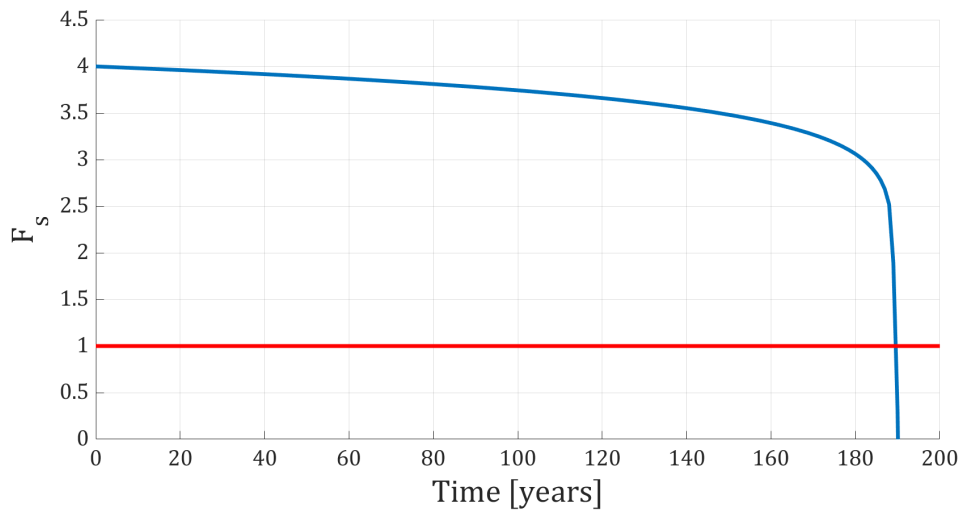


Figure 6.1: Fracture mechanics models, a) single rock bridge under far field normal and shear stresses, b) multiple rock bridges under far field normal and shear stresses [10]

Finally, the last assumption is related to the stress at the level of the discontinuity. The only force considered in the analysis is the weight of the rock mass, in order to simplify the study. In this way, the normal stress σ_n and the shear stress τ can be computed by decomposing the weight force along the two directions.

6.2 Analysis result

The Figure 6.2 shows the decrease of the safety factor F_s over the time in function of the rock bridge reduction. At the beginning, as expected, the F_s is about equal to 4, that is the same value computed in the classical LEM analysis. In the first 150 years, it decreases very slowly reaching the value 3.5, but after about 180 years the decline is much more rapid. The safety factor reaches the critical value 1 after 193 years.

Figure 6.2: Reduction of the Safety factor over the years with $n=13$

6.3 Limits of the analysis

The fracture mechanism application used for the prediction of progressive rock bridge reduction appears to be rather sensitive to the input parameters such as the stress field and the subcritical crack growth parameters. This is an important limitation for the practical application of this method because to know the stress state inside a rock mass is very complex. Furthermore, the determination of parameters A and n might show large variability due to heterogeneous behaviour of rock samples. In fact, in order to better understand the model, some parametric analyses have been performed. Figure 6.3 shows the influence of the index of internal damage n , that has been set at 15 rather than 13. We could expect a minimal difference in behaviour compared to the previous case but, on the contrary, the differences are relevant. The failure of the unstable rock mass is expected only after 350 years, about 160 years later than in the previous case. Finally, the subcritical crack growth parameters have been investigated at the laboratory scale, but they have been used for a large scale analysis. In slope stability problems, to neglect the scale effect represents a big limit for a valid prediction of the safety factor. Therefore, it appears that this approach still needs to be improved before being considered reliable for big scale application on rock slope stability. Nevertheless it is important to note the progressive decrease

of the safety factor over the time which suggests the importance of in-site monitoring also in areas which nowadays could be considered safe.

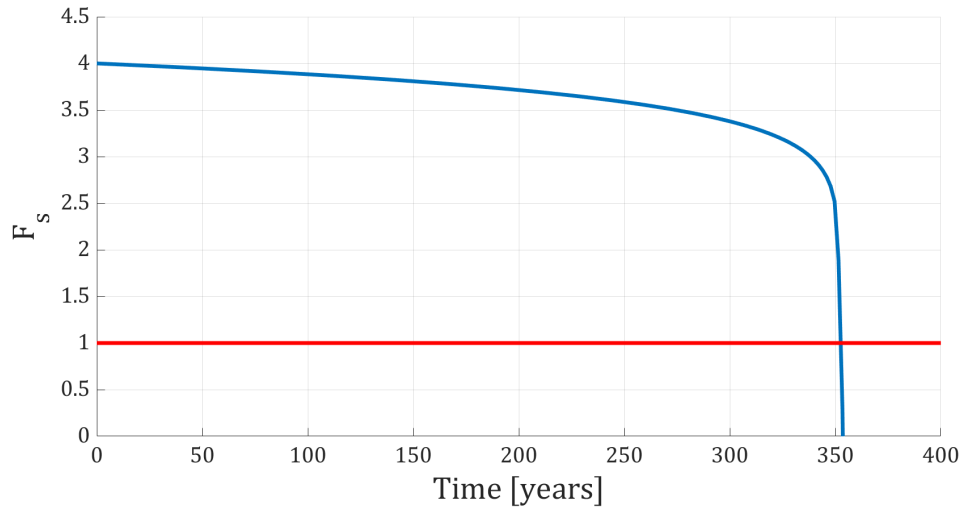


Figure 6.3: Reduction of the Safety factor over the years with $n=15$

Chapter 7

Conclusions and perspectives

The study of stability and prediction of the behaviour of an unstable rock mass represents one of the most difficult problems in the engineering field. Its complexity is linked to the difficult identification of the mechanical parameters to be used in the numerical analysis, and to the high variability of external factors such as air temperature variation, presence and evaluation of water pressure, seismic events, rock degradation.

In the chapter 1, the stability analysis of the cliff of “Madonna del Sasso” has been carried out with the Limit Equilibrium Method (LEM) which is one of the most used approach in the geotechnical field for the evaluation of rock slope stability. In the LEM analysis the rock mass is considered as rigid body, and the presence of discontinuities is taken into account by choosing strength parameters lower than the those characteristic of the rock material. However, this continuum assumption leads to ignore the effect of the crack tip stress concentrations. Furthermore, another limits of the LEM analysis is the impossibility of considering an evolution over time of the rock’s mechanical parameters. Indeed, the area where the rock formation mostly degrade is concentrated at the joints and, if discontinuities are filled with a material that is weaker than the surrounding intact rock, this material might exhibit ductile creep behaviour under shear loading.

For this reason, in the chapter 2, the fracture mechanism approach developed by J. Kemeny has been proposed in order to overcome the LEM limits. According to his study, the effects of degradation of rock joint can be evaluated through a time-dependent reduction of rock bridge along the discontinuity, due to the subcritical crack growth. Then, the application of this

approach to the LEM analysis can allow to evaluate not only the influence of the existing openings, but also the evolution over time of the rock's mechanical parameters due to rock degradation.

After a preliminary analysis in the chapter 3, several laboratory experiments have been carried out on the granitic CCNBD specimens in the chapter 4, in order to investigate the subcritical crack growth parameters, the mode I and mode II fracture toughness. The fracture propagation has been investigated under three types of load: increasing until the failure, creep and cyclic. Furthermore, the samples have been thermally treated at different temperatures in order to emulate the degradation that the rock can undergo in situ. Initially, different thermally treated CCNBD specimens have been tested under an increasing load, in order to analyse the mode I fracture toughness as a function of the degree of internal damage and, as expected, a clear decrease of the fracture toughness can be noticed in relation to the increasing temperature of the thermal treatment (K_{IC} is equal to $0.99 \text{ MPa}\sqrt{\text{m}}$ for the not treated sample, instead it is $0.65 \text{ MPa}\sqrt{\text{m}}$ for the 400°C thermally treated). Furthermore, according to the acoustic emissions analysis, it is evident that the amount of recorded events tends to be lower for the most damaged samples. Then, it is reasonable to expect that the energy generated by the microcracks is also lower for the damaged samples. Subsequently the creep behaviour has been investigated for the 200°C thermally treated samples, where the duration of the creep phase and also the number of acoustic events increase progressively with the decrease of the applied load. Finally, the mode I fracture toughness test has been investigated under cyclic load in order to study the fatigue behaviour of the granite of Alzo as a function of the applied load, keeping a constant thermal treatment and internal damage. Comparing these results with those of the creep tests, it is evident that the failure is reached much faster in the cyclic test if it is considered the average stress intensity applied. In the last experiments, the mode II fracture toughness has been calculated always through the CCNBD specimen thermally treated at 200°C , in order to have data that could be representative of the real internal damage existing along the joints.

Subsequently, the subcritical crack velocity has been calculated for each creep test through the derivative of the crack mouth opening displacement (CMOD) starting from the beginning of the creep phase until the reaching of the first crack propagation. Then, the subcritical crack growth parameters A and n can have been found graphically. At this point, It was possible to apply the fracture mechanism approach to the LEM analysis in order to investigate the safety factor evolution over the time as function of the rock bridge reduction. The final result has been obtained under the assumptions of an average degradation of the rock mass similar to the 200°C thermally treated samples, and of an initial persistence value of 99 % with a rock bridge in the middle of the discontinuity. The results look very consistent showing that the reduction of the safety factor F_s becomes critical after 193 years with these assumptions. Nevertheless, The fracture mechanism application used for the prediction of progressive rock bridge reduction seems to be rather sensitive to the input parameters such as the stress field and the subcritical crack growth parameters. Therefore, it appears that this approach still needs to be improved before being considered reliable for big scale application on rock slope stability.

However, it is important to note the progressive decrease of the safety factor over the time which suggests the importance of in-site monitoring also in areas which nowadays could be considered safe.

7.1 Perspectives

The amount of data collected during this master's thesis could be further analysed in order to investigate in depth the behaviour of the granite of Alzo.

The acoustic emission recordings, for instance, could be used to carry out an analysis about the kind of failure and the amount of released energy during the tests. Furthermore, it is possible to try to locate the main crack propagations through the AE recordings.

Furthermore, a numerical model of crack propagation could be developed from the experimental data. Passing from the laboratory to big scale, it could

be used to predict the behaviour of unstable rock slope. In this case, however, it would be appropriate to study the crack propagation in different lithologies in order to evaluate the influence of the type of rock.

Another perspectives could be the implementation of the mechanical approach in a Finite Element Method (FEM) that could improve a lot the analysis. It is possible, with a FEM, to evaluate the stress state in each point of the rock mass and to compute its evolution over the time and, in this way, a more reliable analysis is obtained. For example, a software capable of carrying out this analysis is 3DEC. It is a three-dimensional numerical modelling code for advanced geotechnical analysis of soil, rock, ground water, structural support, and masonry. 3DEC simulates the response of discontinuous media (such as jointed rock or masonry bricks) that is subject to either static or dynamic loading. The numerical formulation is based on the distinct element method (DEM) for discontinuum modelling.

Finally, coming back to the Limit Equilibrium Method, it can be improved with a field investigation, in order to obtain a valid characterization of the rock mass of "Madonna del Sasso". The main limit of the previous LEM analysis is the lack of mechanical data, indeed, the data used are referred to intact rocks but, in reality, mechanical data related to the entire rock cluster are needed. This is the reason why the safety factor obtained is probably higher than the real case. The calculation of "RMR" or "GSI" indexes, for instance, would allow to characterized in a better way the rock cluster through "Hoek and Brown" criterion. In this way, indeed, it is possible to obtain cohesion and friction angle values of the entire cluster, considering the rock matrix and the discontinuities as a whole. The behaviour of potentially unstable rock cliffs, indeed, is strongly controlled by the structural discontinuity pattern affecting the rock mass.

References

- [1] A. Boriani and E. Giobbi, "Does the basement of western southern Alps display a tilted section through the continental crust? A review and discussion," *Period. di Mineral.*, vol. 73, no. SPEC. ISSUE 2, pp. 5–22, 2004.
- [2] R. Lancellotta, P. Gigli, and C. Pepe, "Relazione tecnica riguardante la caratterizzazione geologico-strutturale dell'ammasso roccioso e le condizioni di stabilità della rupe. Private Communication.," 1991.
- [3] C. Colombero, L. Baillet, C. Comina, D. Jongmans, and S. Vinciguerra, "Characterization of the 3-D fracture setting of an unstable rock mass: From surface and seismic investigations to numerical modeling," *J. Geophys. Res. Solid Earth*, vol. 122, no. 8, pp. 6346–6366, 2017.
- [4] C. Colombero, C. Comina, A. M. Ferrero, G. Mandrone, G. Umili, and S. Vinciguerra, "An integrated approach for monitoring slow deformations preceding dynamic failure in rock slopes: A preliminary study," *Eng. Geol. Soc. Territ. - Vol. 6 Appl. Geol. Major Eng. Proj.*, pp. 699–703, 2015.
- [5] C. Colombero, C. Comina, S. Vinciguerra, and P. M. Benson, "Microseismicity of an Unstable Rock Mass: From Field Monitoring to Laboratory Testing," *J. Geophys. Res. Solid Earth*, vol. 123, no. 2, pp. 1673–1693, 2018.
- [6] G. J. Hearn, "C4 Rock slope stabilization," *Geological Society, London, Engineering Geology Special Publications 24.1*, pp. 189–208, 2011.
- [7] C. Colombero, C. Comina, G. Umili, and S. Vinciguerra, "Multiscale geophysical characterization of an unstable rock mass," *Tectonophysics*, vol. 675, pp. 275–289, 2016.

-
- [8] G. R. Irwin, "Analysis of stresses and strains near the end of a crack traversing a plate," *J. Appl. Mech.*, vol. 24, pp. 361–364, 1957.
- [9] C. Scavia, "A method for the study of crack propagation in rock structures," *Géotechnique*, vol. 45, no. 3, pp. 447–463, 1995.
- [10] J. Kemeny, "The time-dependent reduction of sliding cohesion due to rock bridges along discontinuities: A fracture mechanics approach," *Rock Mech. Rock Eng.*, vol. 36, no. 1, pp. 27–38, 2003.
- [11] R. J. Charles, "Dynamic fatigue of glass," *J. Appl. Phys.*, vol. 29, no. 12, pp. 1657–1662, 1958.
- [12] M. D. Kuruppu, Y. Obara, M. R. Ayatollahi, K. P. Chong, and T. Funatsu, "ISRM-suggested method for determining the mode I static fracture toughness using semi-circular bend specimen," *Rock Mech. Rock Eng.*, vol. 47, no. 1, pp. 267–274, 2014.
- [13] R. J. Fowell and C. Xu, "The cracked chevron notched Brazilian disc test—geometrical considerations for practical rock fracture toughness measurement," *Int. J. Rock Mech. Min. Sci.*, vol. 30, no. 7, pp. 821–824, 1993.
- [14] R. J. Fowell and C. Xu, "The use of the cracked Brazilian disc geometry for rock fracture investigations," *Int. J. Rock Mech. Min. Sci.*, vol. 31, no. 6, pp. 571–579, 1994.
- [15] R. J. Fowell, C. Xu, and P. A. Dowd, "An update on the fracture toughness testing methods related to the cracked Chevron-notched Brazilian disk (CCNBD) specimen," *Pure Appl. Geophys.*, vol. 163, no. 5–6, pp. 1047–1057, 2006.
- [16] Guéguen, Yves, and Kachanov, *Effective elastic properties of cracked rocks—An overview*. Springer Vienna, 2011.
- [17] J. B. Walsh, "The effect of cracks on the compressibility of rock," *J. Geophys. Res.*, vol. 70, no. 2, pp. 381–389, 1965.
- [18] M. H. Waxman and L. J. M. Smits, "Electrical Conductivities in Oil-Bearing Shaly Sands," *Soc. Pet. Eng.*, 1968.

- [19] J. Wang, J. K. Carson, M. F. North, and D. J. Cleland, "A new approach to modelling the effective thermal conductivity of heterogeneous materials," *Int. J. Heat Mass Transf.*, vol. 49, no. 17–18, pp. 3075–3083, 2006.
- [20] M. Adelinet, J. Fortin, and Y. Guéguen, "Dispersion of elastic moduli in a porous-cracked rock: Theoretical predictions for squirt-flow," *Tectonophysics*, vol. 503, no. 1–2, pp. 173–181, 2011.
- [21] Fowell, R. J., et al. "Suggested method for determining mode I fracture toughness using cracked chevron notched Brazilian disc (CCNBD) specimens." *International Journal of Rock Mechanics and Mining Sciences and Geomechanics Abstracts*, vol. 7, no. 32, 1995.
- [22] M. R. M. Aliha, R. Ashtari, and M. R. Ayatollahi, "Mode I and Mode II Fracture Toughness Testing for a Coarse Grain Marble," *Appl. Mech. Mater.*, vol. 5–6, pp. 181–188, 2006.
- [23] S. H. Chang, C. I. Lee, and S. Jeon, "Measurement of rock fracture toughness under modes I and II and mixed-mode conditions by using disc-type specimens," *Eng. Geol.*, vol. 66, no. 1–2, pp. 79–97, 2002.
- [24] N. Erarslan and D. J. Williams, "Mixed-mode fracturing of rocks under static and cyclic loading," *Rock Mech. Rock Eng.*, vol. 46, no. 5, pp. 1035–1052, 2013.
- [25] M. H. B. Nasser, A. Schubnel, and R. P. Young, "Coupled evolutions of fracture toughness and elastic wave velocities at high crack density in thermally treated Westerly granite," *Int. J. Rock Mech. Min. Sci.*, vol. 44, no. 4, pp. 601–616, 2007.
- [26] M. H. B. Nasser, B. S. A. Tatone, G. Grasselli, and R. P. Young, "Fracture toughness and fracture roughness interrelationship in thermally treated westerly granite," *Pure Appl. Geophys.*, vol. 166, no. 5–7, pp. 801–822, 2009.
- [27] J. Kemeny, "A model for non-linear rock deformation under compression due to sub-critical crack growth," *Int. J. Rock Mech. Min. Sci. Geomech. Abstr.*, vol. 28, no. 6, pp. 459–467, 1991.

- [28] T. Y. Ko and J. Kemeny, "Determination of the subcritical crack growth parameters in rocks using the constant stress-rate test," *Int. J. Rock Mech. Min. Sci.*, vol. 59, pp. 166–178, 2013.
- [29] J. E. Olson, "Joint pattern development: Effects of subcritical crack growth and mechanical crack interaction," *J. Geophys. Res. Solid Earth*, vol. 98, no. B7, pp. 12251–12265, 1993.
- [30] B. K. Atkinson, "Subcritical Crack Growth in Geological Materials," *J. Geophys. Res.*, vol. 89, no. 10, pp. 4077–4114, 1984.
- [31] P. G. Meredith and B. K. Atkinson, "Fracture toughness and subcritical crack growth during high-temperature tensile deformation of Westerly granite and Black gabbro," *Phys. Earth Planet. Inter.*, vol. 39, no. 1, pp. 33–51, 1985.

Acknowledgements

The big day finally has arrived: writing these lines of acknowledgments is the finishing touch of my master's thesis. It was a period of deep learning not only from a scientific viewpoint, but also from a personal perspective. I would like to say a couple of words of thanks to all the people who have supported and helped me throughout this period.

The first person I would like to gratefully acknowledge is Prof. Marie Violay for his crucial role in the development of my Master's Thesis. First of all, I wish to thank her for all the time spent to help me, and for all the suggestions which have been fundamental in my growth process. But above all, I am grateful because she taught me the importance of work scheduling. She drove me to make decisions in complete autonomy, thus contributing to a significant professional and personal growth.

I would also like to express my very great appreciation to the other supervisors of my Master's Thesis, i.e., Dr.ssa Federica Sandrone, Dr. Lucas Pimienta, Dr. François Passèlegue and Prof. Claudio Scavia, for the comments provided as a result of the revision of my work. Ringrazio la Dr.ssa Federica Sandrone per la grande disponibilità e per tutto il tempo che mi ha dedicato nel contesto del lavoro di tesi. I suoi consigli e la sua positività sono stati fonte di grande incoraggiamento durante tutto il periodo della mia permanenza a Lausanne. I would like to thank Dr. Lucas Pimienta for all the support and suggestions, and especially for showing me what it really means to work in a laboratory. A great thank also goes to Dr. François Passèlegue for his willingness and for his help in the field of the acoustic emission analysis, without whom it would not have been possible. Infine, un ringraziamento speciale va al Prof. Claudio Scavia, per aver suscitato in me la passione per la

meccanica delle rocce, così come per la disponibilità mostrata nell'approfondire e migliorare il lavoro di Tesi Magistrale.

I wish to thank Laurent Gastaldo for his huge help with the CCNBD sample preparation, and a special thanks to the entire LEMR team (Laboratory of Experimental Rock Mechanics).

Un ringraziamento va alla Dott.ssa Chiara Colombero ed al Prof. Sergio Carmelo Vinciguerra dell'Università di Torino per aver condiviso dati sperimentali riguardo lo studio di stabilità sull'ammasso roccioso della "Madonna del Sasso", e per aver mostrato grande interesse e nel mio lavoro di tesi magistrale.

Ringrazio di cuore la mia famiglia ed i miei genitori per essere stati dei riferimenti costanti nella mia vita e per avermi sempre sostenuto, consigliato e incoraggiato nel cammino intrapreso.

Ringrazio i miei fratelli, Marika e Marco, per esserci stati nei momenti di difficoltà, facendomi capire sempre che uniti si è sempre più forti.

Infine un profondo ringraziamento è dedicato a tutte quelle persone con cui ho condiviso bei momenti e che mi sono sempre rimaste vicine, anche da lontano: Alessandra, Celeste, Christian, Davide, Federico, Francesco, Giulia, Marco e Riccardo. Grazie per aver reso questi anni speciali.

Un capitolo della mia vita ormai si è concluso, ed è ora di iniziarme uno nuovo, ma questi anni trascorsi li porterò sempre nel mio cuore.

Ad Maiora!

*“Questa parte della mia vita, questa piccola parte
della mia vita si può chiamare felicità!”*

*Chris Gardner (Will Smith)
dal film “La ricerca della felicità”*